RESPONSE SURFACE APPROXIMATIONS FOR PITCHING MOMENT INCLUDING PITCH-UP IN THE MULTIDISCIPLINARY DESIGN OPTIMIZATION OF A HIGH-SPEED CIVIL TRANSPORT

by

Paul J. Crisafulli

Thesis submitted to the faculty of the

Virginia Polytechnic Institute & State University

in partial fulfillment of the requirements for the degree of

Master of Science

in

Aerospace Engineering

APPROVED:

William H. Mason, Committee Chairman

Bernard Grossman

Frederick H. Lutze

June 1996

Blacksburg, Virginia

RESPONSE SURFACE APPROXIMATIONS FOR PITCHING MOMENT INCLUDING PITCH-UP IN THE MULTIDISCIPLINARY DESIGN OPTIMIZATION OF A HIGH-SPEED CIVIL TRANSPORT

by

Paul J. Crisafulli

Committee Chairman: William H. Mason

Aerospace & Ocean Engineering

Abstract

A procedure for incorporating a key non-linear aerodynamic characteristic into the design optimization of a high-speed civil transport has been developed. Previously, the tendency of a high-speed aircraft to become uncontrollable (pitch-up) at high angles-of-attack during landing or takeoff for some wing shapes could not be included directly in the design process. Using response surface methodology, polynomial approximations to the results obtained from a computationally expensive estimation method were developed by analyzing a set of statistically selected wing shapes. These response surface models were then used during the optimization process to approximate the effects of wing planform changes on pitch-up. In addition, response surface approximations were used to model the effect of horizontal tail size and wing flaps on the performance of the aircraft. Optimizations of the high-speed civil transport were completed with and without the response surfaces. The results of this study provide insight into the influence of nonlinear and more detailed aerodynamics on the design of a high-speed civil transport.

Acknowledgments

This work would not have been possible without the support of the NASA Langley Research Center under grant NAG1-1160, with Peter Coen as the grant monitor, and the support of the NASA/Universities Space Research Association/Advanced Design Program. This work is also based on the previous work done by Alex Benoliel and several other graduate students.

I would like to thank my advisor, Dr. William H. Mason, for his guidance throughout my undergraduate and graduate education. I would also like to thank Dr. Bernard Grossman, Dr. Raphael Haftka and Dr. Layne Watson for their support and advice during our weekly meetings. Matt Kaufman, Tony Giunta, Vladimir Balabanov and Pete MacMillan also provided me with help and suggestions throughout this project.

I deeply appreciate the support and understanding of my loving parents, Lunette and Joseph Crisafulli. Finally, I would like to extend a special thanks to a special friend, Susan Watson, who shared my success and hardships through my final years at Virginia Tech.

Table of Contents

List of Figures

List of Tables

List of Symbols

α	angle-of-attack
α_B	pitch-up angle-of-attack
ac	aerodynamic center
cg	center-of-gravity
C_L	lift coefficient
$C_{L\alpha}$	lift curve slope, $\partial C_L/\partial\alpha$
$C_{L\delta e}$	change in lift with elevator deflection, $\partial C_L/\partial\delta e$
$C_{L\delta f}$	change in lift with flap deflection, $\partial C_L/\partial\delta f$
C_M	pitching moment coefficient
$C_{M\alpha}$	change in pitching moment with angle-of-attack, $\partial C_M/\partial\alpha$
$C_{M\alpha 1}$	$\partial C_M/\partial\alpha$ before pitch-up
$C_{M\alpha 2}$	$\partial C_M/\partial\alpha$ after pitch-up
C_{Mo}	zero lift pitching moment coefficient
$C_{M\delta e}$	change in pitching moment with elevator deflection, $\partial C_M/\partial\delta e$
$C_{M\delta f}$	change in pitching moment with flap deflection, $\partial C_M/\partial\delta f$
˘$C_{M\delta e}$	increment in pitching moment at a particular elevator deflection, $\partial C_M/\partial\delta e \;\; \delta e$
˘$C_{M\delta f}$	increment in pitching moment at a particular flap deflection, $\partial C_M/\partial\delta f \;\; \delta f$
˘$C_{L\delta f}$	increment in lift at a particular flap deflection, $\partial C_L/\partial\delta f \;\; \delta f$
LE	leading-edge
mac	mean aerodynamic chord
S	wing area
TE	trailing-edge

Greek symbols

α	angle-of-attack
δe	elevator deflection, positive downward
δf	flap deflection, positive downward

Acronyms

APE	Aerodynamic Pitch-up Estimation
BFL	Balanced Field Length
CCD	Central Composite Design
CCV	Control Configured Vehicle
CFD	Computational Fluid Dynamics
HSCT	High-Speed Civil Transport
MDO	Multidisciplinary Design Optimization
RS	Response Surface
RSM	Response Surface Methodology
RSS	Relaxed Static Stability
SAS	Stability Augmentation System
TOGW	Take Off Gross Weight

1. Introduction

The use of optimization methods in the design of aerospace vehicles is often limited due to the need to use computationally expensive design tools such as Computational Fluid Dynamics (CFD), where a single design point analysis may take many hours and thousands of analyses are needed during a single optimization cycle. In addition, the results often contain small wiggles as a function of the design variables due to the presence of numerical noise which affects convergence and lengthens the optimization process. To obtain an optimal aircraft configuration within a reasonable amount of time, algebraic relations or computationally inexpensive models, with a compromise in accuracy, have been used to shorten the optimization cycle in aircraft design programs such as FLOPS[1] and ACSYNT[2]. Another technique is to use a variable complexity modeling approach which involves combining computationally expensive models with simple and computationally inexpensive models. This technique has been previously applied to the aerodynamic-structural optimization of the High-Speed Civil Transport[3,4]. An additional approach is to replace computationally expensive analysis tools with a statistical technique, called response surface methodology, in the actual optimization process. Response surface methodology approximates the response of a computationally expensive analysis tool with a low-order polynomial by examining the response of a set of statistically selected numerical experiments. The result is an extremely fast function evaluation, which not only shortens the optimization process but also filters out any numerical noise generated by the analysis tools. Without numerical noise to create artificial local minima and inhibit optimization, an optimal design is much easier to obtain. The response surface approach has been applied to the wing structural optimization of the High-Speed Civil Transport[5] and to the aerodynamic design of the wing of a High-Speed Civil Transport[6].

In this study, the integration of a key non-linear aerodynamic characteristic (pitch-up) into the design optimization of a high-speed civil transport is addressed using response surface approximations. In previous studies[3-5], variable complexity modeling was used to calculate the linear aerodynamic relationship between the pitching moment and the angle-of-attack of a high-speed civil transport configuration. However, these studies did not include the aerodynamic pitch-up which occurs at low speeds due to non-linear aerodynamic effects related to wing planforms typically proposed for supersonic cruise transports. In addition, response surface approximations were used to model the effects of using wing flaps on the takeoff performance of the aircraft. With the use of the Aerodynamic Pitch-up Estimation (APE) method developed by Benoliel and Mason[7], a means of estimating aerodynamic characteristics and pitch-up of high-speed aircraft wings is now available and can be used during the design optimization.

Optimizations of the high-speed civil transport were completed with and without response surface models. The response surface models were used during the optimization to integrate a simple approximation of the aerodynamic characteristics and pitch-up as predicted by the APE method instead of using the APE method itself, where a single analysis may take minutes and thousands of analyses are needed in a single optimization cycle. Another benefit is to smooth out the noise generated by APE, which is a problem for any derivative-based optimization.

Section 2 is a review of the multidisciplinary design optimization efforts for a high-speed civil transport at Virginia Tech and includes the current method for horizontal tail sizing. Section 3 describes possible improvements to the horizontal tail sizing methodology. Pitch-up and the APE method are described in Section 4. Section 5 describes the nonlinear pitching moment and flap effect models. Response surface methodology and its use within optimization is introduced in Section 6. Section 7 applies the response surface methodology to the results of the APE method. Section 8 presents the results of the optimizations of a high-speed civil transport with and without the response surface models. Finally, Section 9 includes the conclusions of this study.

2. HSCT Design Optimization

The design problem studied extensively at Virginia Tech is to minimize the total takeoff gross weight of a 251 passenger High Speed Civil Transport with a range of 5,500 nautical miles and a cruise speed of Mach 2.4. A design code has been developed which comprises of conceptual-level and preliminary-level tools which estimate the subsonic and supersonic aerodynamics, takeoff and landing performance, mission performance, propulsion, and weights. The HSCT is defined by 29 variables which include the planform shape and thickness distribution of the wing, the area ruling of the fuselage, engine nacelle locations, tail sizes, the cruise trajectory, and the amount of fuel to be carried. The configuration is analyzed and then optimized by evaluating constraints on the geometry, performance, and aerodynamics using the conceptual-level and preliminary-level tools. An optimized HSCT configuration will have the minimum TOGW which satisfies all the constraints on the problem.

2.1 Optimization Problem

Twenty-nine design variables are used to describe the HSCT design problem and are listed in Table 1. The wing planform is specified using eight design variables which include the wing root chord, wing tip chord, wing span, locations of the wing leading-edge and trailing-edge break points, and the location of the leading-edge of the wing tip as shown in Figure 1. The airfoil sections (Figure 1) are described by four design variables which include the airfoil leading-edge radius parameter, chordwise location of maximum thickness, and the wing thickness at the wing root, leading-edge break, and tip. The thickness distribution at any spanwise station is then defined as follows:

1. The wing thickness varies linearly between the wing root, leading-edge break, and wing tip.

2. The chordwise location of maximum airfoil thickness is constant across the span.
3. The airfoil leading-edge radius parameter is constant across the span. The leading-edge radius-to-chord ratio, r_t, is defined by $r_t = 1.1019[(t/c)(I/6)]^2$.
4. The trailing-edge half-angle of the airfoil section varies with the thickness-to-chord ratio according to $\tau_{TE} = 3.03125(t/c) - 0.044188$. This relationship is fixed throughout the design.

Two design variables position the nacelles spanwise along the trailing-edge of the wing. Another design variable specifies the maximum sea level thrust per engine. The fuselage is assumed to be axisymmetric and is area ruled using eight variables which include the axial positions and radii of four fuselage restraint locations. The horizontal tail and vertical tail areas are described using two variables. These control surfaces are trapezoidal planforms, where the aspect ratio, taper ratio, and quarter chord sweep are specified. Three additional design variables include the fuel weight, initial supersonic cruise altitude, and constant cruise climb rate. Additional parameters which describe the design problem are included in Table 2. These values do not change during the optimization and include flight characteristics, takeoff and landing parameters, landing gear parameters, baseline engine values, and other miscellaneous design settings which are discussed in detail in Reference 8.

Table 1. Design variables.

#	Baseline Value	Description	#	Baseline Value	Description
1	181.5	Wing root chord (*ft*)	16	12.2	Fuselage restraint 2, *x* (*ft*)
2	155.9	LE break, *x* (*ft*)	17	3.5	Fuselage restraint 2, *r* (*ft*)
3	49.2	LE break, *y* (*ft*)	18	132.5	Fuselage restraint 3, *x* (*ft*)
4	181.6	TE break, *x* (*ft*)	19	5.3	Fuselage restraint 3, *r* (*ft*)
5	64.2	TE break, *y* (*ft*)	20	248.7	Fuselage restraint 4, *x* (*ft*)
6	169.6	LE of wing tip, *x* (*ft*)	21	4.6	Fuselage restraint 4, *r* (*ft*)
7	7.0	Tip chord (*ft*)	22	26.2	Nacelle 1, *y* (*ft*)
8	75.9	Wing semi-span (*ft*)	23	32.4	Nacelle 2, *y* (*ft*)
9	0.4	Chordwise location of max *t/c*	24	322,617	Mission fuel (*lbs*)
10	3.7	Airfoil LE radius parameter, r_t	25	64,794	Starting cruise altitude (*ft*)
11	2.6	Airfoil *t/c* at root (%)	26	33.9	Cruise climb rate (*ft/min*)
12	2.2	Airfoil *t/c* at LE break (%)	27	697.9	Vertical tail area (*sq ft*)
13	1.8	Airfoil *t/c* at tip (%)	28	713.1	Horizontal tail area (*sq ft*)
14	2.2	Fuselage restraint 1, *x* (*ft*)	29	55,465	Max sea level thrust per engine (*lbs*)
15	1.1	Fuselage restraint 1, *r* (*ft*)			

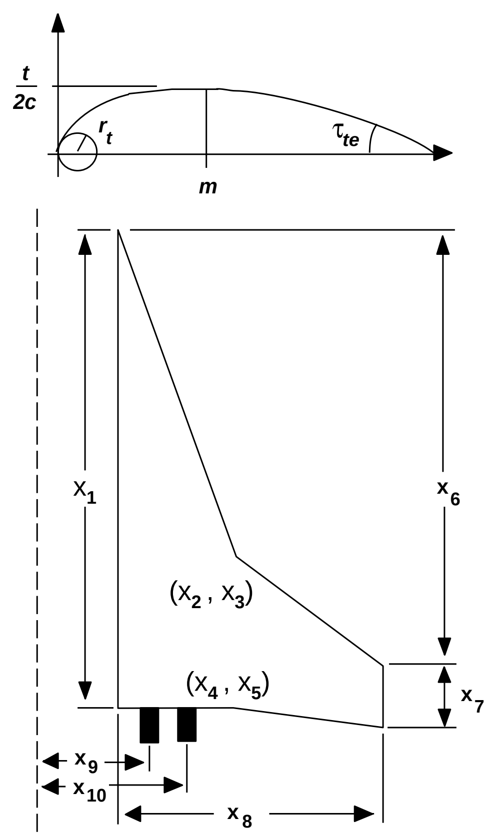

Figure 1. Airfoil section and wing planform with design variables.

Table 2. Command file options.

Flight Characteristics		**Landing**	
Altitude at start of cruise (*ft*)*	50,000	Speed (*knots*)	145.0
Climb rate in cruise (*ft/min*)*	100	Maximum landing angle of attack (*deg*)	12.0
Mach number	2.4	CLmax	1.0
Design lift coefficient	0.10	Clmax	2.0
Fraction of leading edge suction	0.8	Fuel ratio at landing	0.5
Mission fuel weight (*lbs*)*	290,905	Cross wind speed (*knots*)	20.0
Landing Gear		**Miscellaneous**	
Main gear length (*ft*)	19.75	Fuel fraction of weights**	1.0
Nose gear length (*ft*)	18.75	Fuel density (lbs/ft^3)	48.75
Tipback angle (*deg*)	15.0	Percentage wing volume available for fuel	0.5
Maximum overturn angle (*deg*)	63.0	Minimum range (*n. mi.*)	5,500
Take Off		Minimum chord length (*ft*)	7.0
CLmax	0.9	Minimum engine spacing (*ft*)	7.0
Altitude (*ft*)	0.0	Structural interlacing factor***	1.0
Ground friction	0.03	**Engines**	
Braking friction	0.30	Thrust per engine	46,000
Stall _k	1.165	Ref. thrust for calculating engine weight	46,000
Braking reaction time (*sec*)	3.0	Reference weight	17,800
Height of obstacle (*ft*)	35.0	Reference diameter of nacelle	6.5
Maximum BFL (*ft*)	11,000	Reference length of nacelle	35.0
Maximum distance (*ft*)	9,000	Number of engines	4

* Overwritten by design variables.
** Fraction of fuel remaining for FLOPS weight and *cg* calculation.
*** Ratio of structural optimization bending material weight to FLOPS bending material weight.

A complete design optimization is comprised of a sequence of optimization cycles using sixty-nine constraints (Table 3), which include geometry, performance, and aerodynamic constraints on the design of the HSCT. These constraints are discussed in detail in References 4 and 8. During the optimization, the optimizer (NEWSUMT-A[9]) uses an objective function, which includes an extended interior penalty function for inequality constraints and an exterior penalty function for equality constraints, to identify an optimal aircraft design which satisfies all sixty-nine constraints. To shorten the entire optimization, variable-complexity modeling is used to scale the results of simple analyses to the results of computationally expensive exact analysis methods at the beginning each optimization cycle. These scale factors are carried through the optimization cycle with an added benefit of performing thousands of computationally inexpensive calculations, instead of time-consuming exact calculations, to predict an improved design. At the beginning of the next cycle, the design is evaluated with the exact analysis methods and new scale factors are calculated. This process continues until the design is converged or changes only slightly from cycle to cycle. More details of the variable complexity modeling are in Reference 4. A typical optimization is completed within 25 to 50 cycles using NEWSUMT-A. A typical optimization cycle takes approximately 10 minutes to complete on an R-8000 SGI Power Challenge.

Table 3. Optimization constraints.

#	Geometric Constraints	#	Aero. and Performance Constraints
1	Fuel volume † 50% wing volume	35	Range ‡ 5,500 *n. mi.*
2	Wing spike-shape prevention	36	Landing angle-of-attack † 12¡
3-20	Wing chord ‡ 7.0 *ft*	37	Landing C_L † 1.0
21	LE break † wing semi-span	38-56	Landing section C_l † 2.0
22	TE break † wing semi-span	57-59	No engine scrape at landing with 5¡ bank
23	Root *t/c* ‡ 1.5%	60-61	No wing scrape at landing with 5¡ bank
24	LE break *t/c* ‡ 1.5%	62-63	Limit aileron and rudder to 22.5¡ and bank to 5¡ during 20 knot crosswind landing
25	TE break *t/c* ‡ 1.5%		
26-30	Fuselage restraints, *x*	64	Tail deflection during approach † 22.5¡
31	Nacelle 1 ‡ side-of-body	65	Takeoff rotation † 5 seconds
32	Nacelle 1 † nacelle 2	66	Engine-out limit with vertical tail design
33	Nacelle 2 † wing semi-span	67	Balanced field length † 11,000 *ft*[*]
34	No negative TE sweep inboard TE break	68-69	Required engine thrust † available thrust

[*] MacMillin used a balanced field length constraint of 10,000 feet in Reference 8.

2.2 Analysis Methods

The design code comprises of conceptual-level and preliminary-level tools which include a combination of public domain software which was obtained from NASA and software developed in-house. The software can be broken into several design disciplines: subsonic and supersonic aerodynamics, takeoff and landing performance, mission performance, propulsion, and weights. In each group, there are several levels of analysis from more complex and computationally expensive analysis tools to simple approximate models, which are used together during the optimization using variable-complexity modeling. A list of analysis tools is provided in Table 4. Their applications within the design code are described in detail in References 3, 4, and 8.

Table 4. Analysis and optimization tools.

Design Discipline		Conceptual-Level Analysis	Preliminary-Level Analysis
Subsonic aerodynamics	Lift-curve slope	Diederich model[10]	VLM code[11]
	Pitching moment	DATCOM[12]	VLM code[11]
	LE vortex effects	Polhamus suction analogy[13]	
	Ground effect	Kuchemann s[14] and Torenbeek s[15] approximation	
	Stability and control derivatives	DATCOM[12]	VLM code by Kay[16]
Supersonic aerodynamics	Drag due to lift	Lineary theory for approx. cranked delta planform[17]	Supersonic panel code based on Carlson s Mach box code[18,19]
	Wave drag	Approx. version of classical far-field slender body formulation[11]	Harris wave drag code[20]
	Skin friction drag	Algebraic boundary-layer strip method[11]	
Takeoff /Landing performance	Engine-out	Algebraic relations[8]	
	Crosswind landing		
	Powered approach trim		
	Balanced field length	Loftin[21]	Numerical/analytical integration with Powers method[22]
Mission performance		Algebraic relations with minimum time climb using Rutowski[23] and Bryson s[24] energy approach	
Propulsion		Simple engine scaling	
Weights		FLOPS weight module[1]	GENESIS FEM optimization[25]
Optimization		NEWSUMT-A[9]	

Since we are concerned with the subsonic aerodynamic pitching moment in this study, there are two levels of modeling used to estimate the subsonic aerodynamics. The detailed calculations for the subsonic lift curve slope and pitching moment curve slope are performed using a vortex-lattice code developed by Hutchison which is discussed in detail in Reference 11. The code calculates the pitching moment at zero angle-of-attack and at 1 degree angle-of-attack. The differences in the pitching moment is the pitching moment curve slope ($C_{M\alpha}$). The simple approximation for the pitching moment curve slope is an empirical algebraic relation from the U.S.A.F. Stability and Control DATCOM[12]. Since we are not specifying a wing camber distribution*, the zero lift pitching moment (C_{Mo}) is zero.

2.3 Current Horizontal Tail Sizing

Three constraints on takeoff and landing performance currently have a major effect on the horizontal tail size or how much control power is needed during the mission. The take-off constraints include a balanced field length requirement of 11,000 feet and a rotation time to lift-off attitude constraint of less than 5 seconds. For approach trim, the aircraft must trim with a tail deflection of less than 22.5 degrees. These constraints were added to the design code by MacMillin[8].

2.3.1 Takeoff Performance

Takeoff performance is evaluated by integrating the equations of motion during the ground run, rotation, and climb out phases of takeoff. The sum of the horizontal distance covered by the airplane during these three segments is the takeoff field length. The longest distance required for takeoff occurs when an engine fails at a certain critical speed at which time the pilot can decide to abort the takeoff and safely brake to a stop or to continue the takeoff. This distance is known as the balanced field length or FAR takeoff distance.

---

* We do not specify a wing camber distribution within our aerodynamic evaluation, which is a good approximation to thin supersonic wings. Instead, we are currently integrating wing camber into the design via the wing bending material weight which is the major portion of the wing structural weight. This is performed using response surface approximations to wing structural weight optimizations which include aerodynamic loads which are affected by wing camber and twist.

During the evaluation of the takeoff requirements, lift and moment flap effects are added to the aerodynamics of the airplane. High-lift devices are important for low speed operation of the HSCT[26]. If high-lift devices are ignored, supersonic efficiency is compromised to satisfy low-speed performance requirements such as the takeoff balanced field length. Ground effect and drag due to the landing gear and a windmilling engine are also included within the calculations and are discussed in detail in Reference 8.

The takeoff requirements are calculated with an all-moving horizontal tail deflected -20 degrees, leading-edge flaps deflected 10 degrees, and trailing-edge flaps deflected 30 degrees. The longitudinal derivatives with respect to horizontal tail deflection ($C_{L\delta e}$,$C_{M\delta e}$) are calculated using a vortex lattice code developed by J. Kay[16]. In order to save computational effort, the derivatives are calculated only every five optimization cycles and are scaled using variable complexity within each optimization cycle. The longitudinal derivatives with respect to flap deflection ($C_{L\delta f}$, $C_{M\delta f}$) were picked based upon investigation of the aerodynamics of AST-105-1 configurations[27] and other proposed HSCT designs[7]. These derivatives are currently fixed throughout the optimization as:

$$C_{L\delta f} = 0.2508/\text{rad}$$

$$C_{M\delta f} = -0.0550/\text{rad}$$

The aircraft is required to rotate to lift-off in under 5 seconds. If takeoff rotation takes too much time, it will greatly increase the takeoff distance. This requirement was determined by MacMillin[8] before the balanced field length constraint was added to the design code. After investigating typical rotation times for large aircraft, he required the aircraft to rotate in under 5 seconds which is a reasonable assumption. Since this constraint is active in most of our optimizations, we are currently investigating the effect of increasing the time-to-rotate or may decide to remove the constraint entirely since the time-to-rotate is dependent on the takeoff speed and is included within the calculation of the takeoff rotation distance and balanced field length.

2.3.2 Approach Trim Performance

The aircraft must be able to be trimmed at an angle-of-attack well above operating procedures. In addition, there should be extra control deflection to allow for pitch control. We require that the tail deflection to trim is less than 22.5 degrees at a landing speed of 145 knots and an altitude of 5000 *ft* at maximum TOGW. The tail deflection required to trim the aircraft is determined by calculating the pitching moment about the aircraft center-of-gravity generated by the lift, drag, thrust, and weight. The tail deflection to trim is then found by calculating how much the tail needs to deflect in order to trim out the pitching moment (i.e. to obtain zero pitching moment about the *cg*). The approach trim analysis currently neglects the effects of flaps.

3. Proposed Improvements to Design Code and Other Related Issues

As described in Section 2.3, the horizontal tail is sized to provide adequate control during takeoff and landing. This section describes improvements to the horizontal tail sizing methodology which includes requirements on the center-of-gravity and the use of active control technology to minimize the required size of the horizontal tail. In addition, a short summary of the aerodynamic center and its shift from subsonic to supersonic cruise related to HSCT-type planforms is provided. This subject is important since the center-of-gravity range must be located properly relative to the aerodynamic center to balance the aircraft for minimum trimmed drag flight.

3.1 Center-of-Gravity Requirements

A typical tail sizing diagram used to find the minimum required horizontal tail size for the aircraft to meet center-of-gravity (*cg*) requirements is presented in Figure 2. This diagram is known as an *x*-plot or scissors-plot [28]. In this diagram, the forward and aft center-of-gravity limits are plotted against the non-dimensional horizontal tail volume, which is proportional to the size and moment arm of the horizontal tail. The required *cg* range represents the *cg* range needed to cover the anticipated combinations of fuel, passengers, cargo, etc. Typical *cg* ranges and tail volumes are provided by Roskam[29] in Table 5. To find the minimum tail size, the smallest value of tail volume is picked for which the distance between the forward and aft limits is equal to the required *cg* range.

The forward center-of-gravity location is typically limited by the control authority of the horizontal tail to rotate the aircraft nose-up about its main landing gear during takeoff, and to trim the aircraft during approach. Both constraints are shown in Figure 2. Several conditions may limit the aft *cg* locations. The aft center-of-gravity location is limited by the control authority of the horizontal tail to recover from a high angle-of-attack (nose-down control), the tip-back location of the main landing gear to ensure that the aircraft does not tip backwards onto its tail (tip-up limit), and the lower stability limit of the aircraft. Analysis must be made for a particular design to determine which constraints are critical. Prior to the use of RSS/CCV, the stability limit was normally the active constraint for the aft *cg* limit.

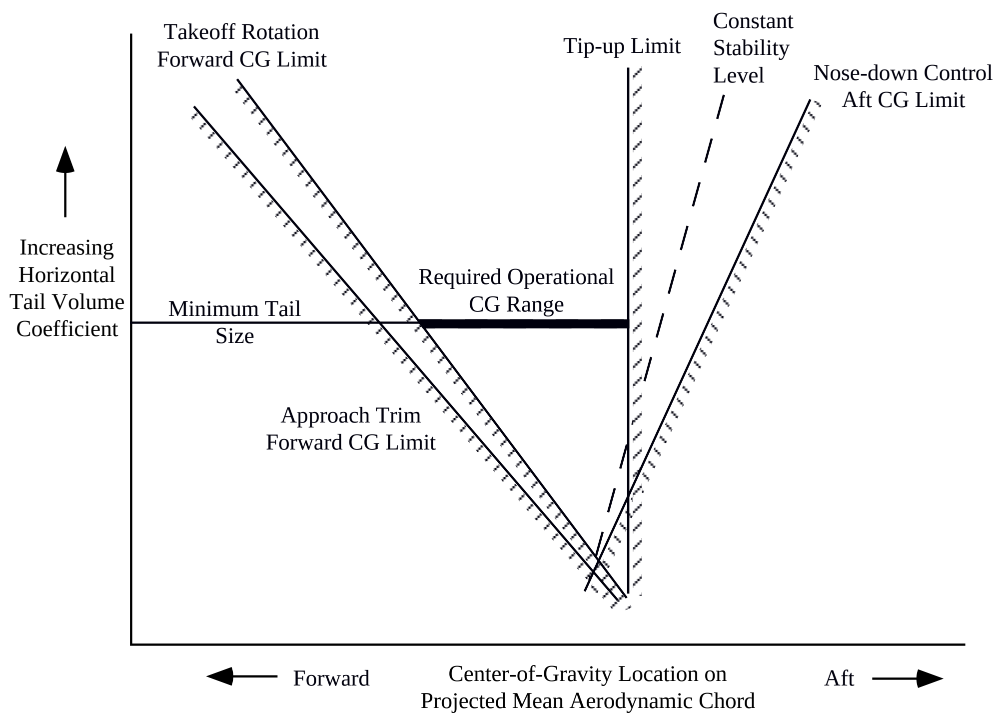

Figure 2. Tail sizing diagram (Ref. 28).

Table 5. Typical values of *cg* ranges and tail volumes (Ref. 29).

CG Range	
Jet transport	26 - 91 *in*, 0.12 - 0.32 *mac*
Supersonic cruise aircraft	20 - 100 *in*, 0.30 *mac*
Tail Volume	
Boeing SST	0.36
AST-100	0.052

As described in Section 2.3, the active constraints on takeoff and landing performance have a major effect on the size of the horizontal tail within the MDO process. As presented in Figure 3, these constraints do not include aft *cg* requirements associated with nose-down control or the required *cg* range. To automate the complete tail sizing diagram within an optimization code, the forward and aft center-of-gravity limits are needed for a given horizontal tail size. In general, the landing gear location would also be allowed to vary. Therefore, it is essential that the optimizer is given a range of possible center-of-gravity locations to search and locate the forward and aft limits given performance, stability, control and tipback requirements. Since the current procedure is to calculate a single *cg* location for each piece of an aircraft, a new procedure for calculating a range of possible locations for a given aircraft configuration is needed.

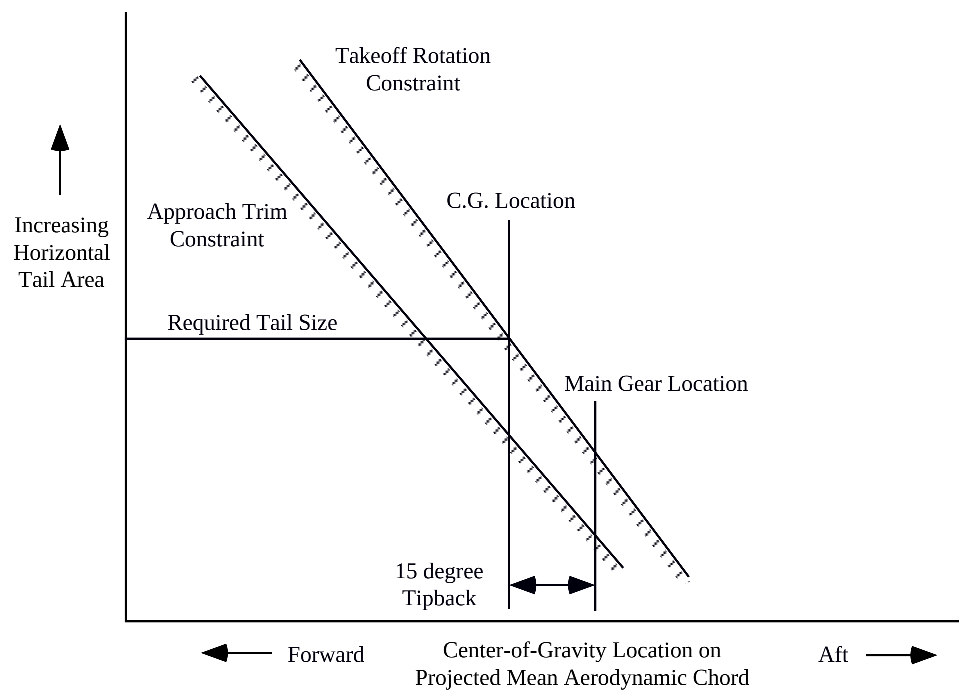

Figure 3. Current tail sizing procedure.

A new method for calculating the range of possible center-of-gravity locations has been proposed for use within optimization by Chai, *et al*[30]. This new method begins by determining an uncertainty *cg* range for each non-movable structural item of the aircraft and a movement range for each piece of service and operational equipment. The range of possible center-of-gravity locations is then calculated by shifting the weight of each item within their respective uncertainty ranges and movement limits. The theory behind this method is that services and operational equipment can be located in multiple places within the aircraft instead of one predefined position. Also, there exists some uncertainty about the actual *cg* location of each structural piece of the aircraft.

Using this method, the range of possible center-of-gravity locations can then be used with the tail sizing diagram to determine the optimum horizontal tail size depending upon the relation between the range of possible *cg* locations, the range between the forward and aft limits, and the required operational *cg* range. If the forward and aft *cg* limits are within the range of possible locations, the horizontal tail size is iteratively increased or decreased during the optimization process so that the required operational range is exactly between the forward and aft limits as shown in Figure 4. If the forward and aft limits are outside of the range of possible center-of-gravity locations, the aircraft configuration must be rearranged by moving the wing, landing gear, or horizontal tail along the aircraft fuselage.

For a realistic and flyable aircraft design, the aircraft center-of-gravity requirements must be addressed during the horizontal tail design process. Without addressing these requirements, the horizontal tail may be undersized or over-sized. If the horizontal tail is under-sized, then the result is a design which does not meet aircraft center-of-gravity requirements and is not flyable. If the horizontal tail is over-sized, the aircraft meets all requirements but the additional size of the horizontal tail adds unnecessary weight and drag which affects performance in terms of range and payload weight. Using the tail sizing process during the optimization, the final result is an overall optimum aircraft design where the horizontal tail is the minimum size required for the aircraft to satisfy all center-of-gravity requirements.

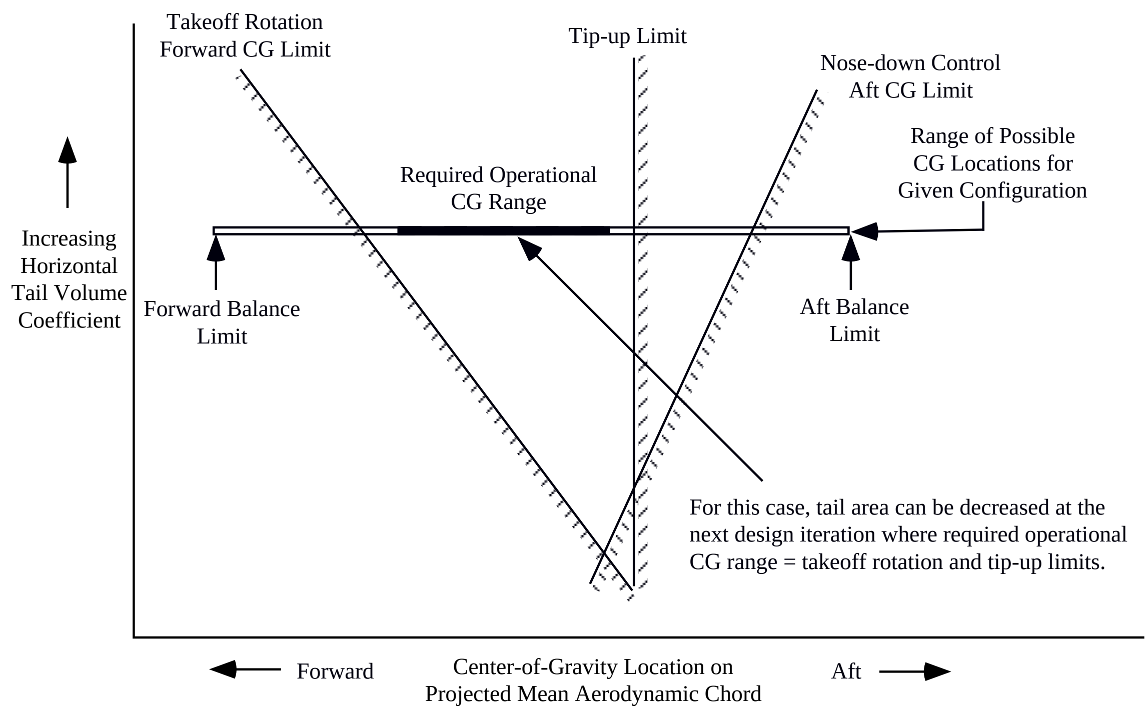

Figure 4. Iterative approach to tail sizing.

3.2 Nose-Down Control

To obtain efficient supersonic flight, the aircraft must be balanced near neutral stability to minimize trim drag. With the use of relaxed static stability, neutral stability can be obtained at supersonic speeds without transferring fuel. However, this will lead to an unstable aircraft at subsonic speeds due to the shift in aerodynamic center with Mach number. An unstable aircraft leads to problems such as pitch departure and deep stall trim from which recovery may be difficult at high angles-of-attack. To overcome this problem, sufficient nose-down moment is needed at any angle-of-attack. A typical pitching moment curve including the maximum nose-down control is shown in Figure 5. The most important portion is where the magnitude of the nose-down moment is a minimum. This is referred to as the "pinch point"[31]. This requirement can make a significant impact on the configuration. The magnitude of the nose-down moment (ΔC_M) at the pinch point is chosen to minimize weight, maximize supersonic performance, and maximize low-speed high angle-of-attack controllability and maneuverability.

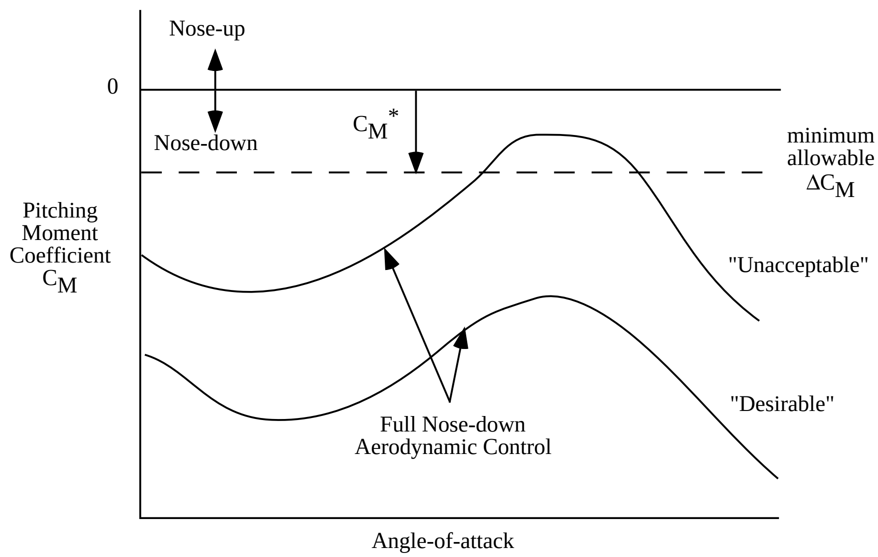

Figure 5. Nose-down control parameter (C_M^*). (Ref. 31).

For tactical aircraft, Ogburn *et al*[32] have proposed nose-down control criteria from a NASA Langley simulator and flight test program. This test program documented pilot acceptability levels of aircraft nose-down control parameters such as pitch acceleration and pitch rate. The pilots performed a pushover from a high angle-of-attack to the recovery angle-of-attack with maximum tail deflection, starting from a 1g stabilized, trimmed, wings-level flight, and maintaining constant thrust throughout the maneuver. The data from this test program suggested the nose-down control design criteria to be 4 deg/sec^2 instantaneous pitch acceleration within 1 second of control input and 5 *deg/sec* instantaneous pitch rate within 2 seconds of control input. The Stability and Control Group at McDonnell Douglas[33] uses this nose-down pitch criteria for determining the aft *cg* limit of their aircraft. For HSCT-type transports, NASA-Langley[34] has discussed possibilities of determining the pitch rate and pitch acceleration at the cockpit of the aircraft instead of using the above guidelines at the aircraft *cg* , since the pilot feels the motion at the cockpit which is a distance away from the *cg* due to the long fuselage. This would relieve the impact of this criteria on the design.

3.3 Stability & Control/Control System Design

Active control technology is used to relax the demand for inherent airframe stability while keeping the aircraft in control by electronic means using rapid response actuators with no input from the pilot. Active control systems provide artificial stability by constantly monitoring disturbances and reacting to counteract any disturbance through the use of feedback control. Using RSS, a significant gain in performance may be achieved if the horizontal tail size is reduced and the longitudinal stability is regained by augmentation. In a conventional aircraft, tail downloads are needed to trim. Using a feedback control system, the inherent longitudinal static stability can be relaxed by shifting the *cg* aft so much that there is negative stability, which can give a significant reduction in tail downloads or even a lifting tail, which reduces wing loads. The benefit at operating at a negative subsonic static margin is that the tail can be smaller with less parasite drag and weight. The result is a reduction in trim drag, an improvement in maneuverability, and a reduction in gross weight.

If active control technology is used, the required horizontal tail size is reduced by decreasing the inherent stability of the aircraft as shown in Figure 6 from Reference 35. While static stability was the constraint previously, the horizontal tail size is now determined by the longitudinal short period frequency, which is a function of the static stability, the control authority limit for nose gear unstick (takeoff rotation control authority limit), and the required *cg* range, as well as the nose-down control power requirement. If the stability level is relaxed using augmentation, the required horizontal tail size is reduced. In the example in Figure 6, the minimum horizontal tail size is achieved at the point which the augmentation system becomes saturated in the presence of gusts. In general, the nose-down control or tip-back limit may also limit the size of the horizontal tail depending on the *cg* requirements. In this example, the wing and main landing gear are moved forward to obtain the minimum horizontal tail size.

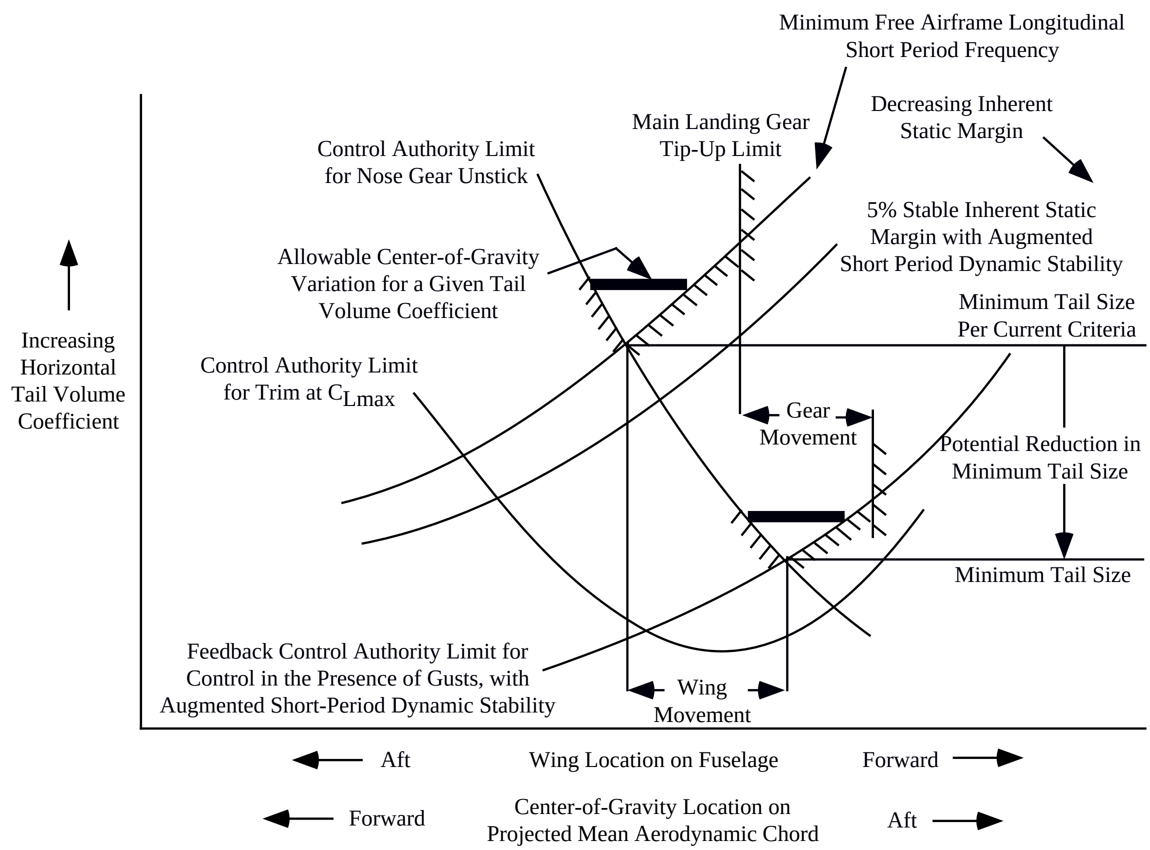

Figure 6. Tail sizing diagram using active control technology. (Ref. 35)

Holloway, *et al*,[36] and Whitford[28] also discuss the benefits on aircraft performance using modern control system technology. Figure 7 is another example of the potential reduction in horizontal tail size if active control technology such as a pitch stability augmentation system is used. For a conventional aircraft, the level of static stability and the required *cg* range determine the size of the horizontal tail. By relaxing the static stability, the size of the horizontal tail is reduced by moving the aft limit of the required *cg* range back to the tip-up limit which is just ahead of the main gear. The resulting negative stability is then regained by augmentation. In any case, the minimum horizontal tail size is chosen to provide adequate trim throughout flight and to assure that the stability augmentation system does not saturate in any anticipated level of turbulence.

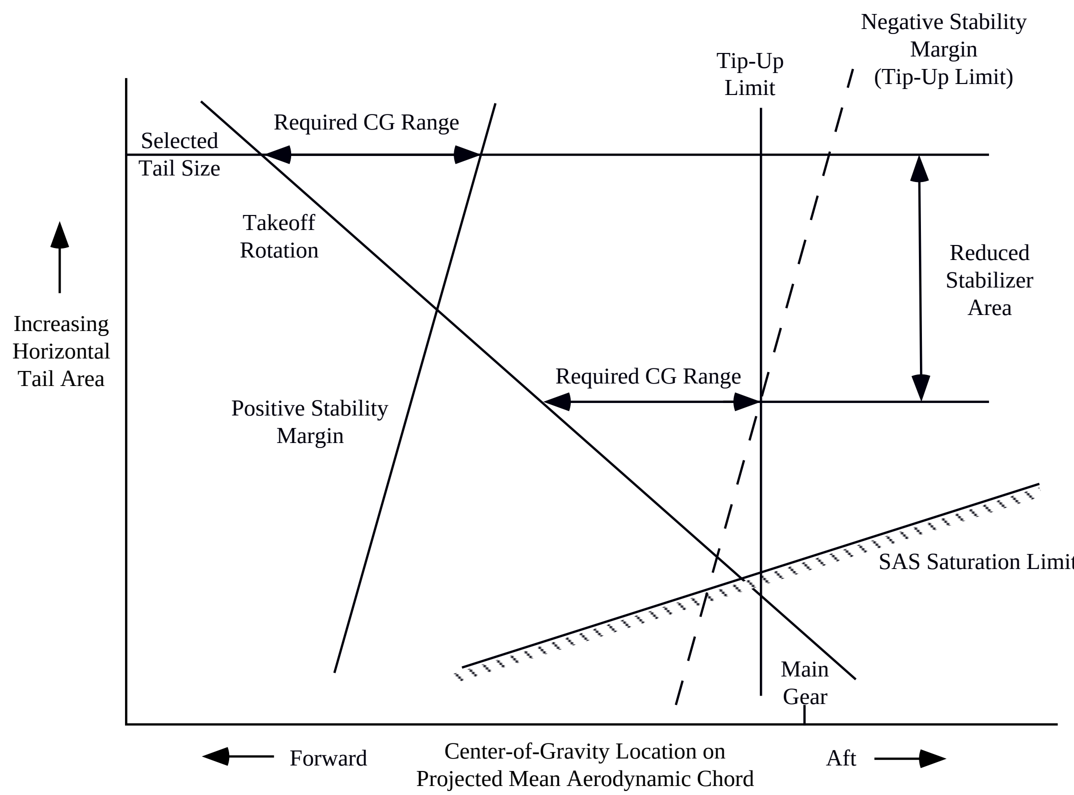

Figure 7. Another tail sizing diagram using active control technology. (Ref. 36).

3.4 Aerodynamic Center Shift

Because of the strong interplay between subsonic control power required and supersonic cruise, we investigated the aerodynamic center (*ac*) shift for HSCT-class aircraft. This study of the aerodynamic center shift was made to investigate the accuracy of the HSCT design code in predicting the aerodynamic center and its shift from subsonic to supersonic speeds. A vortex lattice code contained within the HSCT design code predicted the subsonic aerodynamic center of a cranked-arrow supersonic transport at approximately 50% *mac*. Carlson s program WINGDES[19] was used to compare the aerodynamic center location with the vortex lattice code and predicted the location at approximately 51% *mac* with a small shift of 1% *mac* at a cruise Mach of 2.4 as shown in Figure 8. This shift in aerodynamic center seemed small, especially compared to the *ac* shift from 25% to 50% *mac* of a typical airfoil section. Therefore, a study was conducted to confirm the aerodynamic center location and its small shift at supersonic cruise by investigating other HSCT-type configurations. This section contains a summary of this research.

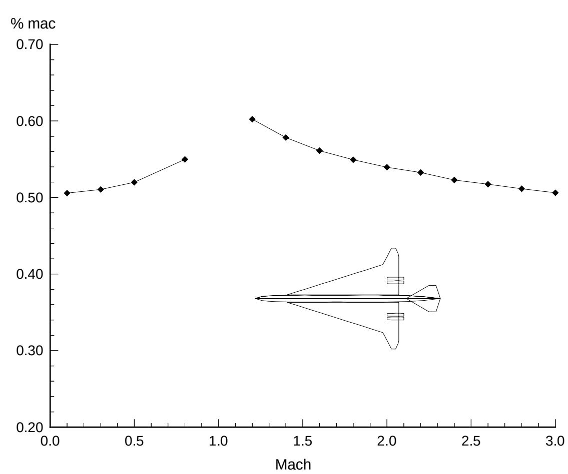

Figure 8. Aerodynamic center shift of an HSCT planform using WINGDES[19].

3.4.1 Background Information

To balance an aircraft for minimum trimmed drag flight, the center-of-gravity range must be located properly relative to the aerodynamic center. The aerodynamic center is the longitudinal location about which no change in moment occurs during a change in angle-of attack, i.e. where only changes in lift take place. The aerodynamic center of a complete aircraft is known as the neutral point. This location is aft or forward of the wing aerodynamic center depending on the configuration. The addition of a fuselage moves the combined aerodynamic center (or neutral point) forward of the wing aerodynamic center, while adding a horizontal tail moves it rearward. For the remainder of this section, the aerodynamic center will refer to the neutral point or combined aerodynamic center.

The aerodynamic center moves aft with an increase in aircraft speed from subsonic to supersonic Mach number. This shift in position is due to a change in pressure distribution which occurs between subsonic and supersonic speeds causing the aerodynamic center to move aft of its subsonic position. This rearward travel in aerodynamic center increases the longitudinal stability of the aircraft and has adverse affects such as reduced maneuverability, increased supersonic trim drag, and increased required size of the control surfaces. Supersonic trim drag is due to the increased nose-down pitching moment which causes the control surfaces to have large deflections to trim.

3.4.2 Past Research

It is desirable to design an airplane so that the shift in aerodynamic center is minimal. Lamar and Alford[37] proposed the use of a normalizing parameter ($\sqrt{S}$) to compare the aerodynamic shift of different planforms. This reference length is independent of the planform, whereas the conventionally used mean aerodynamic chord (*mac*) is dependent on the planform itself. Lamar and Alford used this normalizing parameter to investigate the effects of aspect ratio, wing sweep, taper ratio, notch ratios, and forewings on the aerodynamic center travel of various wings.

As presented in Figure 9, delta wings with varying aspect ratio were used to demonstrate the usefulness of this parameter. In this figure, Δx is the distance between the aerodynamic center location at Mach 0.25 and the aerodynamic center position at any Mach number. The aerodynamic center shift based on the mean aerodynamic chord ($\bar{c}$) shows that the delta wing with the lowest aspect ratio has the smallest incremental change. However, the shift based on √S shows that all three delta wings have the same change across the Mach range.

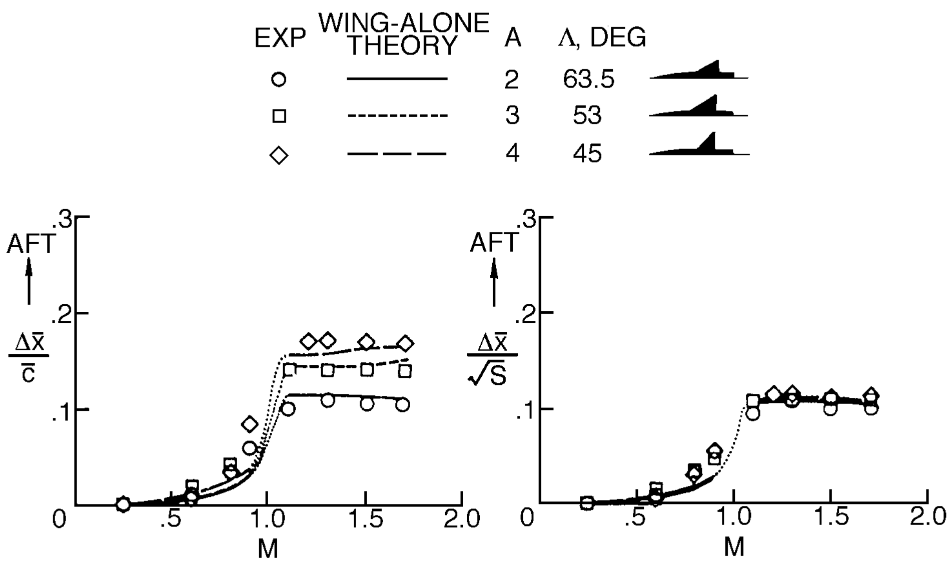

Figure 9. Effect of aspect ratio and sweep (Ref. 37).

Figure 10, also from Reference 37, presents the effect of wing sweep and taper ratio on the aerodynamic center shift. Based on the mean aerodynamic chord ($\bar{c}$), the delta wing has the smallest change. However, based on √S, the delta wing and the sweptback wing have about the same change in aerodynamic center position.

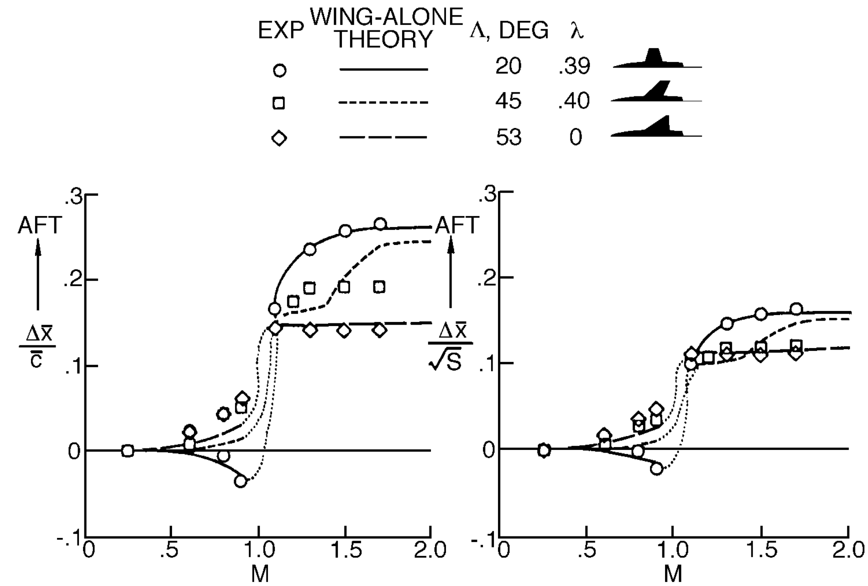

Figure 10. Effect of sweep and taper (Ref. 37).

Figure 11, also from Reference 37, shows the effect of planform variation in sweep, taper ratio, and notch ratios. The wing with the lowest sweep has the smallest shift when the taper ratio is zero for any given notch ratio at Mach 3.0. The planform with the lowest taper ratio has the smallest shift when the wing is swept 60 degrees.

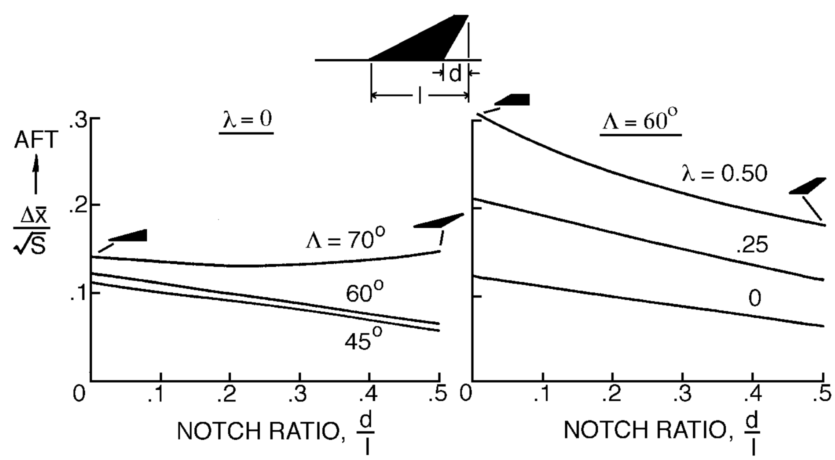

Figure 11. Conventional planform variation (Ref. 37).

One method to reduce the aerodynamic center shift of an arrow wing is to reduce the sweep of the wing tip as presented in Figure 12. Another method to reduce the shift of a delta wing is to add an inboard forewing as shown in Figure 13. The wing with the longest root chord (or most forward apex) has the smallest change in aerodynamic center.

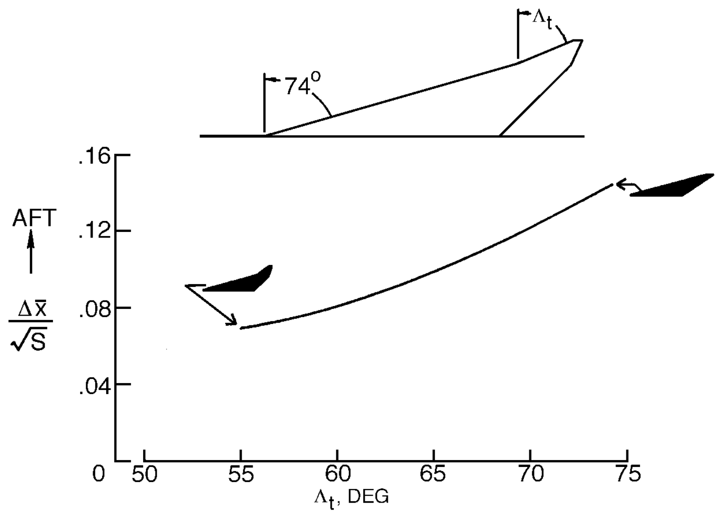

Figure 12. Composite planforms (Ref. 37).

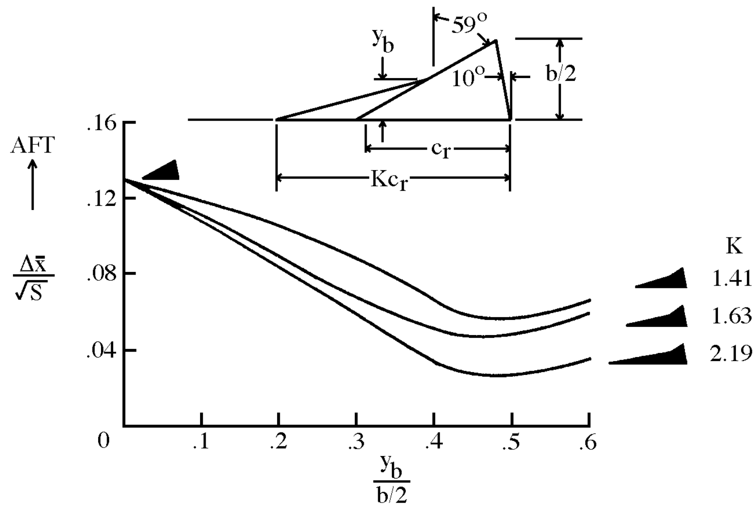

Figure 13. Effect of Leading-Edge Break Location (Ref. 37).

Hopkins, *et al*,[38] have also studied the effects of planform variations on the aerodynamic characteristics of low aspect ratio wings. They concluded that one of the benefits of a cranked delta wing over a delta wing is a smaller shift in aerodynamic center between subsonic and high supersonic Mach numbers. However, the disadvantage is a more severe loss in longitudinal stability, where the pitching moment is linear at low angles-of-attack but not at higher angles-of-attack where the planforms exhibit pitch-up. Benoliel and Mason[7] have developed a method which can estimate pitch-up and will be discussed later in Section 4.

Figure 14 presents the pitching moment results at a Mach number of 0.4. The pitching moment is linear at low angles-of-attack, but not at higher angles-of-attack where the cranked planforms exhibit a severe loss in longitudinal stability. The delta wings shows only a slight loss in longitudinal stability. The constant aspect ratio wings (wings 1-4) show a progressive loss in longitudinal stability as more of the wing leading-edge is extended forward.

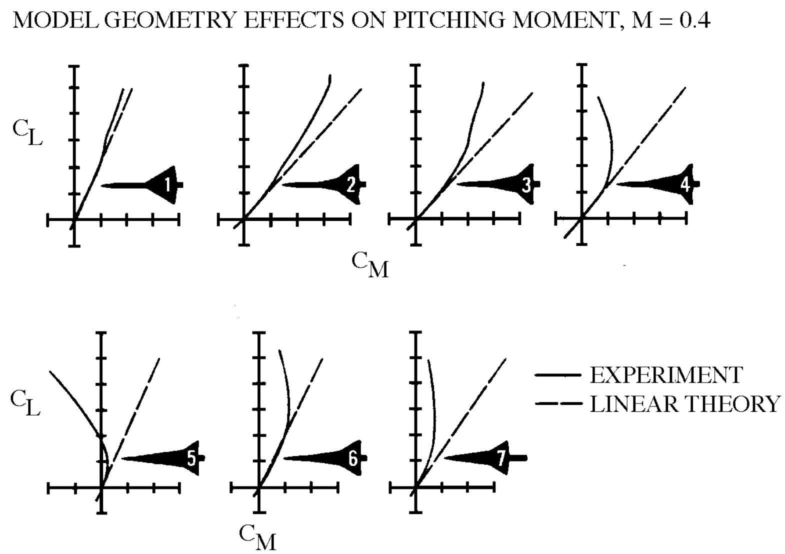

Figure 14. Pitch-up of several wing planforms (Ref. 38).

Figure 15[†] shows that a maximum travel in aerodynamic center of approximately 13 percent chord occurred between subsonic and transonic speeds for all the wing models used in the report. At higher supersonic Mach numbers, the aerodynamic center was about the same or slightly forward of the low subsonic aerodynamic center. For delta wings, the aerodynamic center is considerably behind the subsonic position.

In this figure, $\delta C_M/\delta C_L$ is plotted versus Mach number. The location of the aerodynamic center is calculated as $h_{ac} = h_{ref} - \delta C_M/\delta C_L$.

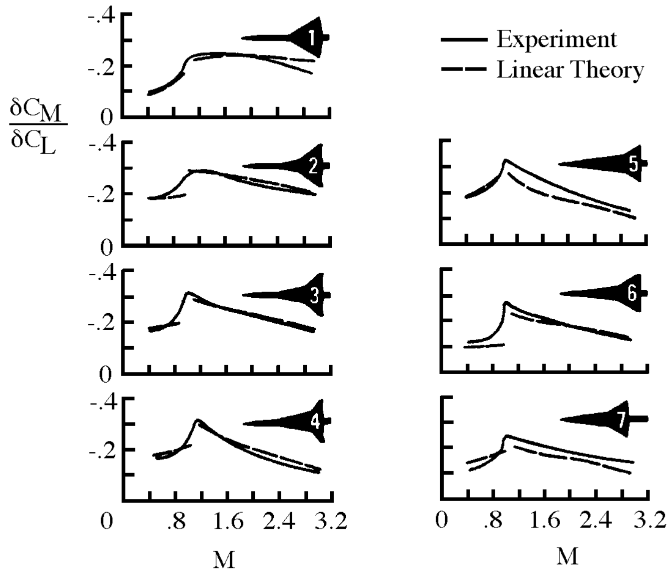

Figure 15. Aerodynamic center travel of different wing planforms. (Ref. 38)

Ray and Taylor[39] and Corlett and Foster[40] performed wind tunnel experiments for an ogee, delta, and trapezoidal wing planform, with and without camber, for a tailless fixed-wing supersonic transport. Two experiments were conducted at a Mach range of 0.4 to 1.14 and 1.80 to 2.86. The cambered planforms were designed for a lift coefficient of 0.1 at a cruise Mach of 2.2. All the planforms had a constant Aspect Ratio of 1.54. As shown in Figure 16, the planform differences had little effect on the aerodynamic center shift in the subsonic and transonic regime. However, in the supersonic regime, the ogee wing exhibited the largest aerodynamic center variation. The delta and trapezoid wing experienced approximately the same shift in aerodynamic center. Also shown in Figure 16, the supersonic aerodynamic center location moves forward after the transonic regime toward the subsonic position with an increase in supersonic Mach number.

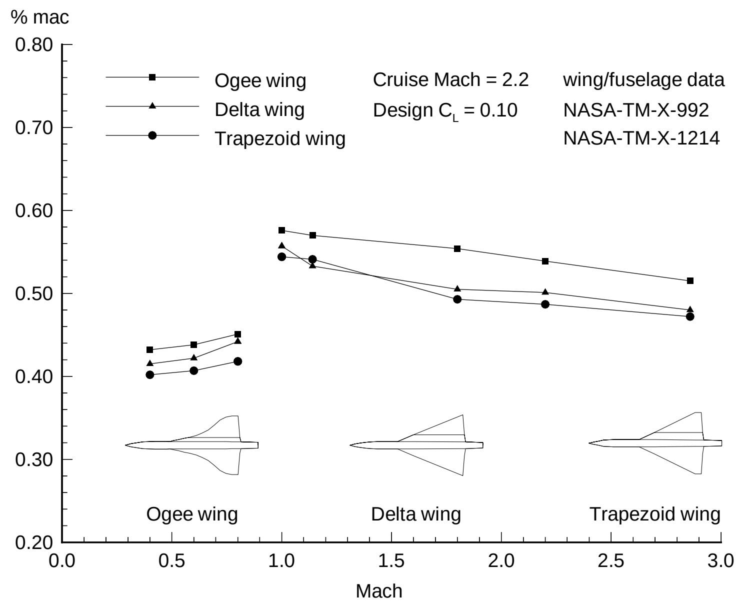

Figure 16. Aerodynamic center shift of three supersonic wings.

Concorde design studies[41] have shown that the advantages of a reduced travel in aerodynamic center are 1) longitudinal trim is easier to obtain, 2) a low static margin both at subsonic speed and supersonic cruise can be reached using a fuel transfer system, and 3) by design of wing camber and twist, it is possible to obtain low elevon angles to trim throughout the flight envelope, which minimizes the supersonic cruise trim drag. In subsonic cruise, the aerodynamic center is approximately 54% of the root chord and the takeoff and landing center-of-gravity is approximately 53.5%. In supersonic cruise at Mach 2.0, the aerodynamic center shifts to approximately 62% of the root chord and the cruise center-of-gravity is at 57% to maintain satisfactory longitudinal stability characteristics.

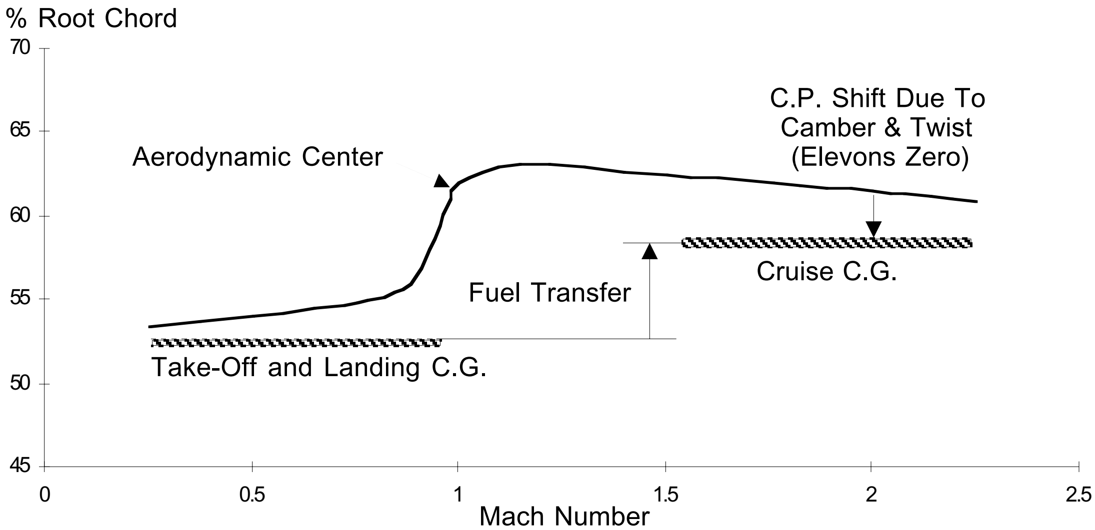

Figure 17. Concorde aerodynamic center shift (Ref. 42).

The aerodynamic center location of two supersonic wings[43-45] is compared to the prediction of WINGDES in Figure 18. These configurations were chosen because the wing planform geometry was specified along with experimental data. As shown in the figure, WINGDES predicted the aerodynamic center within 3% of the *mac*

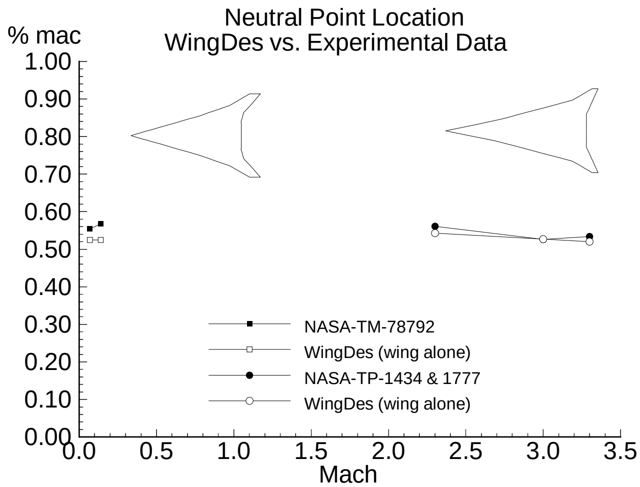

Figure 18. Aerodynamic center comparison for two supersonic wings.

3.4.3 Conclusion

In conclusion, the aerodynamic center location of a HSCT-type wing moves aft slowly until transonic speeds are reached. At this point, the aerodynamic center moves aft more rapidly. The aftmost aerodynamic center location occurs at about a Mach number of 1.0. As the Mach number is increased, the aerodynamic center moves forward at a fairly significant rate at first, but this rate decreases as the Mach number is increased. The aerodynamic center then becomes independent of the Mach number. Here, the aerodynamic center is only slightly aft of the subsonic position. The magnitude and actual trends with Mach number are highly dependent on the planform.

4. Pitch-Up and the APE Method

Low aspect ratio, highly-swept cranked delta wings are typically proposed for high-speed civil transports[46]. These wing planforms are chosen due to the low drag benefits of a highly swept leading-edges, which have poor low-speed aerodynamic characteristics, and a lower sweep outboard section to compensate for this deficiency, which improves the low speed lift/drag ratio and increases the lift curve slope. However, at low speeds these wings are susceptible to pitch-up at modest angles-of-attack (as low as 5°) due to non-linear aerodynamic effects, which include leading-edge vortex flow, outer wing stall, and vortex breakdown[7].

Pitch-up is defined as an abrupt change in the slope of the pitching moment curve with respect to the angle-of-attack ($C_{M\alpha}$) such that the slope of the curve after the pitch-up angle-of-attack is increased. The magnitude of the change in slope of the curve and the pitch-up angle-of-attack vary depending on the aircraft configuration. As identified in a study by Benoliel and Mason[7], pitch-up is a result of the forces generated by the leading-edge vortex inboard, together with flow separation and vortex breakdown on the outer portion of the wing. The strong effects of the leading-edge vortex, and the loss of lift on the outboard wing sections due to flow separation, causes the center-of-pressure to move forward producing the pitch-up behavior. This behavior has yet to be demonstrated by a complete CFD analysis of an HSCT-class wing undergoing pitch-up at low speed.

To estimate the pitch-up of cranked delta and arrow wing planforms, Benoliel and Mason[7] performed a study on planforms that exhibited pitch-up during experimental investigations. Using a vortex lattice type method, *Aero2s*[47], section lift coefficients were plotted for each spanwise station at angles-of-attack near the pitch-up regime for a variety of planforms. It was determined from this study that an equivalent 2-D section lift coefficient limit could be used to model separated flow on the outboard wing panel.

Once this 2-D lift coefficient is exceeded, the total aircraft lift and pitching moment is corrected to include the loss of lift on the outboard wing panel. The resulting Aerodynamic Pitch-up Estimation (APE) method is a computationally inexpensive means of estimating the onset of non-linear aerodynamic characteristics and pitch-up of cranked arrow wings (although still not cheap enough to be included directly within an optimization).

A comparison of the APE method, *Aero2s*, and wind tunnel data for a cambered and twisted cranked arrow wing tested by Yip and Parlett[48] is presented in Figure 19. The results of the APE method, shown with a solid line, is in good agreement with the experimental data and estimates pitch-up of the configuration fairly well. The pitch break occurs at an angle-of-attack of about 6° at a lift coefficient of about 0.24. Many other comparisons were presented by Benoliel and Mason.

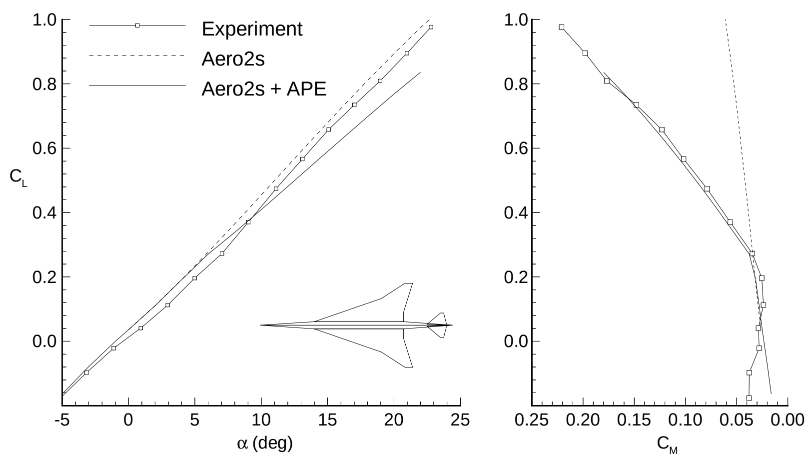

Figure 19. Comparison of lift and pitching moment estimation methods for a 71°/57° swept cambered and twisted wing ($\delta_{tail} = 0°$). (Ref. 48).

5. Nonlinear Pitching Moment Model and Flap Effect Model

In this section, the nonlinear pitching moment and the lift and moment flap effect models are described. The nonlinear pitching moment model will be used during the calculation of the takeoff and landing constraints. The flap effect model will only be used during the takeoff analysis, since we are currently neglecting flaps within the approach analysis.

5.1 Nonlinear Pitching Moment Model

The nonlinear pitching moment model is shown in Figure 20. The difference between a linear relationship in pitching moment with angle-of-attack and the nonlinear pitching moment model is that the slope of the pitching moment curve changes after the pitch-up angle-of-attack. As shown in the figure, three parameters describe the nonlinear behavior with angle-of-attack and include the slope before pitch-up ($C_{M\alpha,1}$), the pitch-up angle-of-attack (α_B), and the slope after pitch-up ($C_{M\alpha,2}$). The pitching moment model also includes a contribution due to tail deflection ($\Delta C_{M\delta e}$) and flap deflection ($\Delta C_{M\delta f}$). The resulting relationship of the pitching moment with angle-of-attack is :

$$C_M = C_{M\alpha,1}\alpha + C_{Mo} + \Delta C_{M\delta e} + \Delta C_{M\delta f} \quad \text{for } \alpha \le \alpha_B$$
$$C_M = C_{M\alpha,2}\alpha + (C_{M\alpha,1} - C_{M\alpha,2})\alpha_B + C_{Mo} + \Delta C_{M\delta e} + \Delta C_{M\delta f} \quad \text{for } \alpha \ge \alpha_B$$

where, the pitching moment at zero angle-of-attack (C_{Mo}) is zero (see Section 2.2).

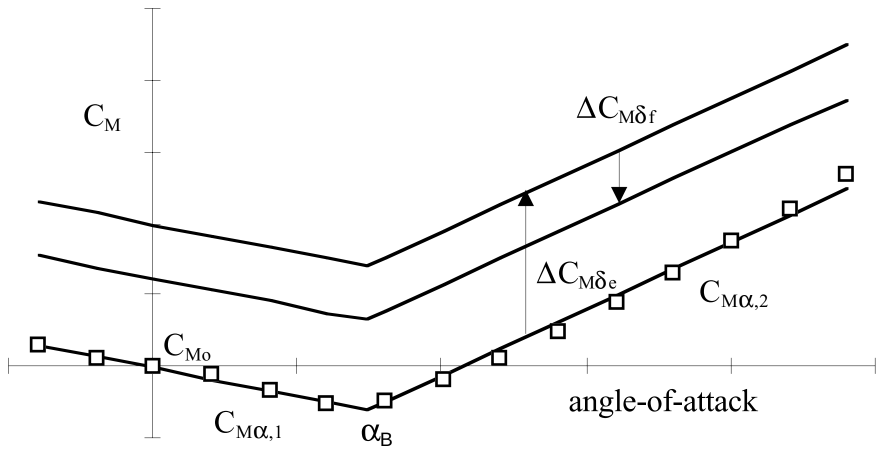

Figure 20. Linear least squares fit of pitching moment data.

5.2 Lift and Moment Flap Effect Model

The flap effect model includes an increment in lift ($\Delta C_{L\delta f}$) and pitching moment ($\Delta C_{M\delta f}$) due to flap deflection, where $\Delta C_{M\delta f}$ is contained within the nonlinear pitching moment model. Since these values are currently fixed throughout the optimization at an approximate value based on investigation of HSCT-class aircraft, an improved model is needed to calculate more accurate values and to include changes in the aircraft geometry.

The increment in lift and moment due to flap deflection ($\check{C}_{M\delta f}$, $\check{C}_{L\delta f}$) are calculated as average values over the entire angle-of-attack range. As shown in Figure 21 from experimental data, the flap effectiveness for the pitching moment is fairly linear throughout the angle-of-attack range. However, the flap effectiveness for the lift is not linear and the effectiveness decreases with an increase in angle-of-attack. For this study, it was assumed that the flap effectiveness for both the lift and pitching moment are linear to simplify the problem. The size of the leading-edge and trailing-edge flaps are modeled as shown in Figure 22.

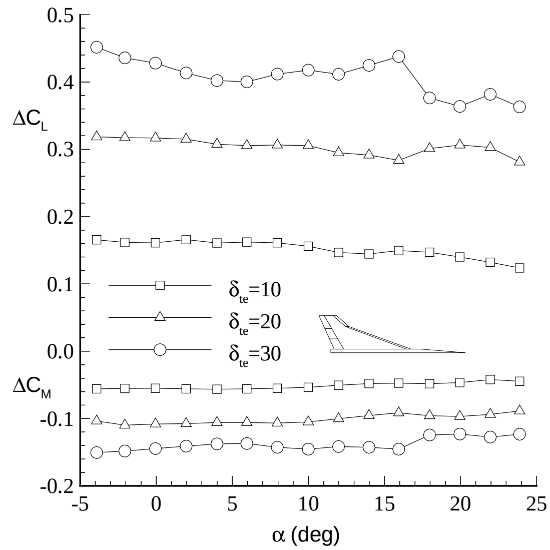

Figure 21. Increments in lift and pitching moment for various trailing-edge flap deflections for a 70°/48.8° sweep flat cranked arrow wing (Ref. 49).

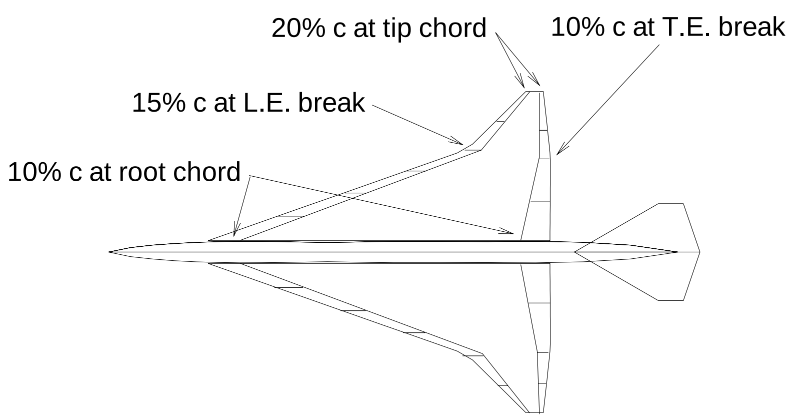

Figure 22. Leading-edge and trailing-edge flaps.

5.3 Estimation Using the APE Method

Two separate analyses by *Aero2s* and the APE method are used to calculate the six parameters ($C_{M\alpha,1}$, α_B, $C_{M\alpha,2}$, $\breve{C}_{M\delta e}$, $\breve{C}_{M\delta f}$, $\breve{C}_{L\delta f}$) at Mach 0.2 and sea level. For both analyses, *Aero2s* and the APE method require information on the wing and flap geometry, horizontal tail geometry, and the deflections of the tail, leading-edge, and trailing-edge flaps. The first analysis deflects the horizontal tail and a linear least squares fit through the resulting pitching moment data is used to calculate $C_{M\alpha,1}$, α_B, $C_{M\alpha,2}$, and $\breve{C}_{M\delta f}$. A second analysis deflects the horizontal tail, leading-edge flaps, and trailing-edge flaps to calculate the average values of the increment in lift and pitching moment due to flap deflection ($\breve{C}_{M\delta f}$, $\breve{C}_{L\delta f}$). Each analysis takes approximately 2 minutes to complete for a single aircraft design.

Since each analysis takes approximately 2 minutes, *Aero2s* and the APE method cannot be directly connected to the optimization. Pitching moment and flap effect information is needed whenever the takeoff and approach constraints are calculated for a given aircraft configuration. In addition, the optimizer evaluates many different designs in order to chose a design with a minimum TOGW which satisfies all of the constraints. As a result, the optimization would take to long to find an optimal solution. Therefore, another method is needed to approximate the results ($C_{M\alpha,1}$, α_B, $C_{M\alpha,2}$, $\breve{C}_{M\delta e}$, $\breve{C}_{M\delta f}$, $\breve{C}_{L\delta f}$) from *Aero2s* and the APE method. Response surface methodology will be used for this purpose.

6. Response Surface Methods

In this section, response surface methodology and its use within optimization is briefly discussed. Response surface methods will be used to approximate the pitch-up and flap effect parameters ($C_{M\alpha,1}$, α_B, $C_{M\alpha,2}$, $\breve{C}_{M\delta e}$, $\breve{C}_{M\delta f}$, $\breve{C}_{L\delta f}$) calculated by *Aero2s* and the APE method. These parameters will be used within the optimization via the nonlinear pitching moment and the lift and moment flap effect models.

6.1 Introduction

Response surface methodology (RSM) is a technique in which empirical models are developed to approximate an unknown function of a set of variables. Based on statistical and design of experiments theory[50], the empirical model known as the response surface model, is constructed by performing a series of numerical experiments and then observing the response (or data) from those experiments. In most cases, the response surface model is a low-order polynomial such as a linear or quadratic function of the variables in interest. For example, a second-order response surface model for n variables has the form:

$$y = c_0 + \sum_{1 \le i \le n} c_i x_i + \sum_{1 \le i \le j \le n} c_{ij} x_i x_j + \varepsilon$$

where x_i are the variables, c_i are the polynomial coefficients, y is the observed response, and ε is the error between the approximation and the true response. For n variables, there are $k = (n + 1)(n + 2)/2$ coefficients in the quadratic polynomial. The polynomial coefficients are typically solved by a least squares fit of the polynomial through the data obtained from the experiments (here they are computer runs). At least $p \ge k$ experiments (analysis runs) are needed to solve for the unknown coefficients. The final result is a regression curve or surface which best approximates the response of an unknown function of a set of variables.

6.2 Response Surface Generation

The first step in generating a response surface model is to determine a set of relevant variables within the problem of interest and to construct a design space by determining the minimum and maximum value of each variable. The second step is to determine an appropriate procedure which selects the number of experiments and the combination of variables within each experiment. Typical design of experiment approaches include factorial and central composite designs[51]. In the factorial design, each variable is assigned a certain number of levels or discretized values where at least three levels are needed to fit a quadratic response surface model. For a three-level factorial design, each variable is assigned a minimum, maximum, and midpoint value and 3^n experiments (or design points with a particular set of variables) are generated. A three-level, three variable factorial design is presented in Figure 23 where 27 design points are shown.

If the problem consists of a large number of variables and 3^n experiments are too many to evaluate, the number of experiments can be reduced using a central composite design of experiment. In this point selection scheme, each variable is assigned an extreme minimum and maximum value yielding 2^n experiments. In addition, $2n$ experiments are generated by assigning a single variable at a time to its minimum and maximum value multiplied by a scaling factor and keeping the rest of the variables at their midpoint value. The final experiment consists of the midpoint or center design. A three variable central composite design is presented in Figure 24 where 15 design points are shown.

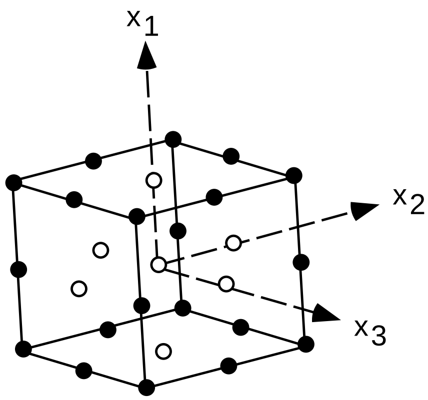

Figure 23. A three-level three variable factorial design (27 points).

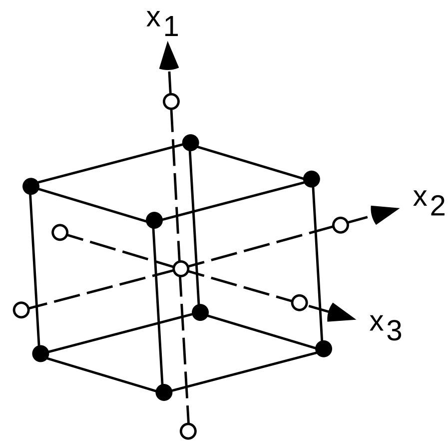

Figure 24. A three variable central composite design (15 points).

If the number of experiments is still too large to evaluate, then D-optimality criterion[52] can be used to choose a user-selected number of points, where the number of experiments is at least the number of coefficients in the response surface model. D-optimality has also been shown to be useful in selecting experiments within irregularly shaped design spaces[53]. In most problems, irregularly shaped design spaces are developed by constraining certain portions of the cuboidal design space due to the nature of the problem.

The final step in the response surface model generation is to evaluate each experiment or set of variables. Using the data obtained from these evaluations, a least squares method is used to determine the coefficients of the response surface model. The response surface model is then evaluated by observing how well it approximates the true function or response. This is achieved by calculating the R-squared of the least squares fit. This value estimates the proportion of the variation in the response around the mean that can be attributed to terms in the response surface model rather than to random error.

It is also the square of the correlation between the actual and predicted response. A value of 1.0 symbolizes a perfect fit (errors are all zero) of the model throughout the data points.

6.3 Response Surface Models Within Optimization

Response surfaces are used in derivative-based optimization to counteract the adverse affects of numerical noise by creating smooth, polynomial models for the noisy results. Without numerical noise to inhibit optimization, a globally optimal design is easily found. Response surface models also have the added benefit of being extremely inexpensive to calculate during optimization. Therefore, RSM is used to approximate the results obtained from computationally expensive analyses, even though the expensive analyses may not produce numerical noise.

Figure 25 diagrams the procedure used to incorporate response surface models into the optimization process. A set of design variables which are affected by the particular problem are selected and the boundaries of the feasible design space are determined around a baseline or initial HSCT design. A point selection scheme is used to determine a small number of HSCT configurations which best describes the overall feasible design space. These HSCT configurations are then analyzed. This step in the procedure is the most time consuming and parallel computing can be efficiently used if available. The results of the analyses are used to generate response surface models using the method of least squares. The response surface models are then substituted into the optimization and an optimization is performed until all constraints are satisfied. If the errors are significant between the response surface approximation and actual analysis at the final design, the process is repeated by shrinking or traversing the boundaries of the design space around this final design, in hopes of an increase in accuracy of the response surface approximations within this new region.

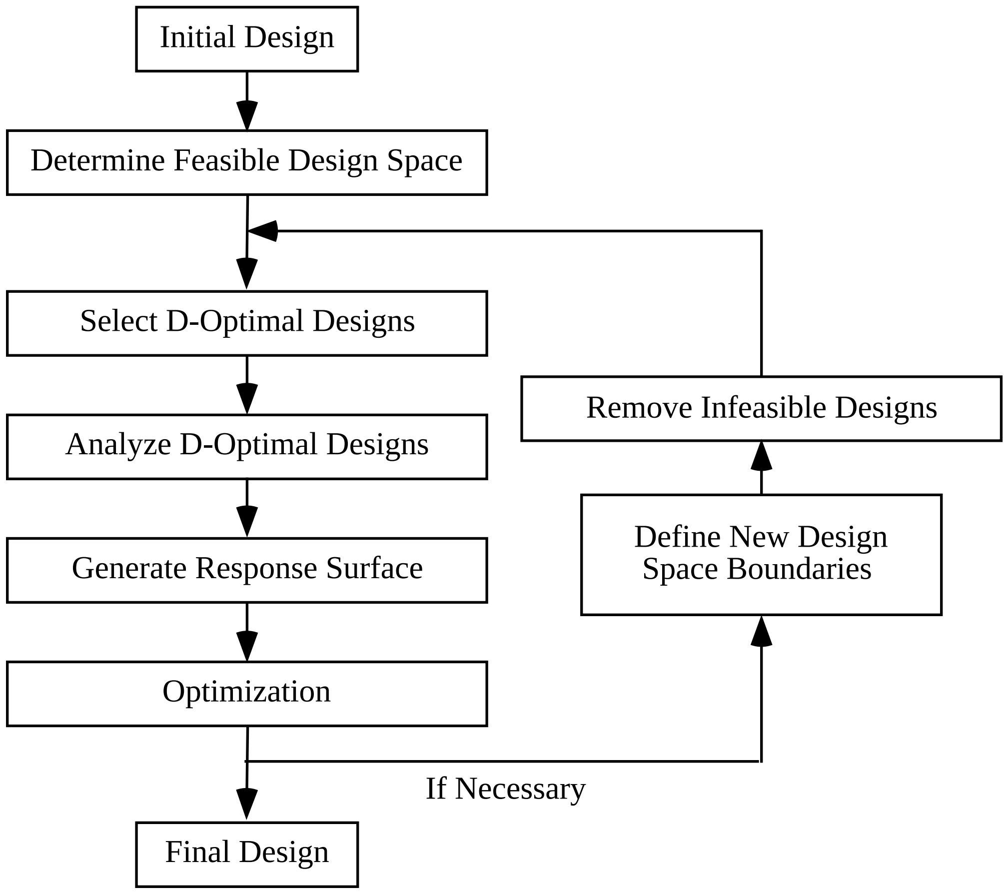

Figure 25. Response surface procedure.

7. Response Surface Approximation For Pitch-up and Flap Effect Parameters

In this study we apply response surface methodology to approximate the pitch-up and flap effect parameters ($C_{M\alpha,1}$, α_B, $C_{M\alpha,2}$, $\breve{C}_{M\delta e}$, $\breve{C}_{M\delta f}$, $\breve{C}_{L\delta f}$) calculated by *Aero2s* and the APE method. The resulting response surface approximations will be then used within the optimization instead of directly calculating the above parameters using *Aero2s* and the APE method.

7.1 Design Variable Selection

Nine of the 29 HSCT design variables (Table 1) were found to have an impact on the results calculated by the Aerodynamic Pitch-up Estimation (APE) method and therefore were used to develop the response surface models. These design variables included the horizontal tail and wing planform variables: wing root chord, wing tip chord, wing span, locations of the wing leading-edge and trailing-edge break points, and the location of the leading-edge of the wing tip (Figure 1). The remaining HSCT design variables were ignored in the development of the response surfaces.

7.2 Feasible Design Space

From a previous study[5], the reasonable design space was identified by constructing a large hypercube defined by varying three of the twenty-five[‡] geometric design variables (Table 1) at a time around the baseline design. A reasonable design refers to a design where all the geometric constraints are acceptable even though some of the aerodynamic and performance constraints are violated. Using this technique, 19,651 configurations were found on the boundary of the domain. A large percentage of these

---

Twenty-five variables were used in the study in Ref. 5 since they affected the wing bending material weight for which a response surface approximation was generated.

configurations violated one or more of the HSCT s geometric constraints and therefore were unreasonable. Instead of eliminating unreasonable designs, a series of increasingly expensive criteria (Table 6) were used to move the candidate designs towards the reasonable design space. The final result is a series of candidate designs that surround the reasonable design space resulting in a more accurate response surface. The candidate designs for this study were chosen from the 19,651 points which were unique to this nine design variable pitching moment problem resulting in 835 candidate design points. Of these 835 candidate designs, 138 D-optimal designs were selected to generate quadratic, nine variable response surface model. This number of D-optimal designs was selected since at least 55 designs are needed to solve a 55 coefficient, quadratic, nine variable response surface model. In this case, 2.5 times the amount were selected.

Table 6. Criteria for reasonable designs (Ref. 5).

#	Description
1-34	HSCT geometric constraints (Table 2)
35-36	20,000 *lbs* < wing bending material < 120,000 *lbs*
37-58	Minimum fuselage radius
59	Inboard Λ_{LE} > Outboard Λ_{LE}
60	$\Lambda_{LE} > 0$
61-62	5,000 *sq. ft* < wing area < 15,000 *sq. ft*
63-64	1.0 < aspect ratio < 3.2
65	Inboard $\Lambda_{TE} < 40°$
66-83	$c_{y,i+1}/c_{y,i} < 1.0$
84	Approximate range > 5,000 *n.mi.*

7.3 Response Surface Generation

The above six parameters ($C_{M\alpha,1}$, α_B, $C_{M\alpha,2}$, $\breve{C}_{M\delta e}$, $\breve{C}_{M\delta f}$, $\breve{C}_{L\delta f}$) were calculated for each D-optimal aircraft configuration. The resulting data was used to determine the coefficients of the response surface models for each of the six desired responses. Table A-

1 presents the coefficient values for each response. To generate the actual response surface, the corresponding coefficients can be substituted into the following nine-variable, quadratic response surface model:

$$
\begin{aligned}
f(x_1, x_2, x_3, x_4, x_5, x_6, x_7, x_8, x_9) = {} & c_0 + c_1x_1 + c_2x_2 + c_3x_3 + c_4x_4 + c_5x_5 + \\
& c_6x_6 + c_7x_7 + c_8x_8 + c_9x_9 + c_{11}x_1^2 + c_{12}x_1x_2 + c_{13}x_1x_3 + c_{14}x_1x_4 + c_{15}x_1x_5 + \\
& c_{16}x_1x_6 + c_{17}x_1x_7 + c_{18}x_1x_8 + c_{19}x_1x_9 + c_{22}x_2^2 + c_{23}x_2x_3 + c_{24}x_2x_4 + c_{25}x_2x_5 + \\
& c_{26}x_2x_6 + c_{27}x_2x_7 + c_{28}x_2x_8 + c_{29}x_2x_9 + c_{33}x_3^2 + c_{34}x_3x_4 + c_{35}x_3x_5 + \\
& c_{36}x_3x_6 + c_{37}x_3x_7 + c_{38}x_3x_8 + c_{39}x_3x_9 + c_{44}x_4^2 + c_{45}x_4x_5 + c_{46}x_4x_6 + \\
& c_{47}x_4x_7 + c_{48}x_4x_8 + c_{49}x_4x_9 + c_{55}x_5^2 + c_{56}x_5x_6 + c_{57}x_5x_7 + c_{58}x_5x_8 + \\
& c_{59}x_5x_9 + c_{66}x_6^2 + c_{67}x_6x_7 + c_{68}x_6x_8 + c_{69}x_6x_9 + c_{77}x_7^2 + c_{78}x_7x_8 + \\
& c_{79}x_7x_9 + c_{88}x_8^2 + c_{89}x_8x_9 + c_{99}x_9^2
\end{aligned}
$$

where, x_1 = wing root chord,

x_2 = wing leading-edge break (x location),

x_3 = wing leading-edge break (y location),

x_4 = wing trailing-edge break (x location),

x_5 = wing trailing-edge break (y location),

x_6 = leading-edge of wing tip (x location),

x_7 = wing tip chord,

x_8 = wing semi-span, and

x_9 = horizontal tail area.

Each response surface model was evaluated to determine how well it fit the actual data. A statistical parameter known as the R-squared value was used for this purpose.

Table 7 lists the R-squared, adjusted R-squared, root mean square error, the mean of the response, and the number of observations (design evaluations) for each response surface model. The R-squared value estimates the proportion of the variation in the response around the mean that can be attributed to terms in the response surface model rather than to random error. It is also the square of the correlation between the actual and predicted response. A value of 1.0 symbolizes a perfect fit (errors are all zero) of the model throughout the data points. The next value in Table 7 adjusts the R-squared value to make it more comparable over models with different numbers of parameters. The root mean square error estimates the standard deviation of the random error. The mean of the response is the overall mean of the response values. The number of observations is the total number of design evaluations used in the fit.

As presented in Table 7, the response surface models for the pitching moment slope before pitch-up ($C_{M\alpha 1}$), slope after pitch-up ($C_{M\alpha 2}$), lift increment due to flap deflections ($\Delta C_{L\delta f}$) and the pitching moment increment due to flap deflections ($\Delta C_{M\delta f}$) fit the data very well since their R-squared values are all greater than 0.94, which is close to a perfect correlation value of 1.0. The response surface models for the pitch-up angle-of-attack (α_B) and the pitching moment increment due to tail deflection ($\Delta C_{M\delta e}$) did not fit as well as the other response surface models with R-squared values less than 0.90. This is attributed to noise or randomness in the data and to the nature of the unknown true response which is not a true quadratic polynomial function of the design variables.

Table 7. Response surface fit.

	Pitch-up Response Surfaces			Tail & Flap Response Surfaces		
	$C_{M_{\alpha,1}}$	α_B	$C_{M_{\alpha,2}}$	ˇ$C_{M\delta e}$	ˇ$C_{L\delta f}$	ˇ$C_{M\delta f}$
R-squared	0.988538	0.881350	0.950256	0.894273	0.940473	0.955996
Adjusted R-squared	0.981081	0.804155	0.917893	0.825486	0.901744	0.927367
Root mean square error	0.000194	0.930877	0.000332	0.009637	0.007593	0.003491
Mean of response	-0.00064	7.621623	0.002319	0.068936	0.196638	-0.05014
Observations	138	138	138	138	138	138

Figures B-1 through B-6 provide examples of the response surface fit of each response surface model by comparing the response surface to actual data through the design space. For each response surface model, a single design variable is allowed to vary from its minimum to maximum values while holding the other eight variables constant at their baseline values listed in Table 1. In a sense, we are taking cuts through the design space.

8. HSCT Design Optimizations

Several HSCT design optimizations were performed with and without the response surface approximations for the pitch-up and flap effect parameters. These parameters were included within the analysis of the takeoff and landing constraints. The entire sequence of optimizations is presented in Figure 26. The baseline design shown at the top of the figure is used as a starting design for each optimization. This design is a former HSCT configuration previously thought to be optimal by Dudley *et al*[4], but does not currently satisfy all of the constraints due to modifications and improvements to our analysis methods. The optimizations labeled without response surfaces were completed using the original methods within the design code, which include a linear relationship between pitching moment and angle-of-attack and a constant approximation of the flap effects. The remaining optimizations were performed with various response surface models substituted into the optimization process as listed in Table 8. In Case E, new response surface models were generated within a reduced design space around Case D and used during the optimization.

Table 8. List of response surface models used in each optimization.

	Response Surface Models					
Optimization	$C_{M\alpha,1}$	α_B	$C_{M\alpha,2}$	˘$C_{M\delta e}$	˘$C_{M\delta f}$	˘$C_{L\delta f}$
Case A						
Case B	3					
Case C	3	3	3			
Case D	3	3	3	3	3	3
Case E	3	3	3	3	3	3

Additional constraints were added to the optimization to keep the optimizer within the response surface design space. The purpose was to reduce any exploitation of the response surface by the optimizer which may drift into regions where the response

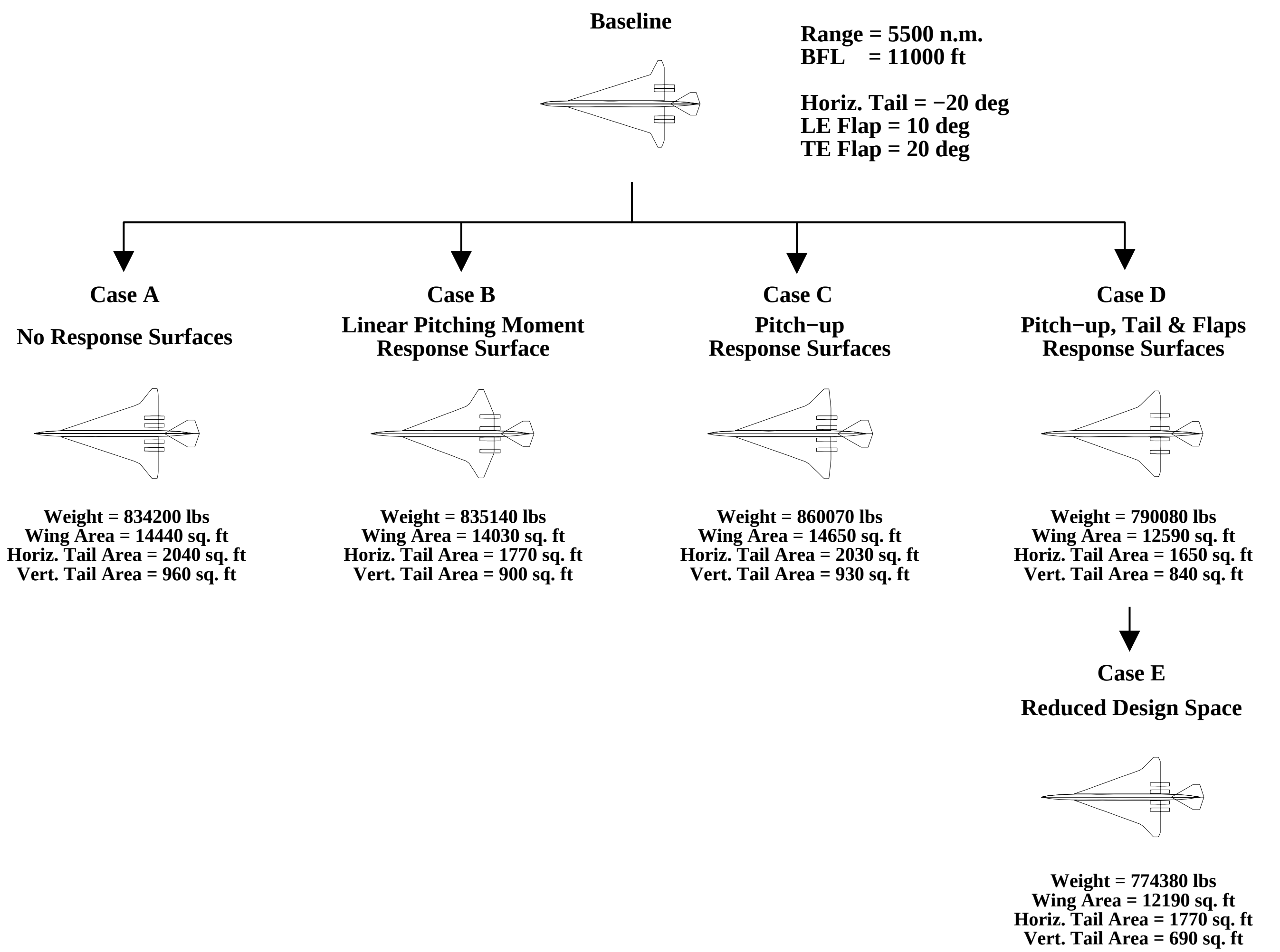

Figure 26. Series of HSCT optimization with and without response surfaces.

surface is invalid. By evaluating the values of the design variables for each D-optimal design, a minimum and maximum constraint value was established for each of the nine design variables related to the pitching moment and pitch-up. Additionally, the geometrically reasonable design constraints of Table 6 were included in the optimization, except for the wing bending material weight constraints. The total number of constraints increased from 69 to 111 and are listed in Table 9.

Table 9. Additional constraints.

#	Description
1-69	HSCT constraints (Table 3)
70-71	min $x_1 < x_1 <$ max x_1
72-73	min $x_2 < x_2 <$ max x_2
74-75	min $x_3 < x_3 <$ max x_3
76-77	min $x_4 < x_4 <$ max x_4
78-79	min $x_5 < x_5 <$ max x_5
80-81	min $x_6 < x_6 <$ max x_6
82-83	min $x_7 < x_7 <$ max x_7
84-85	min $x_8 < x_8 <$ max x_8
86-87	min $x_9 < x_9 <$ max x_9
88-89	5,000 *sq. ft* < wing area < 15,000 *sq. ft*
90-91	1.0 < aspect ratio < 3.2
92	Inboard $\Lambda_{TE} < 40°$
93	Inboard $\Lambda_{LE} >$ Outboard Λ_{LE}
94	$\Lambda_{LE} > 0$
95-111	$c_{y,i+1}/c_{y,i} < 1.0$

8.1 Case A

As previously mentioned, the baseline design does not satisfy all of the constraints due to modifications and improvements to the design code. This optimization was performed to obtain an optimal design which satisfies the most recent modifications to the code by MacMillin[8] without using response surface models. Table 10 lists the weight data, planform geometry characteristics, and performance data on the initial design.

Table 10. Initial design data.

Weight Data	
Gross weight, *lbs*	700097
Wing weight, *lbs*	110979
Fuel weight, *lbs*	322617
Fuel/Gross	0.46
Planform Geometry	
Root chord, *ft*	181.5
Tip chord, *ft*	7.0
Wing area, *sq ft*	13437
Wing span, *ft*	163.8
Aspect ratio	2.0
Horizontal tail area, *sq ft*	1426.1
Vertical tail area, *sq ft*	697.8
LE sweep, inboard	72.5¡
LE sweep, outboard	27.2¡
Performance Data	
Range, *n. mi.*	4709
Balanced field length, *ft*	8807
Max thrust/engine, *lbs*	52009
Landing angle-of-attack	9.9¡
$(L/D)_{max}$	9.1

For this study[§], the takeoff configuration included horizontal tail, leading-edge flaps, and trailing-edge flaps deflections of -20 degrees, 10 degrees, and 20 degrees respectively. Since response surface models were not included, the increment of pitching moment due to tail deflection ($\Delta C_{M\delta e}$) was calculated using the code, JKayVLM[16]. This value was updated approximately every five cycles and was scaled using variable complexity modeling. In addition, the longitudinal derivatives for the flaps ($\Delta C_{L\delta f}$, $\Delta C_{M\delta f}$) were constant at the values prescribed in Section 2.3.

The initial baseline design violated the range constraint, two thrust constraints, the takeoff rotation constraint, nacelle spacing constraint, and the engine out stability constraint. After 27 optimization cycles, the final design increased 134,000 *lbs* to a final TOGW of 834,000 *lbs* with all the constraints satisfied. A convergence history of the TOGW, range, balanced field length, planform design variables, and horizontal tail area are shown in Figure 27. Table 11 lists the weight data, planform geometry characteristics, and performance data on the optimal design.

Since the most heavily weighted constraint is the range constraint, the wing area increased 1,000 ft^2 with an additional wing weight of 22,100 *lbs*, the fuel increased 106,400 *lbs*, and the lift-to-drag ratio (*L/D*) increased to 9.4 to obtain the required mission range of 5,500 nautical miles. In addition, the vertical tail size increased 260 ft^2 to satisfy the engine out stability requirement. The horizontal tail size increased 620 ft^2 to satisfy the balanced field length and time-to-rotate constraints. The inboard engine also moved inboard to satisfy the nacelle spacing constraint.

[§] In MacMillin s report[8], he performed optimizations with a trailing-edge flap deflection of 30 degrees. Preliminary analysis using response surface models within this study resulted in designs that could not satisfy the balanced field requirement. Therefore, trailing-edge deflections of 20 degrees were used. Appendix C includes a comparison between two optimizations with different trailing-edge flap deflections.

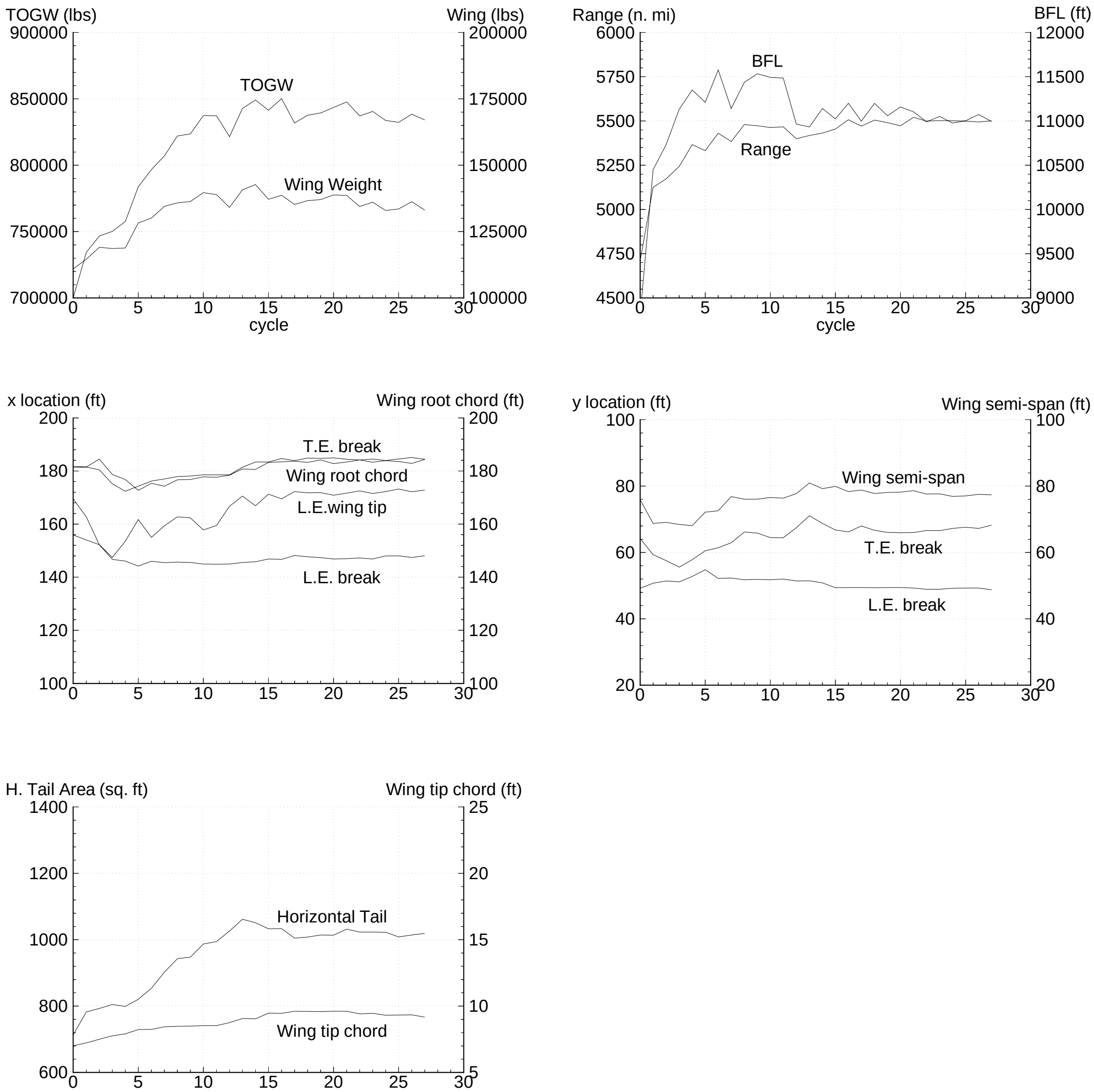

Figure 27. Design history for Case A.

Table 11. Results for Case A.

Weight Data	
Gross weight, *lbs*	834195
Wing weight, *lbs*	133118
Fuel weight, *lbs*	429059
Fuel/Gross	0.51
Planform Geometry	
Root chord, *ft*	184.4
Tip chord, *ft*	9.2
Wing area, *sq ft*	14435
Wing span, *ft*	166.8
Aspect ratio	1.9
Horizontal tail area, *sq ft*	2037.8
Vertical tail area, *sq ft*	957.7
LE sweep, inboard	71.8¡
LE sweep, outboard	40.8¡
Performance Data	
Range, *n. mi.*	5501
Balanced field length, *ft*	10995
Max thrust/engine, *lbs*	53792
Landing angle-of-attack	10.6¡
$(L/D)_{max}$	9.4

To investigate the effect of pitch-up, the balanced field length, time-to-rotate during takeoff, and the approach trim deflection constraints (which all require pitching moment information) were investigated with and without the pitch-up behavior. Table 12 lists the values of each constraint using two different pitching moment models. The balanced field length, time-to-rotate, and approach trim deflection were initially calculated assuming the following linear relationship between the pitching moment and angle-of-attack:

$$C_M = C_{M\alpha}\alpha + C_{Mo} + \Delta C_{M\delta e} + \Delta C_{M\delta f}$$

This model was used with C_{M_α} calculated from both the original subsonic aerodynamic analysis methods within the design code and *Aero2s* with the APE method. Finally, the constraints were calculated assuming the following nonlinear relationship of the pitching moment with angle-of-attack, where the slope changes after the pitch-up angle-of-attack:

$$C_M = C_{M\alpha,1}\alpha + C_{Mo} + \Delta C_{M\delta e} + \Delta C_{M\delta f} \quad \text{for } \alpha \le \alpha_B$$

$$C_M = C_{M\alpha,2}\alpha + (C_{M\alpha,1} - C_{M\alpha,2})\alpha_B + C_{Mo} + \Delta C_{M\delta e} + \Delta C_{M\delta f} \quad \text{for } \alpha \ge \alpha_B$$

Aero2s and the APE method were used to estimate $C_{M\alpha,1}$, α_B, and $C_{M\alpha,2}$.

Table 12. Pitch-up Comparison (Case A).

	BFL (*ft*)	Time to Rotate (*sec*)	Approach Trim (*deg*)
$C_{M\alpha}$ (original design code)	10971	4.9	4.1
$C_{M\alpha}$ (*Aero2s* + APE)	10976	4.9	5.1
Pitch-up - $C_{M\alpha,1}$, α_B, $C_{M\alpha,2}$ (*Aero2s* + APE)	10976	4.9	2.8

The small differences in the takeoff constraints and the change in the approach trim constraint can be explained by investigating the pitching moment curves for the takeoff and landing configurations. The aerodynamic pitching moment about the wing aerodynamic center for the takeoff configuration is plotted in Figure 28. As shown in the figure, the differences in the pitching moment are very small up to the takeoff attitude of 8.5 degrees. As a result, the balanced field length and time-to-rotate will be approximately the same. The total pitching moment needed to be trimmed out by the tail during approach is plotted in Figure 29. This pitching moment is due to the lift, drag, thrust, and weight about the center-of-gravity. As shown in the figure, pitch-up actually reduces the amount of deflection needed to trim at an angle-of-attack of 10.5 degrees.

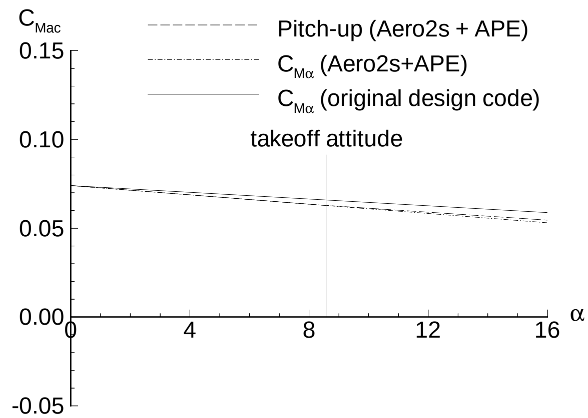

Figure 28. Takeoff pitching moment (Case A).

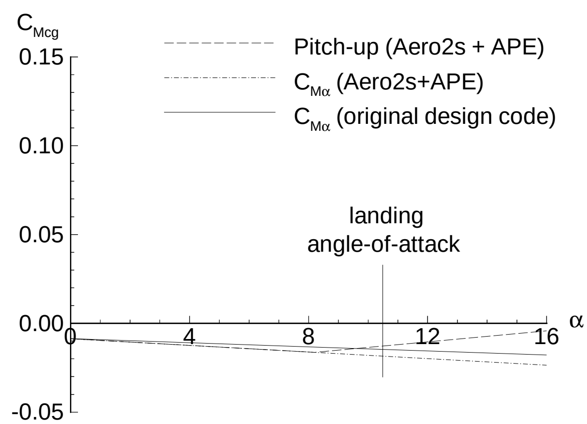

Figure 29. Landing pitching moment (Case A).

Although we did not include the nose-down control margin as a constraint within this study, we investigated the possible impact it may have on the design. As discussed in Section 3.2, the most important portion of the pitching moment curve including the maximum nose-down control is where the magnitude of the nose-down moment is a minimum. This is referred to as the pinch point . Since pitch-up decreases the negative pitching moment at angles-of-attack above pitch-up, the pinch point criteria may become important. Using the suggested nose-down control design criteria as 4 *deg/sec*^{2}

instantaneous pitch acceleration, the pinch point (C_M^*) was calculated as:

$$C_M^* = \frac{\dot{q}\, I_{yy}}{qS\bar{c}} = \frac{-4.0\,\text{deg/sec}^2\; I_{yy}}{qS\bar{c}}$$

As presented in Figure 30, the aircraft does not reach the minimum nose-down control margin at angles-of-attack near the landing angle-of-attack. However, it may be required to maintain adequate nose-down control at much higher angles-of-attack, such as 24 or 28 degrees. In this case, the minimum nose-down control margin may be critical. The figure also shows that pitch-up does affect nose down control since it decreases the negative pitching moment above the pitch-up angle-of-attack.

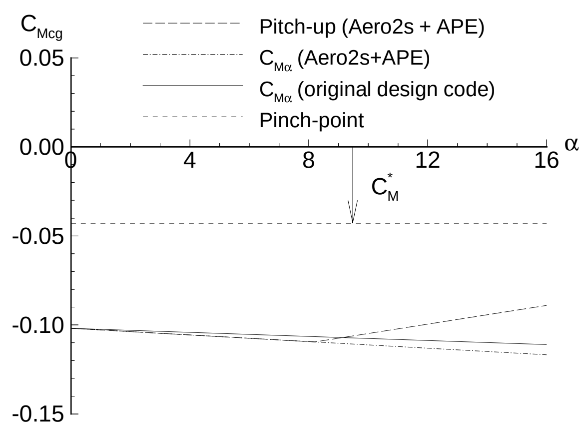

Figure 30. Nose-down pitching moment (Case A).

8.2 Case B

This optimization used the linear relationship between the pitching moment and the angle-of-attack. However, a response surface model for the pitching moment curve slope ($C_{M\alpha}$) was used instead of calculating the value directly within the design code using variable-complexity modeling. Since a response surface model was included, the number of constraints was increased from 69 to 111 as listed in Table 9. As in the previous optimization, the increment in pitching moment due to tail deflection ($\Delta C_{M\delta e}$) was calculated by JKayVLM and the increment in lift and pitching moment due to flap deflection ($\Delta C_{L\delta f}$, $\Delta C_{M\delta f}$) were held constant. To reiterate, the major difference in this optimization is that the slope of the pitching moment curve is provided by a response surface model and not calculated by the aerodynamic models inside the design code.

The same initial design is used in this optimization. After 50 optimization cycles, the TOGW increased to 835,100 *lbs* with all the constraints satisfied. A convergence history of the TOGW, range, balanced field length, planform design variables, and horizontal tail area are shown in Figure 31. As shown in the figure, the convergence history is still noisy even though we replaced one aerodynamic model with a smooth response surface model. Studies into disagregating the entire code into different response surface models are currently being conducted which will remove all or most of the noise within the design code. Table 13 lists the weight data, planform geometry characteristics, and performance data on the optimal design.

As shown in Figure 26, the final design of Case B has an unusual planform with the trailing-edge swept forward. The driving constraints for this problem were the engine-out stability constraint and the two thrust constraints. As shown in the convergence history, the wing trailing-edge break location (TE break) was moved inboard and the leading-edge wing tip (LE wing tip) was moved forward to decrease the wing weight and overall TOGW. Since we are solving for a minimum weight design, the optimizer chose to decrease the TOGW by designing a lighter wing instead of increasing the size of the engines, which would increase the weight, to satisfy the thrust constraints.

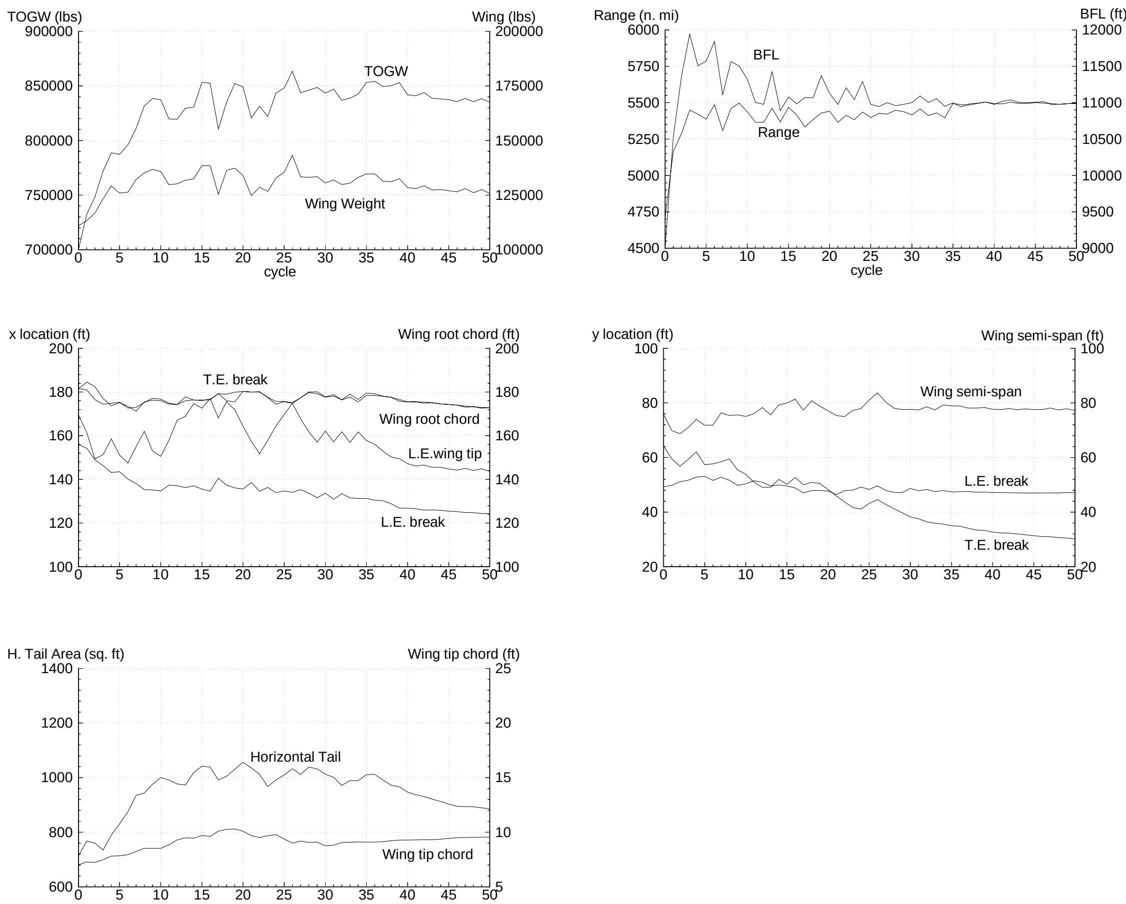

Figure 31. Design history for Case B.

Table 13. Results for Case B.

Weight Data	
Gross weight, *lbs*	835137
Wing weight, *lbs*	125782
Fuel weight, *lbs*	436912
Fuel/Gross	0.52
Planform Geometry	
Root chord, *ft*	172.9
Tip chord, *ft*	9.5
Wing area, *sq ft*	14030
Wing span, *ft*	166.5
Aspect ratio	2.0
Horizontal tail area, *sq ft*	1771
Vertical tail area, *sq ft*	896
LE sweep, inboard	69.2¡
LE sweep, outboard	32.8¡
TE sweep, outboard	-22.7¡
Performance Data	
Range, *n. mi.*	5495
Balanced field length, *ft*	10983
Max thrust/engine, *lbs*	55267
Landing angle-of-attack	10.6¡
$(L/D)_{max}$	9.1

The effect of pitch-up was again studied by calculating the balanced field length, time-to-rotate during takeoff, and the approach trim deflection constraints with and without the pitch-up behavior. Table 14 lists the values of each constraint using the linear and nonlinear pitching moment models. As listed in Table 14, the takeoff constraints do not change significantly. This is due to the small differences in the pitching moment up to the takeoff attitude of 8.6 degrees as shown in Figure 32. The differences in approach trim deflection are due to the various pitching moment values at the approach angle-of-attack as presented in Figure 33. The nose-down control margin was also satisfied as shown in Figure 34.

Table 14. Pitch-up Comparison (Case B).

	BFL (ft)	Time to Rotate (sec)	Approach Trim (deg)
$C_{M\alpha}$ (original design code)	10994	5.0	9.7
$C_{M\alpha}$ (*Aero2s* + APE)	11017	5.1	4.5
Pitch-up - $C_{M\alpha 1}$, α_B, $C_{M\alpha 2}$ (*Aero2s* + APE)	11017	5.1	5.3

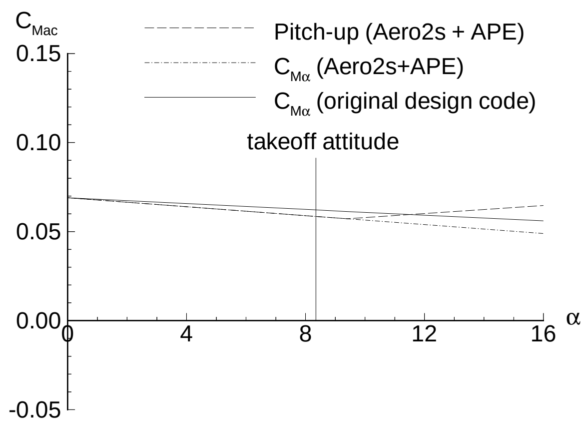

Figure 32. Takeoff pitching moment (Case B).

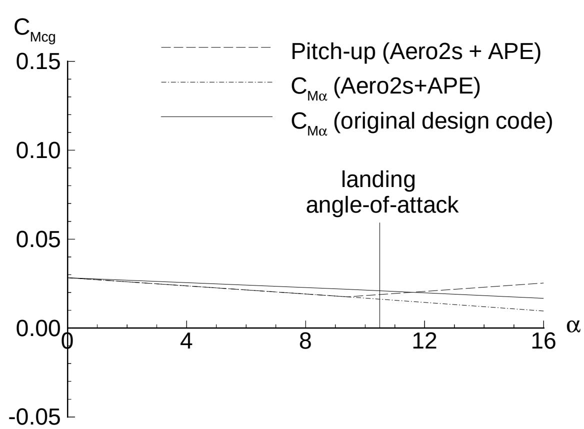

Figure 33. Landing pitching moment (Case B).

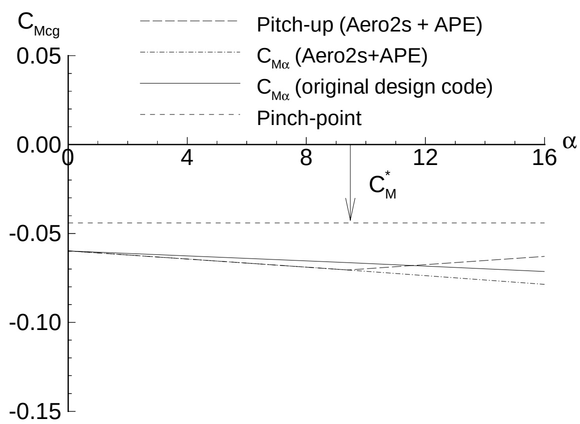

Figure 34. Nose-down pitching moment (Case B).

8.3 Case C

This optimization included the response surface models for the pitch-up: the pitching moment slope before pitch-up ($C_{M\alpha,1}$), pitch-up angle-of-attack (α_B), and slope after pitch-up ($C_{M\alpha,2}$). As in the optimization of Case B, the constraints were increased from 69 to 111, the increment in pitching moment due to tail deflection ($\Delta C_{M\delta e}$) was calculated by JKayVLM, and the increment in lift and pitching moment due to flap deflection ($\Delta C_{L\delta f}$, $\Delta C_{M\delta f}$) were held constant. The same initial design is used in this optimization. After 45 optimization cycles, the TOGW increased to 860,100 *lbs* with all the constraints satisfied. A convergence history of the TOGW, range, balanced field length, planform design variables, and horizontal tail area are shown in Figure 35. Table 15 lists the weight data, planform geometry characteristics, and performance data on the optimal design.

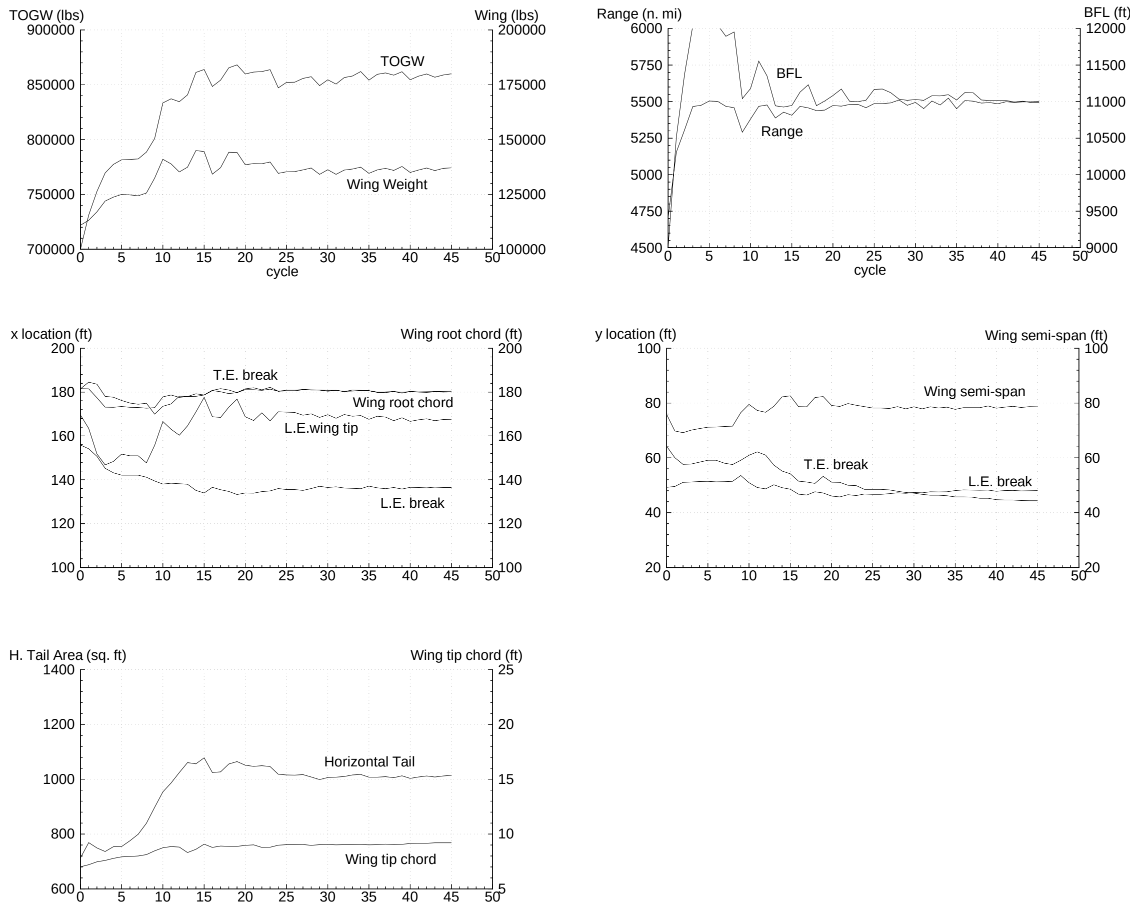

Figure 35. Design history for Case C.

Table 15. Results for Case C.

Weight Data	
Gross weight, *lbs*	860073
Wing weight, *lbs*	137114
Fuel weight, *lbs*	446361
Fuel/Gross	0.52
Planform Geometry	
Root chord, *ft*	180.1
Tip chord, *ft*	9.2
Wing area, *sq ft*	14650
Wing span, *ft*	169.2
Aspect ratio	2.0
Horizontal tail area, *sq ft*	2029
Vertical tail area, *sq ft*	926
LE sweep, inboard	70.6¡
LE sweep, outboard	45.4¡
Performance Data	
Range, *n. mi.*	5502
Balanced field length, *ft*	10967
Max thrust/engine, *lbs*	55864
Landing angle-of-attack	10.5¡
$(L/D)_{max}$	9.3

This optimal design is the heaviest so far at a TOGW of 860,100 *lbs*. The driving constraints for this problem were also the engine-out stability constraint and the two thrust constraints. However, the trailing-edge is not swept forward as in the previous case. Since it has been shown by the prior two cases that pitch-up does not greatly effect the takeoff and approach trim constraints, this optimal design should be very similar to Case B. As shown in the convergence history, the wing trailing-edge break location does move inboard but the leading-edge wing tip does not move forward as in Case B. The resulting wing weight is 11,300 *lbs* heavier than the wing in Case B. In addition, the design also carries heavier engines and a larger vertical and horizontal tail to control the heavier aircraft. There are two possible explanations for the differences in the design. The first and simplest is that the design may be stuck in a local minimum. A more complex explanation may be that the trailing-edge is not swept forward because pitch-up has a greater affect on the takeoff and approach trim constraints than presumed in the two previous cases.

Figure 36 presents the pitch-up parameters during the design history of Case B and C. As shown in the figure, the designs during the optimization of Case B drive towards a very low pitch-up angle-of-attack (α_B) around 3 degrees, while the designs during the optimization of Case C all have pitch-up angles-of-attack around 7 degrees. Keep in mind that the optimization of Case B did not include pitch-up and ignored the pitch-up angle-of-attack information which may have affected the results. A lower pitch-up angle-of-attack could significantly change the approach trim deflection.

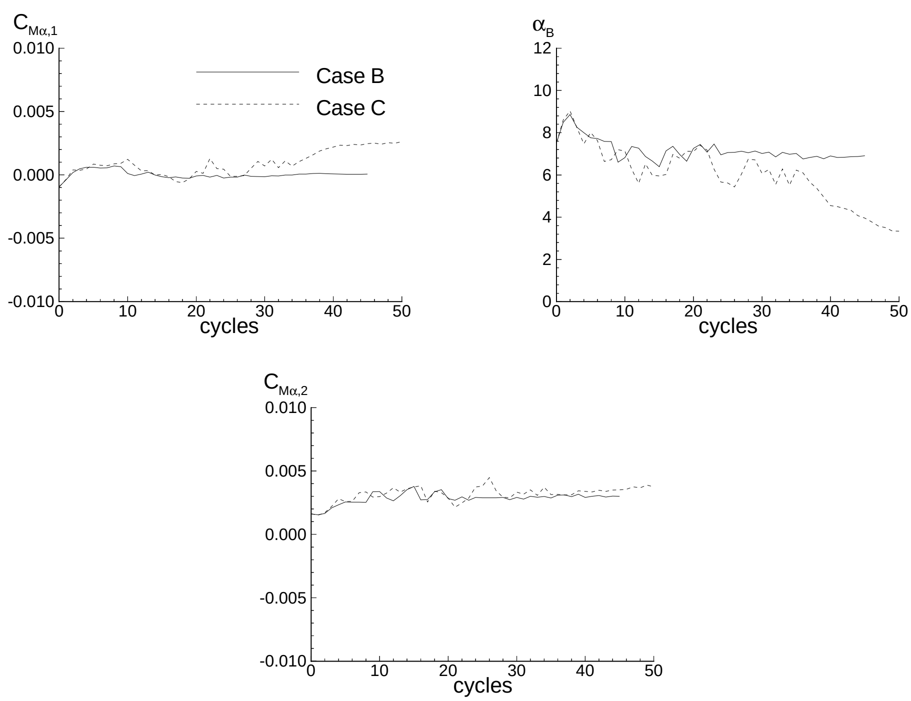

Figure 36. Response surface values throughout the optimization history of Case B and C.

The takeoff, landing, and nose-down pitching moment curves are provided in Figures 37 through 39. The takeoff and approach trim constraints were evaluated using the pitch-up parameters as provided by the response surface models and the actual values calculated by *Aero2s* and APE. The reason for this comparison is to show the impact of errors within the response surface models. As shown in Figures 37 through 39, the pitch-up angle-of-attack is underpredicted approximately 1.5 degrees by the response surface model. This does not greatly affect the balanced field length and time-to-rotate, but does slightly change the approach trim deflection. The nose-down control margin is still satisfied as shown in Figure 39.

Table 16. Actual vs. response surface results (Case C).

	BFL (*ft*)	Time to Rotate (*sec*)	Approach Trim (*deg*)
Pitch-up - $C_{M\alpha 1}$, α_B, $C_{M\alpha 2}$ (Response Surface Models)	10973	5.0	1.6
Pitch-up - $C_{M\alpha 1}$, α_B, $C_{M\alpha 2}$ (*Aero2s* + APE)	10978	5.0	0.7

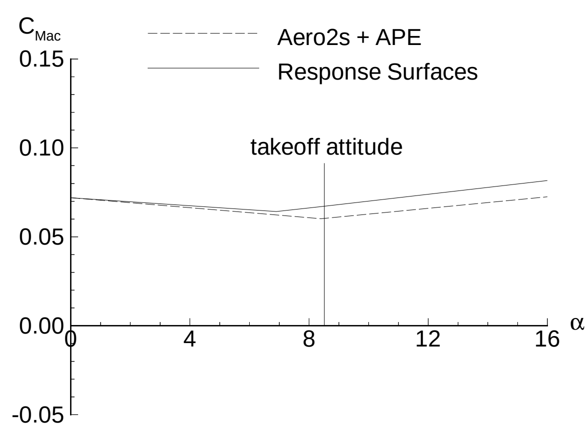

Figure 37. Takeoff pitching moment (Case C).

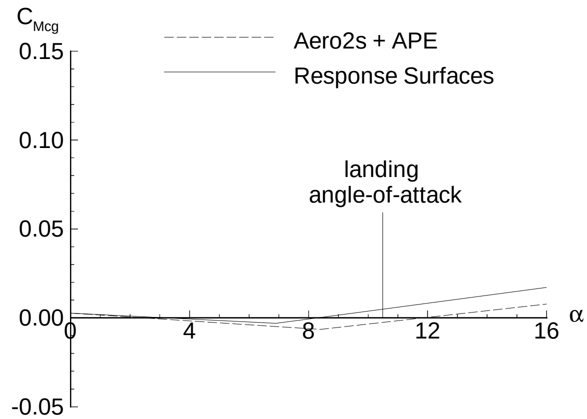

Figure 38. Landing pitching moment (Case C).

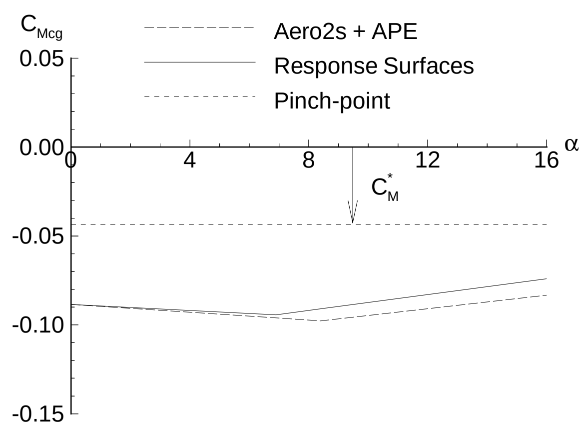

Figure 39. Nose-down pitching moment (Case C).

8.4 Case D

The final two optimizations included response surface models for the increment in pitching moment due to tail deflection ($\Delta C_{M\delta e}$) and the increment in lift and pitching moment due to flap deflections ($\Delta C_{L\delta f}$, $\Delta C_{M\delta f}$) which are not held constant in this optimization. The pitch-up response surface models ($C_{M\alpha,1}$, α_B, $C_{M\alpha,2}$) were also included. The same initial design is used in this optimization. After 38 optimization cycles, the TOGW increased to 790,100 *lbs* with all the constraints satisfied. A convergence history of the TOGW, range, balanced field length, planform design variables, and horizontal tail area are shown in Figure 40. Table 17 lists the weight data, planform geometry characteristics, and performance data on the optimal design.

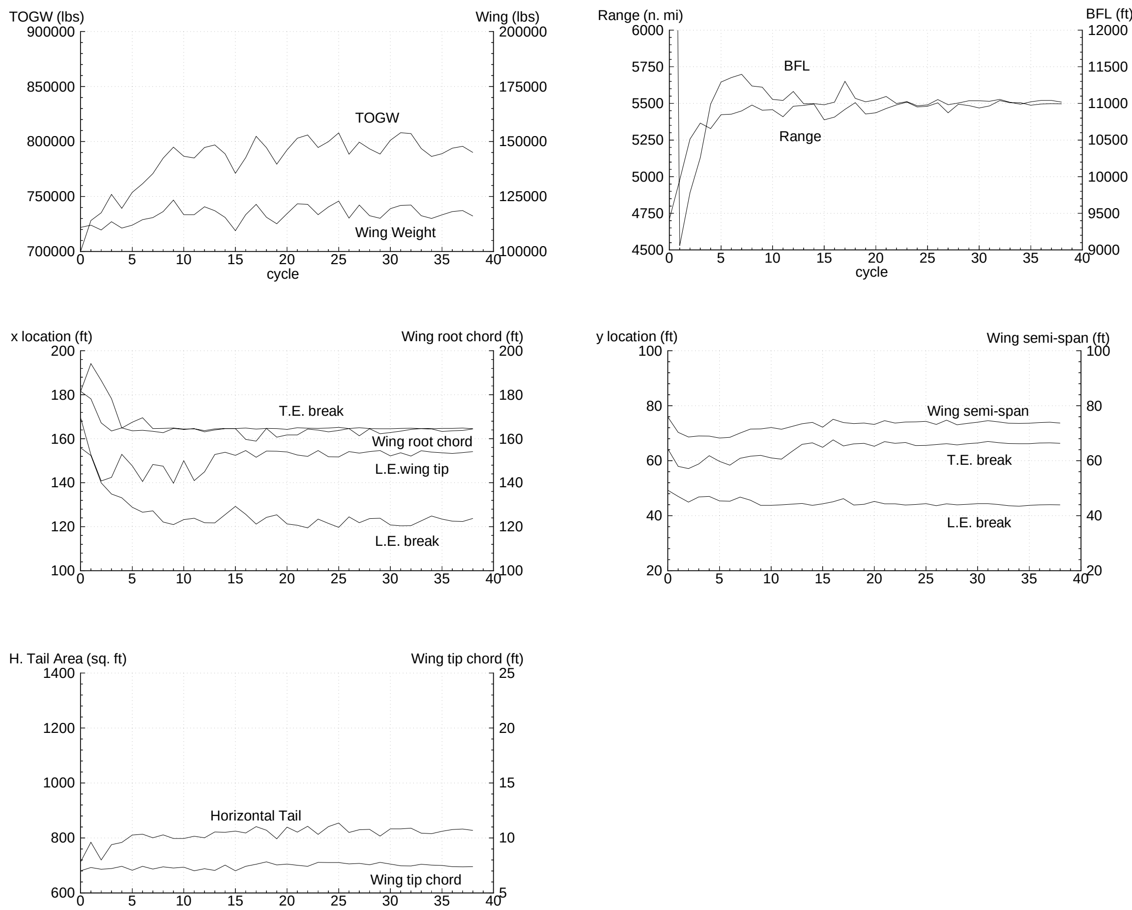

Figure 40. Design history for Case D.

Table 17. Results for Case D.

Weight Data	
Gross weight, *lbs*	790080
Wing weight, *lbs*	116099
Fuel weight, *lbs*	412067
Fuel/Gross	0.52
Planform Geometry	
Root chord, *ft*	164.5
Tip chord, *ft*	7.4
Wing area, *sq ft*	12593
Wing span, *ft*	159.3
Aspect ratio	2.0
Horizontal tail area, *sq ft*	1654
Vertical tail area, *sq ft*	843
LE sweep, inboard	70.5¡
LE sweep, outboard	45.7¡
Performance Data	
Range, *n. mi.*	5497
Balanced field length, *ft*	11005
Max thrust/engine, *lbs*	49258
Landing angle-of-attack	11.3¡
$(L/D)_{max}$	9.2

This optimal design is considerably smaller and lighter than the previous optimal designs. The final weight is close to 70,000 *lbs* lighter than the previous optimization. In addition, the wing planform, horizontal tail, and vertical tail sizes are 2060 ft^2, 380 ft^2 and 90 ft^2 smaller respectively. The reason for this lightweight design is the differences between the pitching moment values predicted by the response surface models and the values which would have been calculated by the original design code. As shown in Figure 41, the increment in lift due to flap deflection calculated by the response surface model is over twice the constant value set during the previous optimizations. In addition, the increment in pitching moment due to elevator deflection is calculated 0.02 greater than the value calculated by JKayVLM. The increment in pitching moment due to flap deflection is calculated as 0.013 less than the constant value set during the other optimizations. Therefore, for a given design, the balanced field length and time-to-rotate would be shorter using the response surface approximations. As a result, the design can be designed with a smaller wing planform and smaller control surfaces to achieve the same performance.

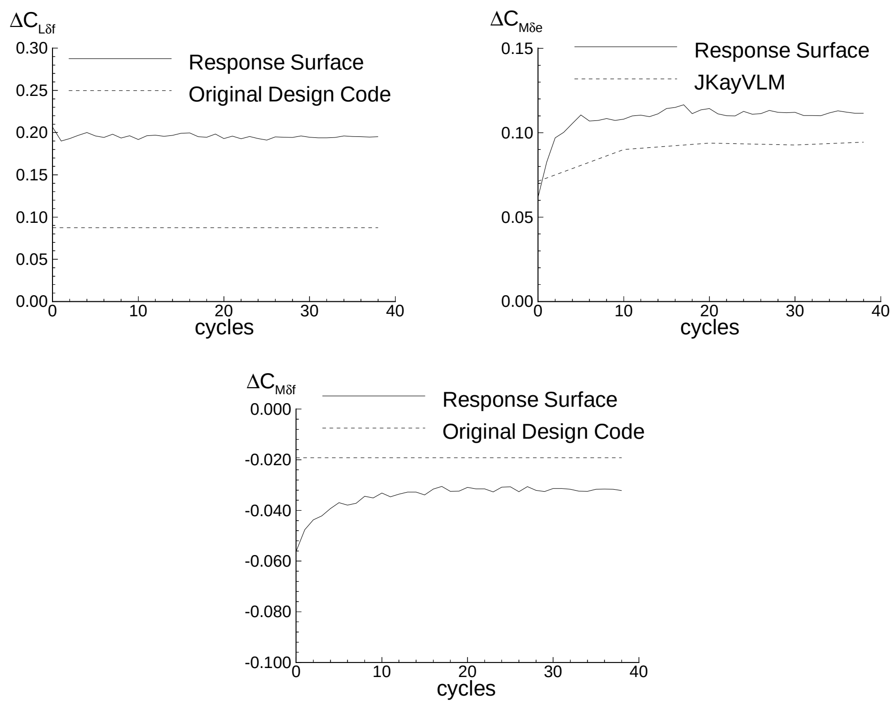

Figure 41. Response surface values vs. design code values.

The balanced field length, time-to-rotate, and approach trim deflection for this configuration are listed in Table 18. Using *Aero2s* and APE, the actual pitching moment was calculated and the constraints were recalculated. Using actual pitching moment data, the balance field length increased 320 *ft* and the time to rotate increased 1.2 *sec*, which now violate the constraints of 11,000 *ft* and 5.0 *sec* respectively. The takeoff pitching moment curve is shown in Figure 42 which shows that there is a significant difference between the pitching moment as calculated by the response surface models and the actual pitching moment curve. The approach trim deflection decreased but is not critical. The landing pitching moment curve is shown in Figure 43. The nose-down control margin is still satisfied as shown in Figure 44.

Table 18. Actual vs. response surface results (Case D).

	BFL (*ft*)	Time to Rotate (*sec*)	Approach Trim (*deg*)
$C_{M\alpha,1}$, α_B, $C_{M\alpha,2}$, $\Delta C_{M\delta e}$, $\Delta C_{L\delta f}$, $\Delta C_{M\delta f}$ (Response Surfaces)	10989	5.0	3.5
$C_{M\alpha,1}$, α_B, $C_{M\alpha,2}$, $\Delta C_{M\delta e}$, $\Delta C_{L\delta f}$, $\Delta C_{M\delta f}$ (*Aero2s* + APE)	11320	6.2	2.3

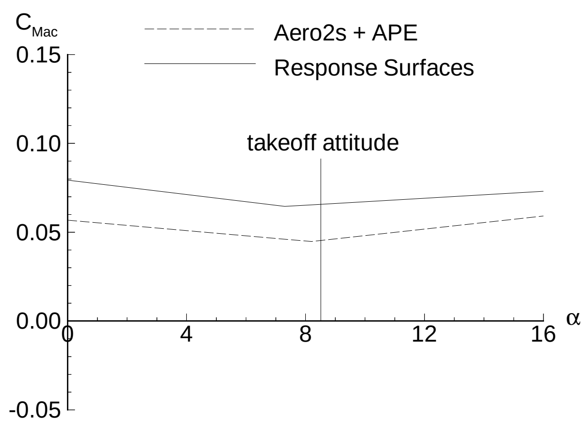

Figure 42. Takeoff pitching moment (Case D).

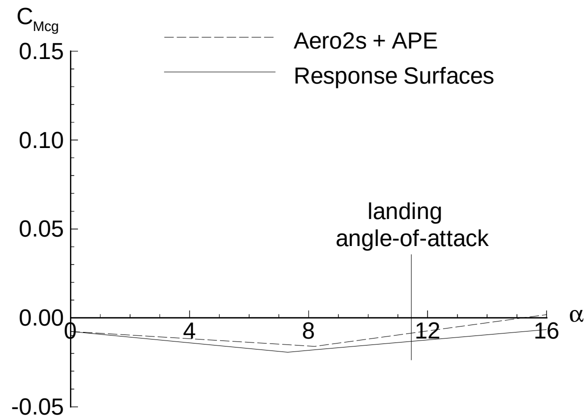

Figure 43. Landing pitching moment (Case D).

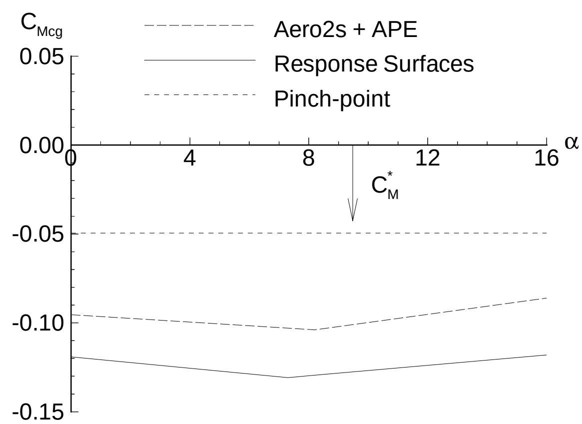

Figure 44. Nose-down pitching moment (Case D).

The accuracy of the response surface approximations throughout the optimization was investigated and presented in Figure 45. This figure compares the response surface values for each parameter to the actual values calculated by *Aero2s* and the APE method throughout the history of the optimization. As presented, the parameters calculated by the response surface were relatively accurate near the beginning of the optimization and increased in error as the optimization progressed. This trend was expected since a quadratic polynomial response surface was generated around the initial design point and the error bounds increase as the design moves further away from the initial design. As shown in the figure, the final value of each parameter was predicted reasonably well using the response surface models, except for the pitching moment increment due to tail deflection ($\Delta C_{M\delta e}$) which was over-predicted approximately 28% of the actual value. This would explain the large increase in balance field length and time-to-rotate as shown in Table 18. The optimizer believed it had more control power from the horizontal tail than it actually did.

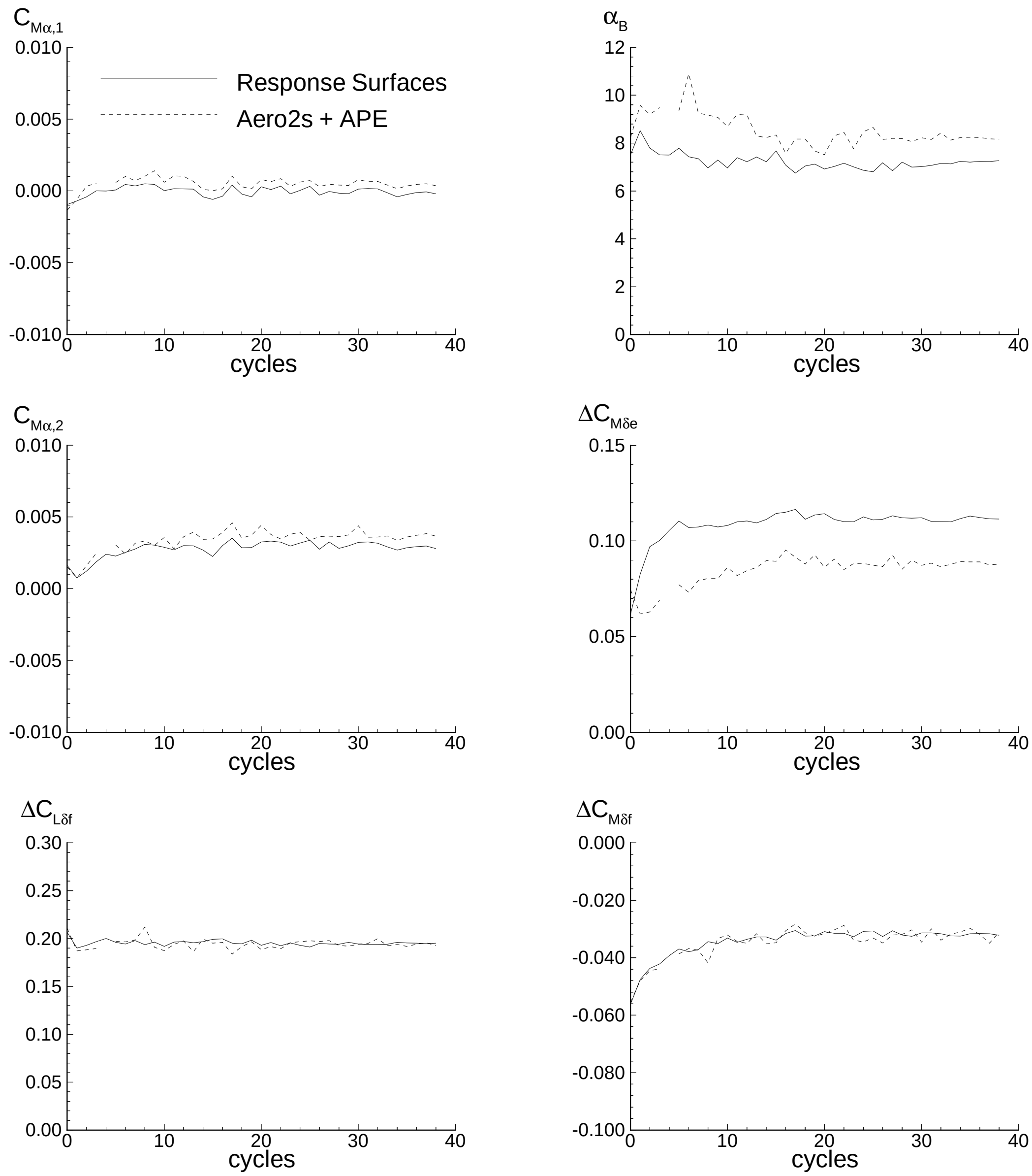

Figure 45. Response surface values vs. actual response (Case D).

Tables 19 and 20 list the predicted variance of each parameter for two separate designs, the initial and final optimal design. Listed in each table are the values of each parameter calculated by the response surface model, the actual value calculated by *Aero2s* and APE, the predicted variance (± error about the predicted value), and the actual difference or error. Since the unknown response of each parameter can not be exactly captured by a quadratic model, there will be an error between the approximation and the true response. As shown in Tables 19 and 20, the actual error is on the order of magnitude or less than the predicted variance which means that there is little bias in the models. In other words, the quadratic model used to generate the response surface models capture most of the response over a linear model, cubic model, or some other function.

Table 19. Predicted variance of the response surface models evaluated at the initial design.

Response Surface	Predicted Value	Actual Value	Predicted Variance	Actual Difference
$C_{M_{\alpha,1}}$	-0.000975	-0.001352	±0.000128	-0.000395
α_B	7.509844	8.234352	±0.615302	0.724508
$C_{M_{\alpha,2}}$	0.001625	0.001519	±0.000219	-0.000106
$\breve{C}_{M_{\delta e}}$	0.061679	0.074510	±0.006325	0.012831
$\breve{C}_{L_{\delta f}}$	0.206570	0.210843	±0.004899	0.004273
$\breve{C}_{M_{\delta f}}$	-0.056198	-0.055599	±0.002000	0.000599

Table 20. Predicted variance of the response surface models evaluated at the final design.

Response Surface	Predicted Value	Actual Value	Predicted Variance	Actual Difference
$C_{M_{\alpha,1}}$	-0.000209	0.000361	±0.000387	0.000570
α_B	7.270312	8.163628	±1.859823	0.893316
$C_{M_{\alpha,2}}$	0.002796	0.003649	±0.000663	0.000853
$\breve{C}_{M_{\delta e}}$	0.111502	0.087871	±0.019287	-0.023631
$\breve{C}_{L_{\delta f}}$	0.195210	0.192453	±0.015232	-0.002757
$\breve{C}_{M_{\delta f}}$	-0.032177	-0.031045	±0.006928	0.001132

8.5 Case E

To investigate the possibility of improving the predicted response of the response surface models, a factorial design of experiment was generated over a smaller design space surrounding a design point of interest instead of approximating the response surface over the entire feasible design space. The design point of interest was chosen as the optimal configuration of Case D and the design variables were allowed to vary as specified in Table 21.

Table 21. Factorial design limits**.**

Design Variable	Baseline Value	Variation	
x_1	164.5	-10%	+10%
x_2	123.7	-10%	+10%
x_3	43.9	-10%	+10%
x_4	164.5	-10%	+10%
x_5	66.3	-10%	+10%
x_6	154.2	-10%	+10%
x_7	7.4	-0%	+50%
x_8	73.7	-10%	+10%
x_9	827.4	-30%	+30%

Simple geometric constraints were used to screen out 12,150 infeasible geometric designs out of 19,683 three-level nine-variable factorial designs. In this case, the infeasible designs were thrown out instead of moving the designs towards the feasible geometric design space. New response surfaces were generated using 150 D-optimal points of the remaining feasible factorial designs and Table 22 lists their corresponding R-squared value. As shown in the table, the response surfaces predicted the true response very well except for the pitch-up angle-of-attack response surface model. The poor response in the pitch-up angle-of-attack is due to the fact that several of the D-optimal configurations exhibited a linear pitching moment curve throughout the entire angle-of-attack regime.

With our assumptions that pitch-up must occur, the specific angle-of-attack at which pitch-up occurred was not easily identified within the data and therefore there were large fluctuations in the prediction.

Table 22. Response surface fit over reduced design space for Case D.

	Pitch-up Response Surfaces			Tail & Flap Response Surfaces		
	$C_{M_{\alpha,1}}$	α_B	$C_{M_{\alpha,2}}$	$\breve{C}_{M\delta e}$	$\breve{C}_{L\delta f}$	$\breve{C}_{M\delta f}$
R-squared	0.992332	0.684075	0.929874	0.974253	0.954308	0.982648
Adjusted R-squared	0.987974	0.504497	0.890013	0.959619	0.928335	0.972784
Root mean square error	0.000165	1.300323	0.000461	0.006750	0.005666	0.002830
Mean of Response	0.001000	6.911615	0.003988	0.084034	0.193532	-0.03535
Observations	150	150	150	150	150	150

Using the improved response surfaces, the final optimal configuration (Case E) is shown in Figure 26. The final result has a similar wing planform as Case D. The takeoff gross weight decreased 15,700 *lbs*. The vertical tail decreased in size since the engines were allowed to move inboard. The horizontal tail size increased since the initial balanced field length was 11,350 *ft*. A convergence history of the TOGW, range, balanced field length, planform design variables, and horizontal tail area are shown in Figure 46. Table 23 lists the weight data, planform geometry characteristics, and performance data on the optimal design.

The balanced field length, time-to-rotate, and approach trim deflection for this configuration are listed in Table 24. Using *Aero2s* and APE, the actual pitching moment was calculated and the constraints were recalculated. Using actual pitching moment data, the balance field length increased 420 *ft* and the time to rotate increased 1.5 *sec*, which still violate the constraints of 11,000 *ft* and 5.0 *sec* respectively. The approach trim deflection increased and is still not critical. The pitching moment curves are shown in Figures 47 through 49.

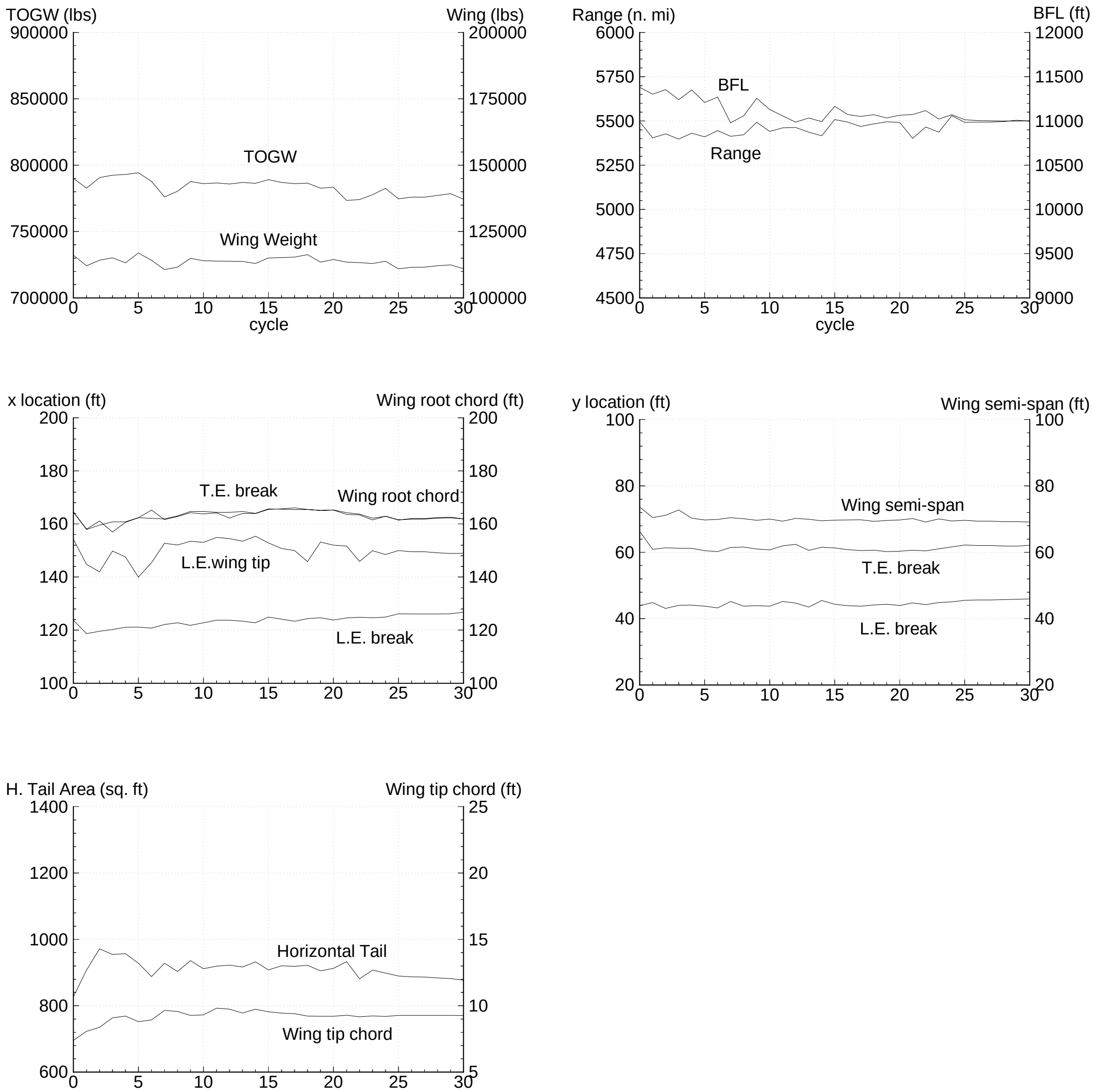

Figure 46. Design history for Case E.

Table 23. Results for Case E.

Weight Data	
Gross weight, *lbs*	774383
Wing weight, *lbs*	111003
Fuel weight, *lbs*	403240
Fuel/Gross	0.52
Planform Geometry	
Root chord, *ft*	161.9
Tip chord, *ft*	9.3
Wing area, *sq ft*	12192
Wing span, *ft*	150.2
Aspect ratio	1.9
Horizontal tail area, *sq ft*	1755
Vertical tail area, *sq ft*	693
LE sweep, inboard	70.1¡
LE sweep, outboard	43.7¡
Performance Data	
Range, *n. mi.*	5498
Balanced field length, *ft*	10989
Max thrust/engine, *lbs*	50233
Landing angle-of-attack	12.0¡
$(L/D)_{max}$	9.1

Table 24. Actual vs. response surface results (Case E).

	BFL (*ft*)	Time to Rotate (*sec*)	Approach Trim (*deg*)
$C_{M\alpha,1}$, α_B, $C_{M\alpha,2}$, $\Delta C_{M\partial e}$, $\Delta C_{L\delta f}$, $\Delta C_{M\delta f}$ (Response Surfaces)	10990	4.9	0.2
$C_{M\alpha,1}$, α_B, $C_{M\alpha,2}$, $\Delta C_{M\partial e}$, $\Delta C_{L\delta f}$, $\Delta C_{M\delta f}$ (*Aero2s* + APE)	11420	6.4	0.7

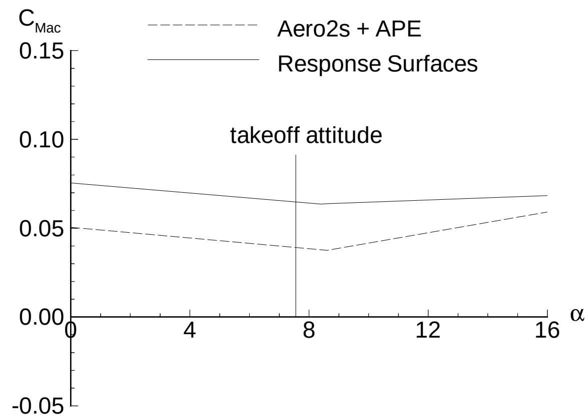

Figure 47. Takeoff pitching moment (Case E).

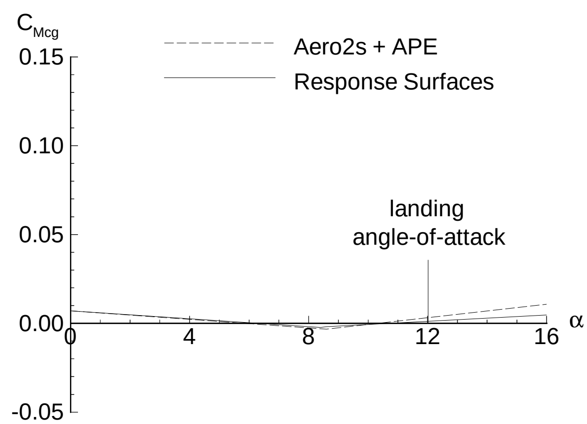

Figure 48. Landing pitching moment (Case E).

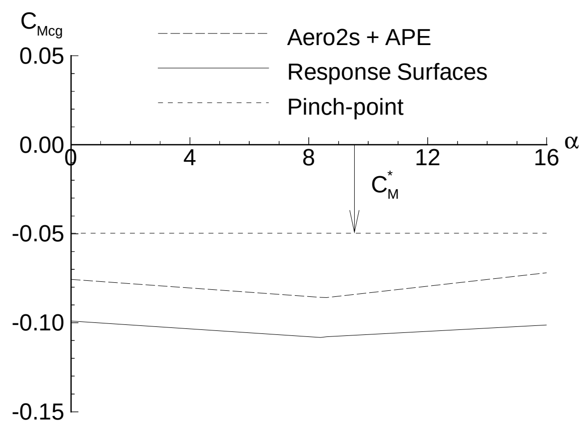

Figure 49. Nose down pitching moment (Case E).

As in the previous case, the accuracy of the response surface approximations throughout the optimization was investigated and is presented in Figure 50. In this case, each parameter was reasonably predicted by the response surface models, except for the pitch-up angle-of-attack (α_B) and the pitching moment due to tail deflection ($\Delta C_{M\delta e}$). The fluctuation in pitch-up angle-of-attack is due to the difficulty in calculating the angle-of-attack at which pitch-up occurs among near-linear data. The final value of $\Delta C_{M\delta e}$ was overpredicted by 24% and the result is the huge difference in balanced field length and time-to-rotate as presented in Table 24.

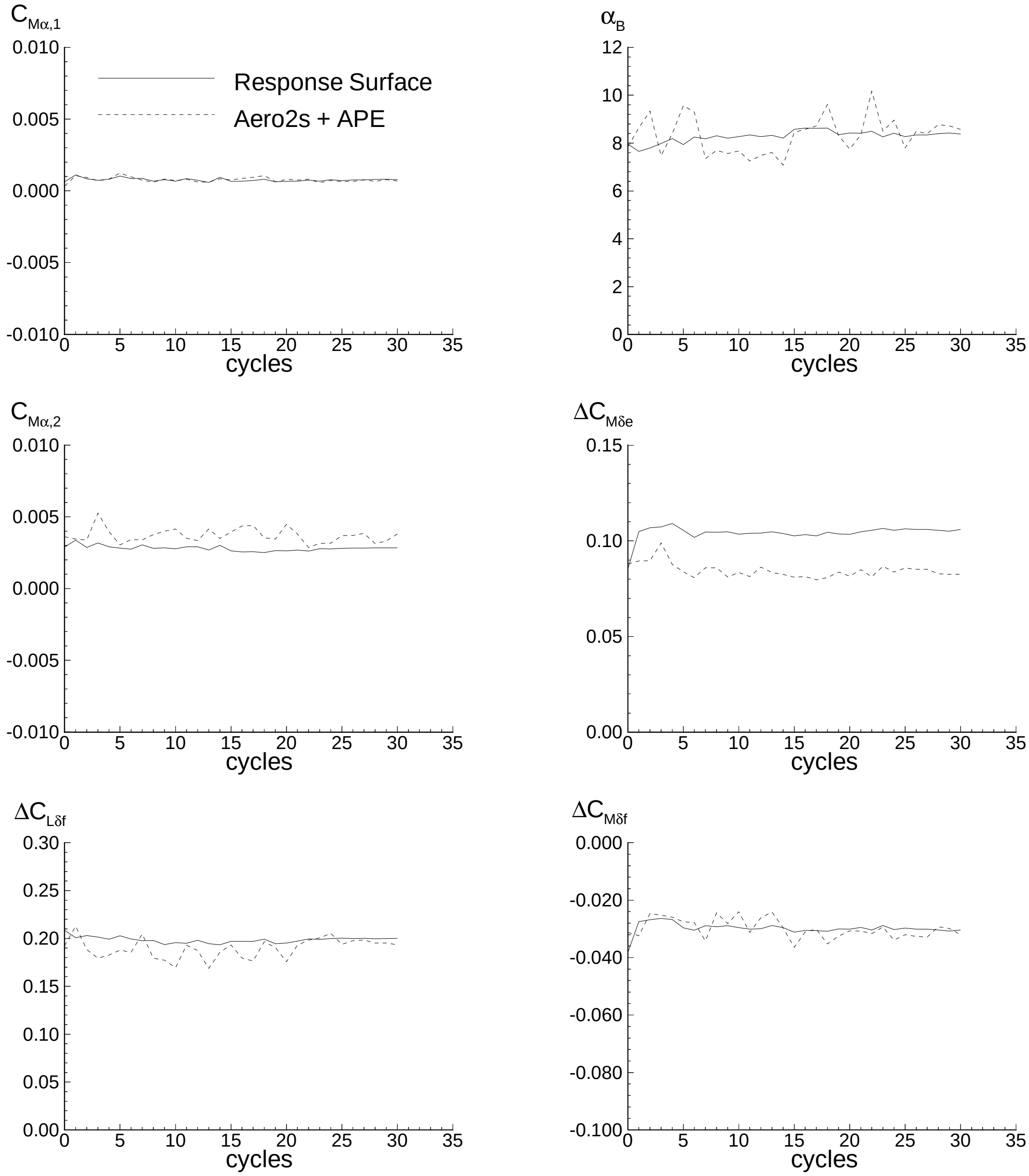

Figure 50. Response surface values vs. actual response (Case E).

Tables 25 and 26 list the predicted variance of each parameter for the initial and final optimal design. As shown in the tables, the actual error is still on the order of magnitude or less than the predicted variance which means that there is little bias in the models. In this case, the predicted variances of the final design are less than the variances of the initial design.

Table 25. Predicted variance of the response surface models evaluated at the initial design.

Response Surface	Predicted Value	Actual Value	Predicted Variance	Actual Difference
$C_{M_{\alpha 1}}$	0.000624	0.000322	±0.000209	-0.000302
α_B	7.959771	7.844286	±1.639030	-0.115485
$C_{M_{\alpha 2}}$	0.002901	0.003615	±0.000581	0.000714
$\breve{C}_{M\delta e}$	0.085455	0.087936	±0.008485	0.002481
$\breve{C}_{L\delta f}$	0.208536	0.192195	±0.007211	-0.016341
$\breve{C}_{M\delta f}$	-0.038147	-0.031205	±0.003464	0.006942

Table 26. Predicted variance of the response surface models evaluated at the final design.

Response Surface	Predicted Value	Actual Value	Predicted Variance	Actual Difference
$C_{M_{\alpha 1}}$	0.000784	0.000696	±0.000190	-0.000088
α_B	8.375019	8.570355	±1.493514	0.195336
$C_{M_{\alpha 2}}$	0.002835	0.003805	±0.000529	0.000970
$\breve{C}_{M\delta e}$	0.105921	0.082539	±0.007746	-0.023382
$\breve{C}_{L\delta f}$	0.200044	0.193509	±0.006633	-0.006535
$\breve{C}_{M\delta f}$	-0.030408	-0.032019	±0.003464	-0.001611

9. Conclusions

The objective of this project was to develop a procedure to incorporate nonlinear aerodynamics including pitch-up and to develop an improved model to estimate the lift and moment flap effects within the multidisciplinary design optimization of a high-speed civil transport and to study their effect on the design. A vortex lattice code, *Aero2s*, and the Aerodynamic Pitch-up Estimation (APE) method were used to develop a nonlinear pitching moment model including pitch-up and to model flap effects. Since an analysis by *Aero2s* and the APE method takes several minutes and many analyses are needed to incorporate the nonlinear pitching moment and flap effect models within the optimization, response surface methodology was used to approximate the results from *Aero2s* and the APE method by developing polynomial approximations through selected data collected prior to the optimization. Optimizations were completed with and without these polynomial approximations (or response surfaces). A summary of the optimizations is listed in Table 27.

Table 27. Summary of optimizations.

Case	Idea	TOGW (*lbs*)	Wing Area (ft^2)	Horizontal Tail Area (ft^2)	Vertical Tail Area (ft^2)
	Initial design	700,000	13,440	1,430	700
A	No response surfaces	834,200	14,440	2,040	960
B	Linear C_M response surface	835,140	14,030	1,770	900
C	Pitch-up response surfaces	860,070	14,650	2,030	930
D	All response surfaces	790,080	12,590	1,650	840
E	Reduced design space	774,380	12,190	1,770	690

Since the initial design did not satisfy all of the constraints due to recent modifications and improvements to the design code, the first optimization (Case A) was performed to obtain a baseline optimal design to compare the effects of the nonlinear pitching moment model and flap effectiveness model (via response surfaces) on the optimization. Since the range constraint was severely violated, more fuel and a larger aircraft was needed and the result was a substantial increase in the TOGW. In addition, the vertical tail size increased to satisfy the engine-out requirement and the horizontal tail increased to satisfy the takeoff requirements.

Case B was used to study the effects of using a response surface approximation for the pitching moment curve slope instead of calculating the slope using the VLM method within the design code. The optimal design of Case B was approximately 1,000 *lbs* heavier but needed to sweep the wing trailing-edge forward to satisfy the thrust constraints by designing a lighter wing instead of increasing the size and weight of the engines.

The nonlinear pitching moment model with pitch-up was included in Case C. The optimal design was 25,000 *lbs* heavier than Case B since the wing trailing-edge was not allowed to sweep forward. The wing was not designed with a forward-swept trailing-edge because the response surfaces predicted a very low pitch-up angle-of-attack for this type of design. Therefore, pitch-up did have an effect on the design. In addition, the design also carries heavier engines and a larger vertical and horizontal tail to control the heavier aircraft.

The response surfaces for the flap effectiveness model were included in Case D. The optimal design is considerably lighter than the previous optimizations. The reason for this lightweight design is the difference between the pitching moment and flap effectiveness predicted by the response surfaces and the value which would had been predicted by the original design code. The response surfaces predicted more lift and pitching moment for a given aircraft design. As a result, the aircraft was designed with a smaller wing planform and control surfaces to achieve the same performance.

In addition, the errors between the response surface models and the actual values from *Aero2s* and the APE method were examined for Case D. Since the increment in pitching moment due to horizontal tail deflection was in error (28%) at the optimal design, the takeoff constraints were violated using the actual analysis. As a result, new response surface models were generated within a smaller design space surrounding Case D, in hopes of decreasing the error of the response surfaces within this region of the design space.

The final optimization (Case E) was performed with these new response surfaces. The result was an optimal design similar to Case D but 16,000 *lbs* lighter. The vertical tail decreased in size since the engines were allowed to move inboard. The horizontal tail size increased since the initial balanced field length was violated by 320 *ft*. Again, the error of the response surfaces was examined and the takeoff constraints for this optimal design were still violated using the actual analysis.

In conclusion, this project demonstrated a way to incorporate nonlinear aerodynamics into the design optimization and did find that pitch-up had an effect on the design of the aircraft. Response surfaces were used to include pitch-up and flap effects into the optimization and were found to be a useful tool. However, errors within the response surface approximation can affect the final output of the optimization. Therefore, techniques should be developed to minimize the errors between the response surface approximation and the true response.

10. References

1. McCullers, L. A., Aircraft Configuration Optimization Including Optimized Flight Profiles, *Proceedings of a Symposium on Recent Experiences in Multidisciplinary Analysis and Optimization*, J. Sobieski, compiler, NASA CP-2327, Apr. 1984, pp. 395-412.

2. Jayaram, S., Myklebust, A., and Gelhausen, P., ACSYNT - A Standards-Based System for Parametric, Computer Aided Conceptual Design of Aircraft, AIAA Paper 92-1268, Feb. 1992.

3. Hutchison, M. G., Unger, E. R., Mason, W. H., Grossman, B., and Haftka, R. T., Variable-Complexity Aerodynamic Optimization of an HSCT Wing Using Structural Wing-Weight Equations, *Journal of Aircraft*, Vol. 31, No. 1, 1994, pp. 110 -116.

4. Dudley, J., Huang, X., Haftka, R. T., Grossman, B., and Mason, W. H., Variable-Complexity Interlacing of Weight Equation and Structural Optimization for the Design of the High Speed Civil Transport, AIAA Paper 94-4377, 1994.

5. Kaufman, M., Balabanov, V., Burgee, S., Giunta, A. A., Grossman, B., Mason, W. H., Watson, L. T., and Haftka, R. T., Variable-Complexity Response Surface Approximations for Wing Structural Weight in HSCT Design, 34th Aerospace Sciences Meeting and Exhibit, AIAA Paper 96-0089, Reno, NV, Jan. 1996.

6. Giunta, A. A., Narducci, R., Burgee, S., Grossman, B., Mason, W. H., Watson, L. T., and Haftka, R. T., Variable-Complexity Response Surface Aerodynamic Design of an HSCT Wing, Proceedings of the 13th AIAA Applied Aerodynamics Conference, AIAA Paper 95-1886, pp. 994-1002, San Diego, CA, June 19-22, 1995.

7. Benoliel, A. M. and Mason, W. H., Pitch-up Characteristics for HSCT Class Planforms: Survey and Estimation, AIAA 12th Applied Aerodynamics Conference, AIAA Paper 94-1819, Colorado Springs, CO, June 1994.

8. MacMillin, P. E., Trim, Control, and Performance Effects in Variable-Complexity High-Speed Civil Transport Design, Master s Thesis, Virginia Polytechnic Institute & State University, Blacksburg, VA, May 1996.

9. Grandhi, R. V., Thareja, R., and Haftka, R. T., NEWSUMT-A: A General Purpose Program for Constrained Optimization Using Approximations, *ASME J. Mechanisms, Transmissions and Automation in Design*, Vol. 107, 1985, pp. 94-99.

10. Diederich, F. W., A Planform Parameter for Correlating Certain Aerodynamic Characteristics of Swept Wings, NACA TN-2335, 1951.

11. Hutchison, M. G., *Multidisciplinary Optimization of High-Speed Civil Transport Configurations Using Variable-Complexity Modeling*. PhD Thesis, Virginia Polytechnic Institute & State University, Blacksburg, Virginia, Mar. 1993.

12. Hoak, D. E., *et al.*, *USAF Stability and Control DATCOM*. Flight Control Division, Air Force Flight Dynamics Laboratory, WPAFB, Ohio, 45433-00001, 1978. Revised.

13. Polhamus, E. C., Prediction of Vortex-Lift Characteristics by a Leading-Edge-Suction Analogy, *Journal of Aircraft*, vol. 8, pp. 193-199, 1971.

14. Kuchemann, D., *The Aerodynamic Design of Aircraft*. Pergamon Press, 1978.

15. Torenbeek, E., *Synthesis of Subsonic Airplane Design*. Delft University Press, 1982.

16. Kay, J., Mason, W. H., Durham, W., and Lutze, F., Control Authority Assessment in Aircraft Conceptual Design, AIAA Paper 93-3968, Aug. 1993.

17. Hutchison, M. G., Mason, W. H., Grossman, B., and Haftka, R. T., Aerodynamic Optimization of an HSCT Configuration Using Variable-Complexity Modeling, AIAA Paper 93-0101, Jan. 1993.

18. Carlson, H. W. and Miller, D. S., Numerical Methods for the Design and Analysis of Wings at Supersonic Speeds, NASA TN-D-7713, 1974.

19. Carlson H. W. and Mack, R. J., Estimation of Leading-Edge Thrust for Supersonic Wings of Arbitrary Planforms, NASA TP-1270, Oct. 1978.

20. Harris, Jr., R. V., An Analysis and Correlation of Aircraft Wave Drag, NASA TM-X-947, 1964.

21. Loftin, Laurence K., J., *Subsonic Aircraft: Evolution and the Matching of Size to Performance*. NASA Reference Publication 1060, Aug. 1980.

22. Powers, S. A., Critical Field Length Calculations for Preliminary Design, *Journal of Aircraft*, vol. 18, pp. 103-107, Feb. 1981.

23. Rutowski, E. S., Energy Approach to the General Aircraft Performance Problem, *Journal of Aeronuatical Science*, vol. 21, pp. 187-195, Mar. 1954.

24. Bryson, Jr., A. E., Desai, M. N., and Hoffman, W. C., Energy-State Approximation in Performance Optimization of Supersonic Aircraft, *Journal of Aircraft*, vol. 6, pp. 481-488, Nov.-Dec. 1969.

25. Vanderplaats, Minura and Associates, Inc., *GENESIS* User Manual, Version 1.3, Dec. 1993.

26. Antani, D. L. and Morgenstern, J. M., HSCT High-Lift Aerodynamic Technology Requirements, AIAA Paper 92-4228, Aug. 1992.

27. Baber, Jr., H. T., Characteristics of the Advanced Supersonic Technology AST-105-1 Configured for Transpacific Range with Pratt and Whitney Aircraft Variable Stream Control Engines, NASA TM-78818, March 1979.

28. Whitford, R., *Design for Air Combat*. Jane s Information Group, 1989, pp. 162-184.

29. Roskam, J., *Airplane Design Part II: Preliminary Configuration Design and Integration of the Propulsion System*. Kansas: Rosakm Aviation and Engineering Corporation, 1985, p. 205, 243.

30. Chai, S., Crisafulli, P., and Mason, W. H., Aircraft Center of Gravity Estimation in Conceptual/Preliminary Design, 1st AIAA Aircraft Engineering, Technology, and Operations Congress, Los Angeles, CA, Sept. 19-21, 1995.

31. Nguyen, L.T. and Foster, J.V., Development of a Preliminary High-Angle-of-Attack Nose-Down Pitch Control Requirement for High-Performance Aircraft, NASA TM-101684, Feb. 1990.

32. Ogburn, M. E., Foster, J. V., Pahle, J. W., Wilson, R. J., And Lackey, J. B., Status of the Validation of High-Angle-of-Attack Nose-Down Pitch Control Margin Design Guidelines, AIAA Paper 93-3623-CP, 1993.

33. Personal communication with Mr. Brook Norton and Mr. Norm Princen, Stability and Control Group, McDonnell Douglas Aircraft Co., 3855 N. Lakewood Boulevard, Long Beach, Califorinia, 90846-0003. July 7, 1995.

34. Personal communication with Mr. Martin Waszak, Mail Stop 489, 6 North Dryden Street, NASA Langley Research Center, Hampton, Virginia, 23681. Oct. 9, 1995.

35. Hofmann, L. G. and Clement, W. F., Vehicle Design Considerations for Active Control Application to Subsonic Transport Aircraft, NASA CR-2408, Aug. 1974.

36. Holloway, R. B., Burris, P. M., and Johannes, R. P., Aircraft Performance Benefits from Modern Control Technology, *Journal of Aircraft*, Vol. 7, No. 6, Nov.-Dec. 1970, pp. 550-553.

37. Lamar, J. E. and Alford Jr., W. J., Aerodynamic-Center Considerations of Wings and Wing-Body Combinations, NASA SP-124, Paper No. 6, 1966.

38. Hopkins, E. J., Hicks, R. M., and Carmichael, R. L., Effects of Planform Variations on the Aerodynamic Characterisics of Low-Aspect-Ratio Wings with Cranked Leading Edges, NASA SP-124, Paper No. 32, 1966.

39. Ray, E. J. and Taylor, R. T., Transonic Aerodynamic Characteristics of a Tailless Fixed-Wing Supersonic Transport Model, NASA-TM-X-1214, Apr. 1966.

40. Corlett, W. A. and Foster, G. V., Aerodynamic Characteristics of a Tailless Fixed-Wing Supersonic Transport Model at Mach Numbers From 1.80 to 2.86, NASA TM-X-992, Aug. 1964.

41. Rech, J. and Leyman, C. S., Concorde Aerodynamics and Associated Systems Development, British Aerospace-Aerospatiale, AIAA Professional Studies Series, 1980.

42. Wilde, M. G. and Cormery, G., The Aerodynamic Derivation of the Concorde Wing, 11th Anglo-American Aeronautical Conference, London, Sept. 8-12, 1969.

43. Shrout, B. L., *et al*, Aerodynamic Characteristics of a Supersonic Cruise Airplane Configuration at Mach Numbers of 2.30, 2.96, and 3.30, NASA TM-78792, Jan. 1979.

44. Coe, Jr., P. L. and Weston, R. P., Effects of Wing Leading-Edge Deflection on Low-Speed Aerodynamic Characteristics of a Low-Aspect-Ratio Highly Swept Arrow-Wing Configuration, NASA TP-1434, 1979.

45. Coe, Jr., P. L., Huffman, J. K., and Fenbert, J. W., Leading-Edge Deflection Optimization of a Highly Swept Arrow-Wing Configuration, NASA TP-1777, 1980.

46. Wright, B. R., F. Bruckman, and N.A. Radovich, Arrow Wings for Supersonic Cruise Aircraft, *Journal of Aircraft*, Vol. 15, No. 12, pp. 829-836, December 3, 1978.

47. Carlson, H. W., Darden, C. M., and Mann, M. J., Validation of a Computer Code for Analysis of Subsonic Aerodynamic Performance of Wings With Flaps in Combination With a Canard or Horizontal Tail and an Application to Optimization, NASA TP-2961, 1990.

48. Yip, Long P. and Lysle P. Parlett. Low-Speed Wind-Tunnel Tests of a 1/10-Scale Model of an Arrow-Wing Supersonic Cruise Configuration Designed for Cruise at Mach 2.2, NASA TM-80152, 1979.

49. Quinto, P. F. and John W. P., Flap Effectiveness on Subsonic Longitudinal Aerodynamic Characteristics of a Modified Arrow Wing, NASA TM-84582, 1983.

50. Myers, R. H. and Montgomery, D. C., *Response Surface Methodology: Process and Product Optimization Using Designed Experiments*, John Wiley & Sons, Inc., 1995.

51. Mason, R. L., Gunst, R. F., and Hess, J. L., *Statistical Design and Analysis of Experiments*, John Wiley & Sons, New York, N. Y., 1989, pp. 215-221.

52. Box, M. J. and Draper, N. R., Factorial Designs, the $|\mathbf{X}^T\mathbf{X}|$ Criterion, and Some Related Matters, *Technometrics*, Vol. 2, No. 4, Nov., 1960, pp. 455-475.

53. Giunta, A. A., Dudley, J. M., Narducci, R., Grossman, B., Haftka, R. T., Mason, W. H., and Watson, L. T., Noisy Aerodynamic Response and Smooth Approximations in HSCT Design, AIAA Paper 94-4376, 1994.

Appendix A: Response Surface Equation Coefficients

Table A-1. Response surface coefficients.

Coef f	Term	$Cm_{a,1}$	a_B	$Cm_{a,,2}$	ˇCm_e	ˇCl_f	ˇCm_f
c_0	intercept	-3.117E-01	2.580E-01	3.975E-01	3.182E-01	3.516E-01	-6.544E-02
c_1	x_1	1.605E-01	-1.499E-01	-5.835E-01	-7.446E-01	-1.509E-01	-1.654E-01
c_2	x_2	-1.222E+00	2.191E-01	-1.240E+00	-3.005E-01	-3.508E-01	2.877E-01
c_3	x_3	7.762E-01	-1.735E-01	6.760E-01	-1.063E-01	4.281E-01	-5.719E-01
c_4	x_4	-1.403E-01	1.300E+00	-6.544E-01	7.791E-01	3.083E-01	-1.949E-01
c_5	x_5	3.716E-01	-6.649E-01	-1.331E-01	-2.143E-02	-1.338E-01	1.850E-01
c_6	x_6	-5.114E-01	-3.896E-01	8.547E-01	8.050E-02	3.389E-02	-3.254E-02
c_7	x_7	-1.129E-01	3.313E-01	-7.569E-02	2.510E-01	2.765E-01	-2.031E-01
c_8	x_8	-5.183E-01	4.916E-01	1.231E-01	1.502E-01	-1.505E-02	2.203E-01
c_9	x_9	-3.602E-01	-2.011E-02	-3.996E-01	1.395E+00	-6.365E-01	1.122E+00
c_{11}	x_1*x_1	-9.800E-02	-9.874E-02	-7.770E-02	4.754E-01	-1.795E-01	2.955E-01
c_{12}	x_1*x_2	5.184E-02	-1.665E-01	5.875E-03	2.078E-01	2.557E-01	1.255E-02
c_{13}	x_1*x_3	-2.199E-01	3.593E-02	-9.925E-02	9.834E-02	-1.681E-01	1.738E-01
c_{14}	x_1*x_4	1.591E-02	2.565E-01	-8.866E-02	-1.835E-01	2.282E-03	-6.060E-02
c_{15}	x_1*x_5	-1.369E-02	3.047E-01	7.048E-02	-1.492E-02	-3.644E-02	-6.657E-02
c_{16}	x_1*x_6	-1.940E-01	-2.706E-02	-1.156E-01	-1.730E-01	7.868E-02	-8.546E-02
c_{17}	x_1*x_7	4.636E-02	-1.193E-01	-2.379E-02	-1.395E-01	-1.404E-01	1.140E-01
c_{18}	x_1*x_8	1.154E-01	-2.339E-01	-1.830E-01	4.504E-02	-3.213E-02	4.937E-02
c_{19}	x_1*x_9	5.151E-01	2.922E-02	4.933E-01	-1.231E+00	1.184E-01	-4.184E-01
c_{22}	x_2*x_2	4.615E-01	-3.374E-01	2.606E-01	9.225E-02	-5.813E-01	1.719E-01
c_{23}	x_2*x_3	-4.902E-02	9.570E-02	-2.363E-01	-1.831E-01	2.854E-01	-1.334E-01
c_{24}	x_2*x_4	-4.754E-01	5.786E-01	3.314E-01	-5.068E-01	5.426E-01	-4.600E-01
c_{25}	x_2*x_5	3.450E-02	-1.084E-01	4.283E-01	-1.159E-01	9.072E-01	-7.593E-01
c_{26}	x_2*x_6	9.560E-01	-6.016E-01	2.644E-01	-7.591E-02	-3.485E-01	2.554E-01
c_{27}	x_2*x_7	7.897E-02	5.831E-02	6.533E-02	-2.662E-01	-1.723E-01	1.724E-01
c_{28}	x_2*x_8	-1.598E-01	4.021E-02	-4.707E-01	-2.428E-01	-2.646E-01	5.260E-02
c_{29}	x_2*x_9	-4.996E-01	1.613E-01	-1.099E-01	-2.112E-02	4.823E-01	-5.380E-01
c_{33}	x_3*x_3	-9.383E-02	1.104E-01	-1.154E-01	2.367E-01	-7.631E-02	1.534E-01
c_{34}	x_3*x_4	-1.205E-01	1.328E-01	-2.570E-01	2.726E-01	-1.553E-01	8.847E-02
c_{35}	x_3*x_5	-8.278E-02	3.480E-02	-2.364E-01	5.781E-02	-5.034E-01	3.982E-01
c_{36}	x_3*x_6	-1.447E-01	-1.174E-01	-2.187E-04	5.024E-02	1.019E-01	4.828E-02
c_{37}	x_3*x_7	-7.206E-02	-4.530E-02	-4.907E-02	2.366E-01	1.583E-03	2.424E-02
c_{38}	x_3*x_8	-1.277E-01	-1.081E-01	2.623E-01	1.562E-01	7.652E-02	-7.460E-02
c_{39}	x_3*x_9	2.670E-01	-1.341E-01	3.625E-01	-3.321E-01	-1.667E-01	-2.370E-02
c_{44}	x_4*x_4	2.295E-01	1.604E-01	-5.373E-01	7.082E-01	-3.309E-01	4.545E-01
c_{45}	x_4*x_5	8.635E-02	-9.481E-01	5.710E-01	-3.020E-01	-1.431E-01	3.276E-01
c_{46}	x_4*x_6	-1.145E+00	-5.806E-01	5.850E-01	-1.011E-01	4.072E-01	-3.359E-01
c_{47}	x_4*x_7	-1.335E-01	3.691E-01	-2.185E-01	3.343E-01	2.348E-01	-1.019E-01
c_{48}	x_4*x_8	-1.233E-01	5.027E-01	-5.388E-01	5.051E-01	1.025E-01	1.032E-01
c_{49}	x_4*x_9	-1.383E-01	-1.660E-01	-6.040E-02	6.755E-01	-3.179E-01	4.361E-01
c_{55}	x_5*x_5	-4.785E-02	2.959E-02	-2.261E-02	2.168E-01	6.111E-01	-3.081E-01
c_{56}	x_5*x_6	8.876E-01	-5.450E-01	-7.679E-01	2.712E-01	-5.676E-01	4.855E-02
c_{57}	x_5*x_7	-4.040E-02	-2.002E-02	-2.751E-02	8.039E-02	3.653E-03	1.386E-02

Coef f	Term	$Cm_{a,1}$	a_B	$Cm_{a,,2}$	$\breve{C}m_e$	$\breve{C}l_f$	$\breve{C}m_f$
c_{58}	x_5*x_8	-4.180E-02	2.344E-02	-5.098E-02	-1.239E-01	-3.424E-03	2.309E-02
c_{59}	x_5*x_9	-1.244E-02	1.527E-02	-1.002E-02	1.439E-02	1.041E-03	3.345E-02
c_{66}	x_6*x_6	6.124E-01	-6.094E-02	-2.213E-01	2.347E-01	-2.532E-01	1.619E-01
c_{67}	x_6*x_7	-4.502E-02	1.070E-01	-5.232E-02	5.665E-02	6.165E-02	-3.892E-02
c_{68}	x_6*x_8	-2.017E-01	4.975E-01	4.629E-01	-4.611E-02	3.106E-01	-2.240E-01
c_{69}	x_6*x_9	-3.680E-02	1.208E-01	-1.204E-01	-1.293E-01	1.810E-01	-9.889E-02
c_{77}	x_7*x_7	-1.523E-03	6.784E-02	-2.935E-02	-2.038E-02	8.326E-02	-8.056E-02
c_{78}	x_7*x_8	-8.045E-03	6.626E-02	-1.236E-02	5.166E-02	-4.535E-03	-8.411E-03
c_{79}	x_7*x_9	1.873E-02	-5.194E-03	2.521E-02	-1.154E-01	4.578E-02	-6.879E-02
c_{88}	x_8*x_8	4.242E-02	7.391E-02	1.168E-01	-6.155E-02	-1.954E-01	1.363E-01
c_{89}	x_8*x_9	8.968E-02	-2.804E-02	3.494E-01	-6.464E-01	-3.219E-01	2.246E-01
c_{99}	x_9*x_9	-7.581E-03	4.807E-02	4.650E-02	-2.685E-01	1.904E-01	-2.3623E-01

Where x_1 through x_9 are scaled to span from -1.0 to 1.0 using the following formulas:

$x_1 =$ (x_1 - 1.482e+00) / 3.293e-01 * 2.0 - 1.0
$x_2 =$ (x_2 - 1.163e+00) / 2.585e-01 * 2.0 - 1.0
$x_3 =$ (x_3 - 3.799e+00) / 8.442e-01 * 2.0 - 1.0
$x_4 =$ (x_4 - 1.482e+00) / 3.294e-01 * 2.0 - 1.0
$x_5 =$ (x_5 - 5.555e+00) / 1.234e+00 * 2.0 - 1.0
$x_6 =$ (x_6 - 1.369e+00) / 3.042e-01 * 2.0 - 1.0
$x_7 =$ (x_7 - 7.085e-01) / 3.542e-01 * 2.0 - 1.0
$x_8 =$ (x_8 - 6.195e+00) / 1.377e+00 * 2.0 - 1.0
$x_9 =$ (x_9 - 5.437e+00) / 4.660e+00 * 2.0 - 1.0

Table A-2. Reduced design space response surface coefficients.

Coef f	Term	$Cm_{a,1}$	a_B	$Cm_{a,,2}$	˘Cm_e	˘Cl_f	˘Cm_f
c_0	intercept	-5.144E-02	-2.538E-01	-4.443E-01	-2.607E-01	3.116E-01	-2.869E-01
c_1	x_1	4.979E-03	8.496E-02	-2.634E-01	-1.584E-01	-1.152E-02	-1.795E-01
c_2	x_2	-2.925E-01	4.738E-02	-3.209E-01	9.461E-02	7.167E-02	4.341E-02
c_3	x_3	1.747E-01	-9.052E-03	1.226E-01	-7.600E-02	8.414E-02	-1.215E-01
c_4	x_4	1.321E-01	1.134E-01	1.113E-01	-1.500E-01	5.185E-02	-1.782E-01
c_5	x_5	4.318E-02	1.378E-02	1.008E-02	-3.034E-02	1.699E-01	-9.046E-02
c_6	x_6	-9.751E-02	-1.604E-01	8.734E-02	2.304E-03	-2.475E-01	7.324E-02
c_7	x_7	3.040E-03	6.570E-02	2.180E-03	4.349E-03	3.384E-02	-6.516E-03
c_8	x_8	-1.345E-01	-4.481E-02	1.978E-02	-5.949E-02	6.507E-02	1.546E-02
c_9	x_9	-8.762E-02	-2.319E-02	-1.123E-01	3.558E-01	-2.423E-01	3.642E-01
c_{11}	x_1*x_1	1.322E-03	-4.538E-02	2.422E-02	7.601E-02	-4.550E-02	7.892E-02
c_{12}	x_1*x_2	4.985E-02	3.638E-02	-2.220E-02	-3.745E-02	-4.756E-04	-1.465E-03
c_{13}	x_1*x_3	-2.544E-02	-7.666E-04	9.808E-03	9.356E-03	-1.046E-03	1.021E-02
c_{14}	x_1*x_4	-3.037E-02	-4.025E-03	-1.314E-03	-4.539E-02	-5.041E-02	-5.737E-03
c_{15}	x_1*x_5	8.053E-03	-1.925E-03	-1.928E-03	-3.731E-03	-1.699E-02	-3.048E-02
c_{16}	x_1*x_6	2.127E-02	1.960E-02	-4.784E-02	-1.068E-02	6.382E-03	8.486E-04
c_{17}	x_1*x_7	-3.368E-03	4.675E-02	-1.662E-02	4.357E-03	1.525E-02	-5.454E-04
c_{18}	x_1*x_8	-8.426E-03	-4.738E-02	-2.813E-02	6.003E-03	-4.994E-03	9.357E-03
c_{19}	x_1*x_9	4.489E-02	-1.734E-02	4.044E-02	-6.714E-02	-2.778E-02	2.683E-03
c_{22}	x_2*x_2	-1.834E-02	-3.029E-02	6.450E-02	-2.032E-02	-1.349E-02	-4.257E-02
c_{23}	x_2*x_3	2.444E-02	-6.917E-03	1.265E-02	-9.387E-03	-5.686E-03	1.686E-03
c_{24}	x_2*x_4	-5.716E-03	1.015E-01	5.800E-02	2.824E-03	1.005E-01	-1.657E-02
c_{25}	x_2*x_5	3.791E-03	2.225E-02	-2.340E-02	-3.178E-03	6.323E-02	-1.903E-02
c_{26}	x_2*x_6	-5.265E-03	-5.023E-02	1.913E-02	-5.819E-03	5.733E-03	-4.225E-03
c_{27}	x_2*x_7	2.959E-03	3.611E-02	-1.067E-02	-1.006E-02	2.794E-02	-7.157E-03
c_{28}	x_2*x_8	-2.850E-02	-5.325E-02	1.654E-02	-1.748E-02	-5.221E-02	7.096E-03
c_{29}	x_2*x_9	-1.812E-02	2.642E-03	-2.963E-02	3.396E-02	-1.049E-02	2.401E-02
c_{33}	x_3*x_3	8.484E-05	-3.344E-03	8.408E-02	-2.555E-02	-1.407E-01	6.462E-02
c_{34}	x_3*x_4	-3.079E-02	-2.734E-03	-2.486E-02	1.432E-02	-3.172E-02	1.060E-03
c_{35}	x_3*x_5	-2.219E-03	-3.943E-03	-1.600E-02	-3.197E-03	4.232E-03	-1.160E-03
c_{36}	x_3*x_6	4.306E-02	-2.006E-02	8.839E-03	-2.907E-03	1.347E-02	2.855E-03
c_{37}	x_3*x_7	-5.293E-03	-5.742E-03	-2.841E-02	8.881E-03	4.740E-03	6.446E-03
c_{38}	x_3*x_8	-2.055E-02	6.341E-03	-3.889E-02	1.282E-03	2.901E-02	-3.355E-03
c_{39}	x_3*x_9	1.882E-02	2.841E-02	1.736E-02	-2.646E-02	1.960E-02	-2.254E-02
c_{44}	x_4*x_4	4.830E-02	-1.099E-01	-2.307E-02	1.479E-02	-8.048E-02	4.047E-02
c_{45}	x_4*x_5	1.357E-02	-1.906E-02	6.454E-02	5.122E-03	-1.743E-02	4.116E-02
c_{46}	x_4*x_6	-1.295E-01	1.369E-01	5.653E-02	1.707E-02	5.972E-02	-1.573E-02
c_{47}	x_4*x_7	5.859E-03	1.853E-02	-6.109E-03	-1.379E-02	-2.248E-02	1.151E-02
c_{48}	x_4*x_8	2.521E-02	1.473E-02	-3.665E-02	7.530E-04	7.067E-02	-1.027E-02
c_{49}	x_4*x_9	-1.047E-02	-1.002E-02	2.748E-03	-3.500E-02	4.855E-02	-8.541E-02
c_{55}	x_5*x_5	1.435E-02	2.867E-02	-1.422E-02	-1.204E-02	2.185E-02	-2.048E-02
c_{56}	x_5*x_6	-2.691E-02	1.400E-02	-2.680E-02	3.942E-03	-5.325E-02	9.432E-03
c_{57}	x_5*x_7	2.936E-03	-2.181E-03	-1.688E-02	3.304E-04	-5.819E-03	1.116E-02
c_{58}	x_5*x_8	-4.022E-02	-6.591E-02	-2.463E-02	2.547E-02	-5.237E-02	4.268E-02
c_{59}	x_5*x_9	3.821E-04	-1.221E-02	7.403E-03	2.578E-03	-9.852E-03	1.187E-03
c_{66}	x_6*x_6	5.257E-02	-1.765E-01	6.254E-02	-2.504E-02	-1.743E-02	-8.646E-03
c_{67}	x_6*x_7	1.685E-03	-4.615E-02	2.715E-03	1.115E-03	8.568E-03	-2.764E-03

Coef f	Term	$Cm_{a,1}$	a_B	$Cm_{a,,2}$	$\check{C}m_e$	$\check{C}l_f$	$\check{C}m_f$
c_{68}	x_6*x_8	-2.501E-02	4.369E-02	1.678E-02	2.471E-03	2.512E-02	-5.963E-03
c_{69}	x_6*x_9	4.658E-03	2.604E-02	9.217E-03	1.852E-03	-1.755E-02	8.953E-03
c_{77}	x_7*x_7	4.871E-03	3.155E-02	4.348E-03	-3.522E-02	-2.578E-02	-7.327E-03
c_{78}	x_7*x_8	-4.406E-03	-5.401E-02	3.335E-02	-1.063E-03	-6.551E-03	-2.209E-03
c_{79}	x_7*x_9	5.348E-03	8.039E-03	-8.813E-03	-5.932E-03	-9.975E-04	-4.390E-03
c_{88}	x_8*x_8	-1.763E-02	-1.198E-02	6.390E-02	2.044E-01	-2.457E-01	1.775E-01
c_{89}	x_8*x_9	-9.590E-03	2.107E-02	-1.319E-02	6.514E-03	1.523E-02	-8.962E-03
c_{99}	x_9*x_9	4.663E-02	7.354E-02	-8.627E-03	-1.779E-01	1.407E-01	-1.854E-01

Where x_1 through x_9 are scaled to span from -1.0 to 1.0 using the following formulas:

$x_1 = (x_1 - 1.482e+00) / 3.293e-01 * 2.0 - 1.0$

$x_2 = (x_2 - 1.163e+00) / 2.585e-01 * 2.0 - 1.0$

$x_3 = (x_3 - 3.799e+00) / 8.442e-01 * 2.0 - 1.0$

$x_4 = (x_4 - 1.482e+00) / 3.294e-01 * 2.0 - 1.0$

$x_5 = (x_5 - 5.555e+00) / 1.234e+00 * 2.0 - 1.0$

$x_6 = (x_6 - 1.369e+00) / 3.042e-01 * 2.0 - 1.0$

$x_7 = (x_7 - 7.085e-01) / 3.542e-01 * 2.0 - 1.0$

$x_8 = (x_8 - 6.195e+00) / 1.377e+00 * 2.0 - 1.0$

$x_9 = (x_9 - 5.437e+00) / 4.660e+00 * 2.0 - 1.0$

Appendix B: Response Surface Fits

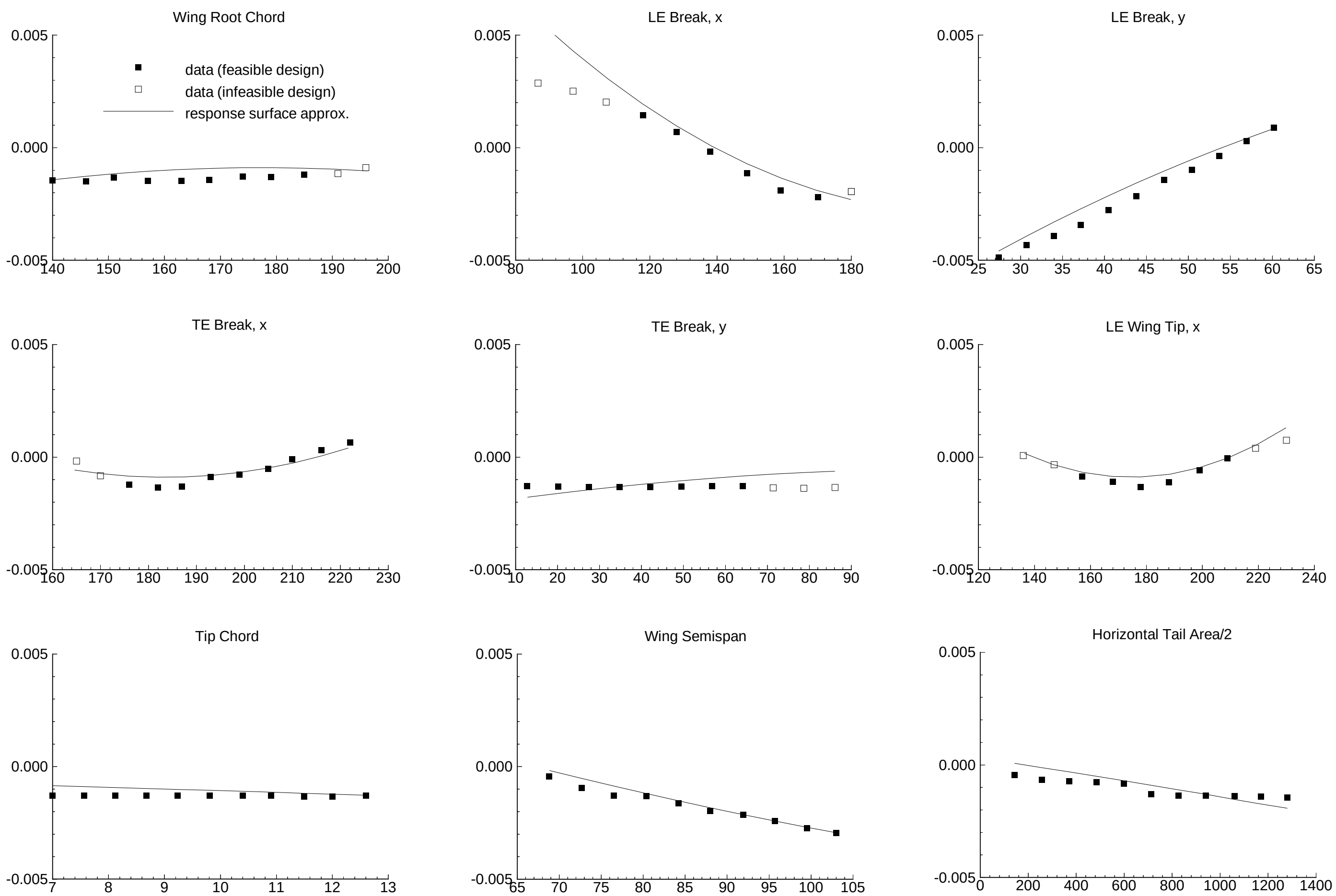

Figure B-1. Response surface fits of $C_{M_{\alpha},1}$ through design space.

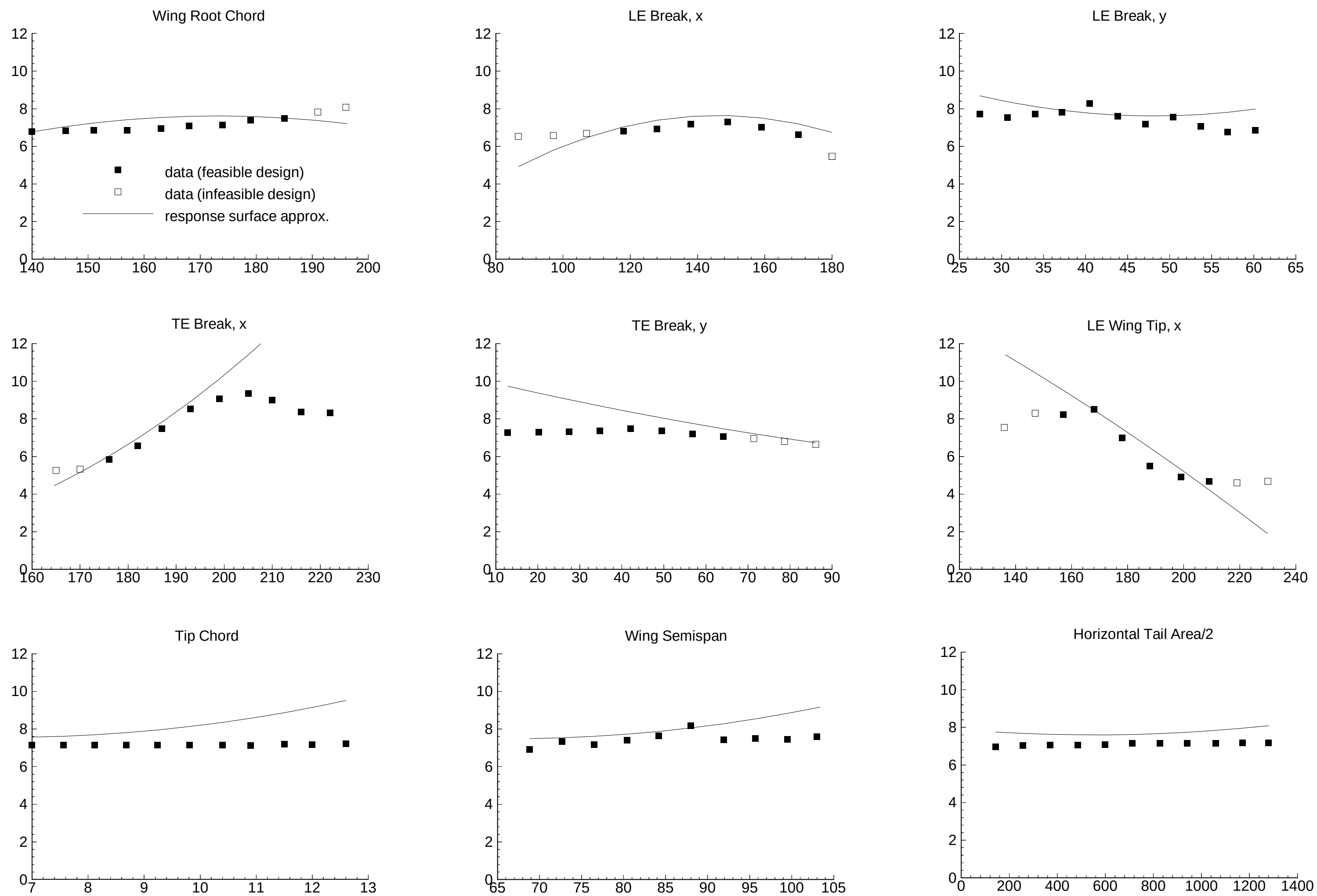

Figure B-2. Response surface fits of α_B through design space.

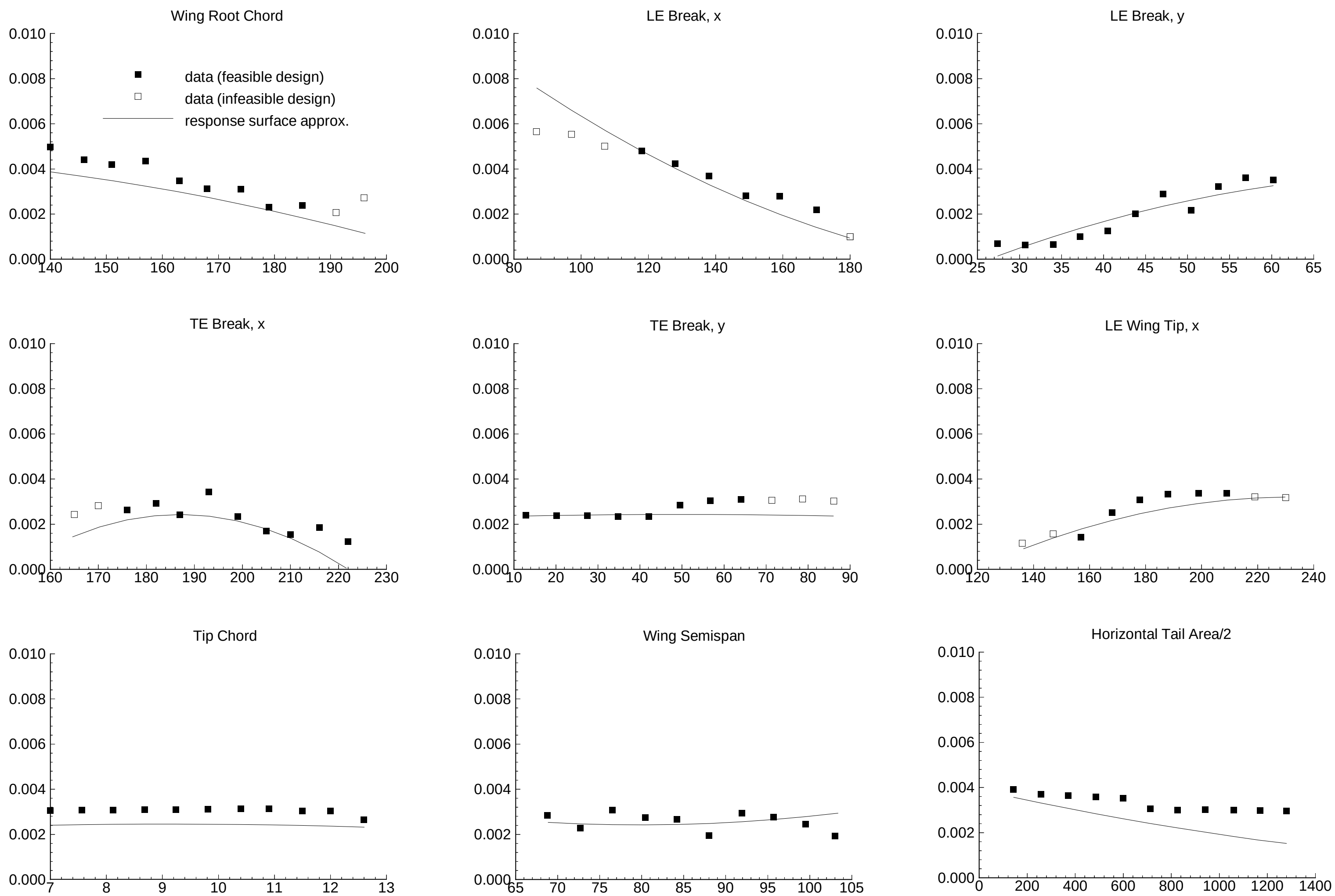

Figure B-3. Response surface fits of $C_{M\alpha,2}$ through design space.

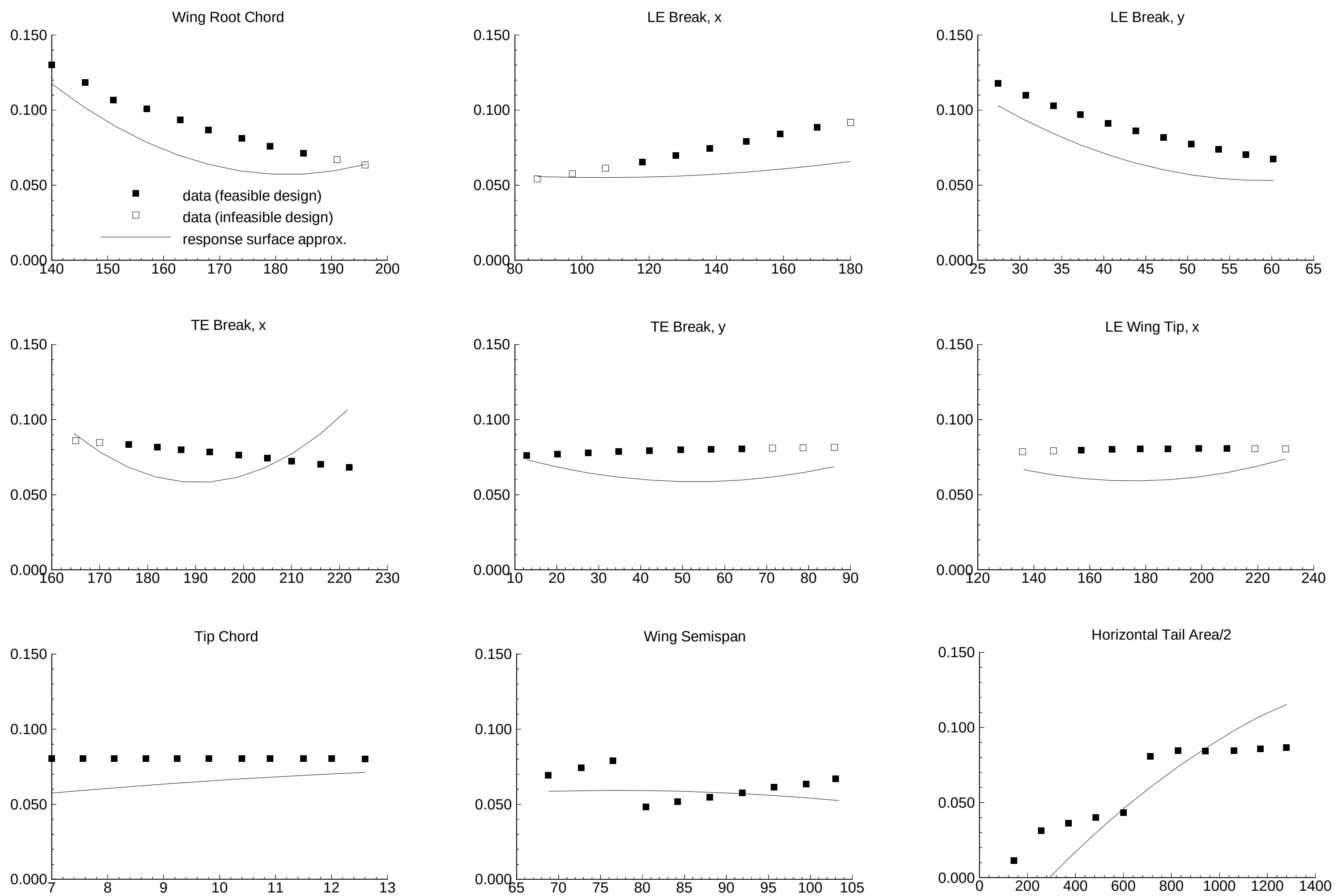

Figure B-4. Response surface fits of $\Delta C_{M\delta e}$ through design space.

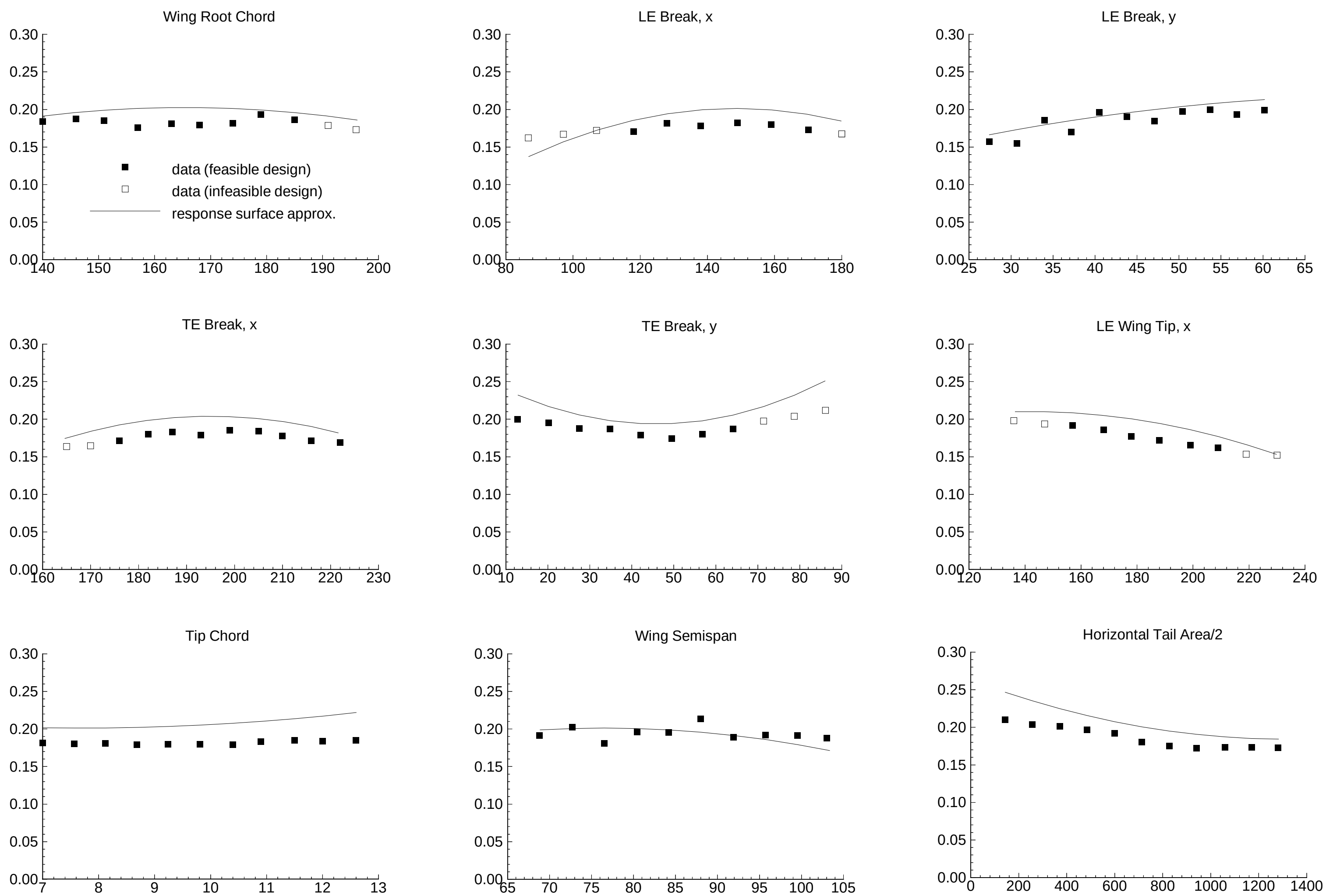

Figure B-5. Response surface fits of $\Delta C_{L\delta f}$ through design space.

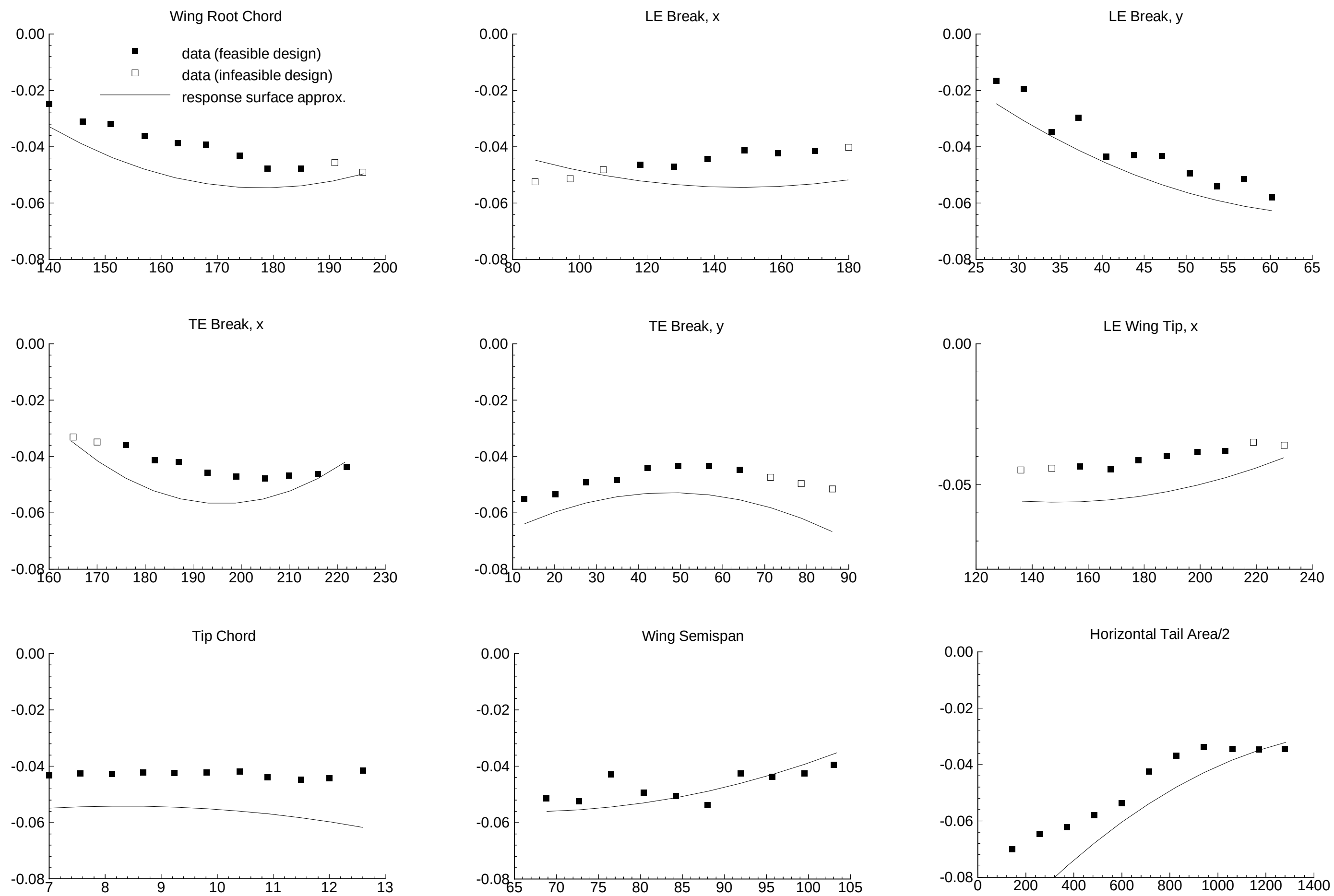

Figure B-6. Response surface fits of $\Delta C_{M\delta f}$ through design space.

Appendix C: Trailing-Edge Flap Deflection Effect

For this study, the takeoff configuration included horizontal tail, leading-edge flap, and trailing-edge flap deflections of -20 degrees, 10 degrees, and 20 degrees respectively. In a previous study by MacMillin[8], he performed optimizations with a trailing-edge deflection of 30 degrees. Preliminary analysis using response surface models within this study resulted in designs that could not satisfy the balanced field length of 11,000 feet with a trailing-edge deflection of 30 degrees. Therefore, optimizations were performed with a trailing-edge deflection of 20 degrees. However, results showed that two different optimal designs were achieved with a 20 degree and 30 degree deflection. This appendix describes the differences in these designs and how they were achieved throughout the optimization.

As shown in Figure C-1, an HSCT design with a TOGW of 700,100 *lbs* was used as an initial design. This initial design violated the range constraint, two thrust constraints, the takeoff rotation constraint, nacelle spacing constraint, and the engine out stability constraint. Two optimizations were performed, one with the trailing-edge flaps set at 20 degrees and one with the trailing-edge flaps set at 30 degrees during takeoff. The horizontal tail and leading-edge flaps were deflected -20 degrees and 10 degrees. The final optimal designs are shown as Case A and Case A2. A convergence history of the TOGW, range, balanced field length, planform design variables, and horizontal tail area are shown in Figures C-2 and C-3 for each optimization. Figures C-4 and C-5 show the engine size and fuel weight for each case. Table C-1 lists the weight data, planform geometry characteristics, and performance data on each optimal design.

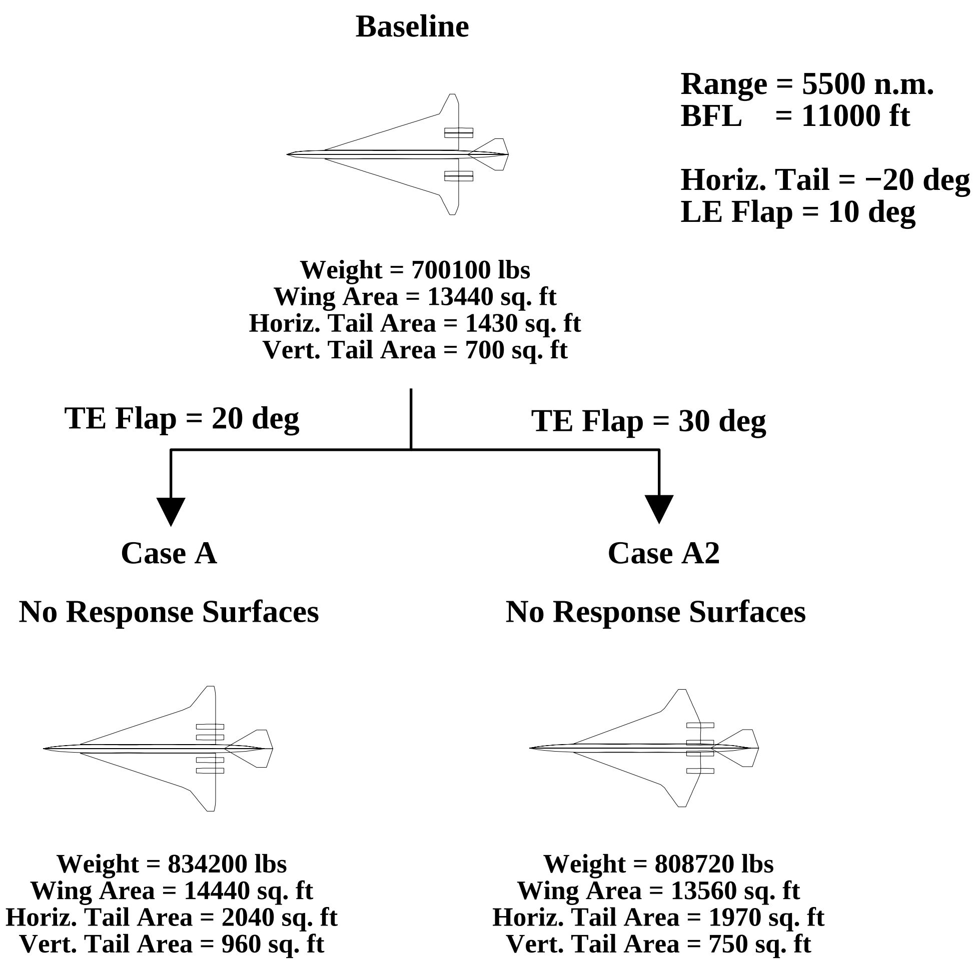

Figure C-1. Design optimizations with a change in TE flap deflection.

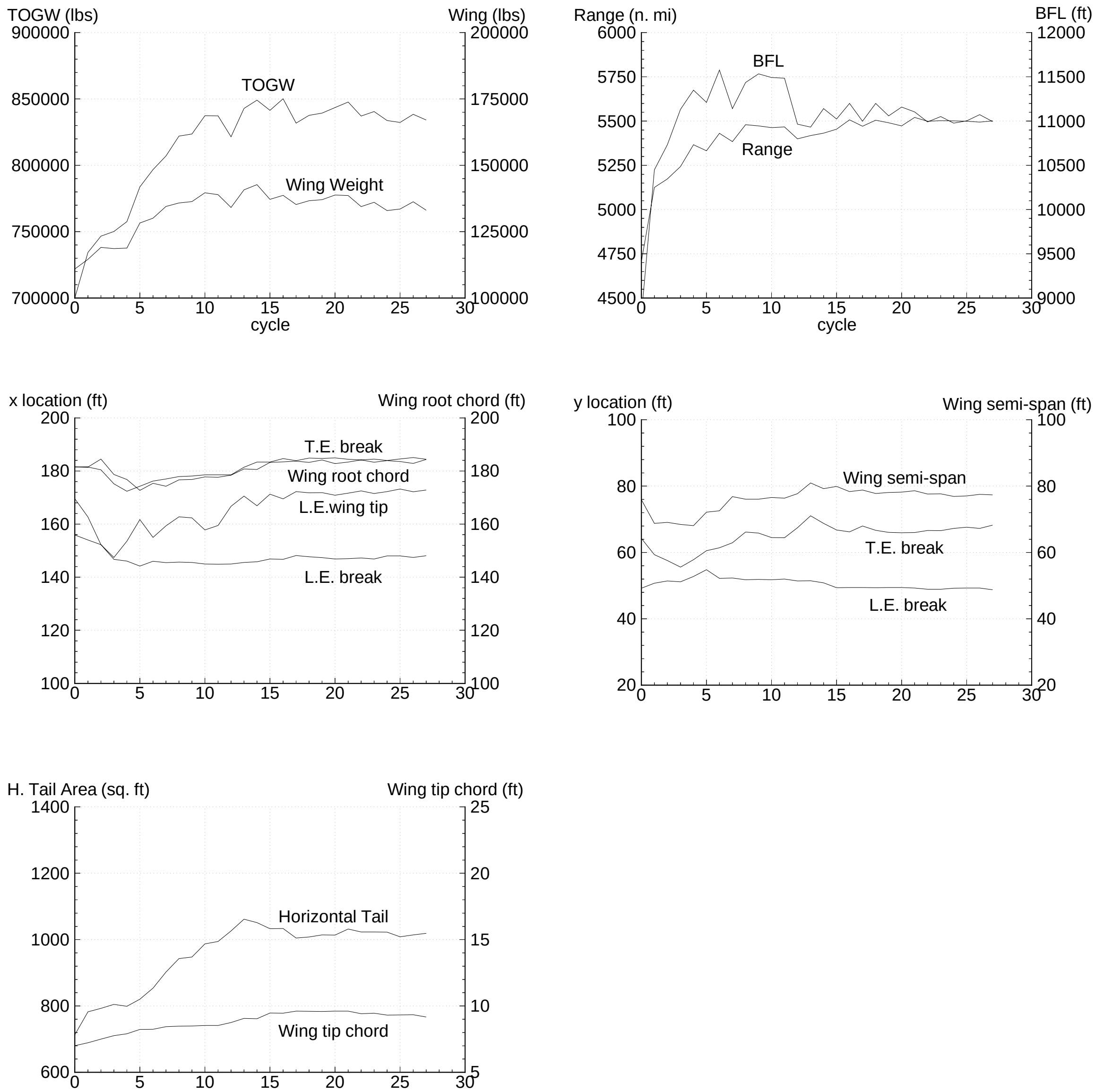

Figure C-2. Design history for Case A.

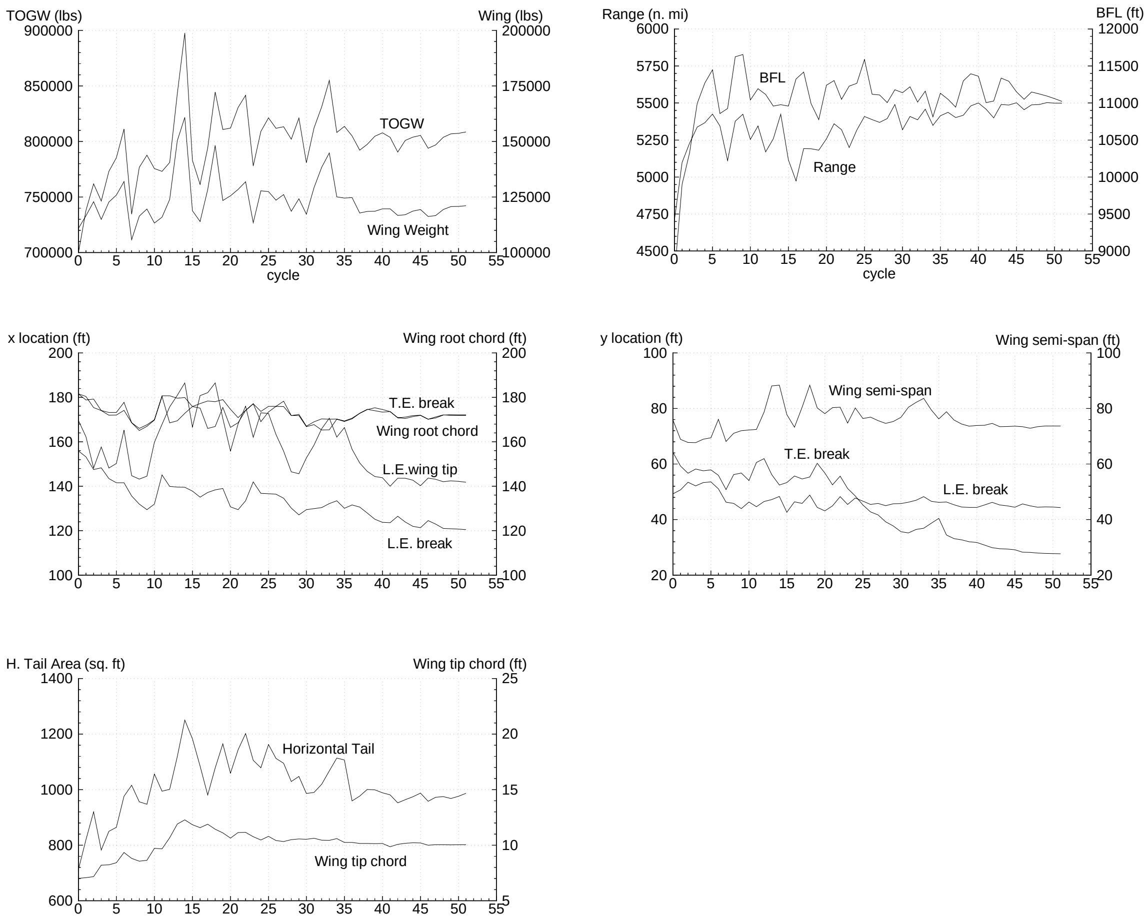

Figure C-3. Design history for Case A2.

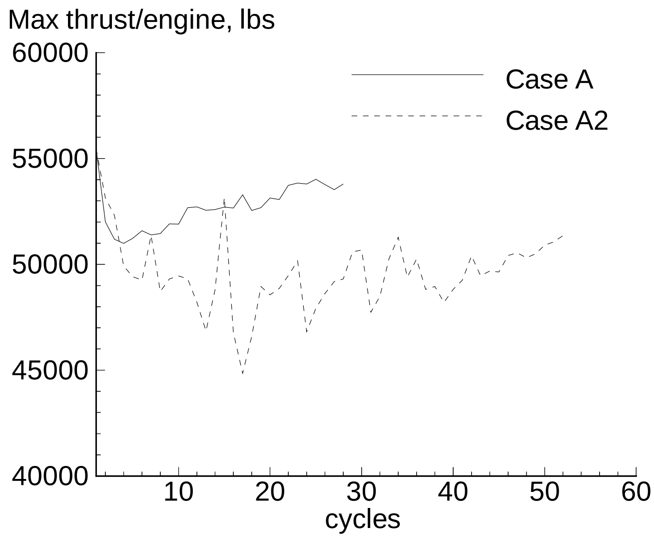

Figure C-4. Variation in thrust for Case A and Case A2.

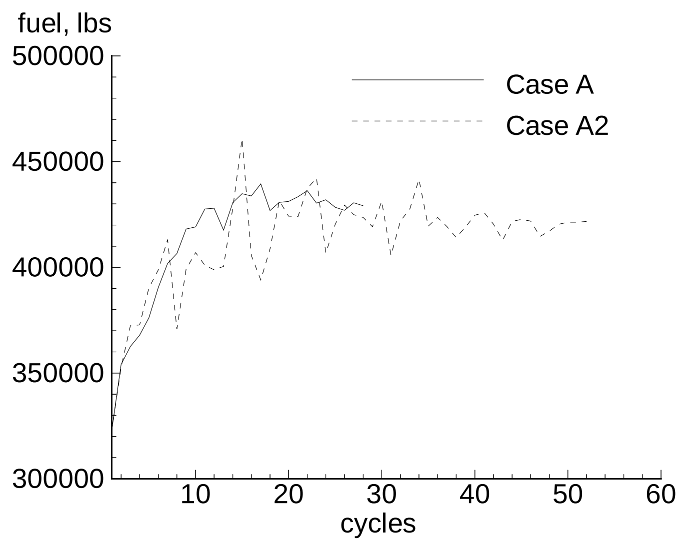

Figure C-5. Variation in fuel weight for Case A and Case A2.

Table C-1. Results for Case A and Case A2.

Weight Data	Case A	Case A2
Gross weight, *lbs*	834195	808717
Wing weight, *lbs*	133118	121102
Fuel weight, *lbs*	429059	421636
Fuel/Gross	0.51	0.52
Planform Geometry		
Root chord, *ft*	184.4	171.9
Tip chord, *ft*	9.2	10.0
Wing area, *sq ft*	14435	13560
Wing span, *ft*	166.8	159.4
Aspect ratio	1.9	1.9
Horizontal tail area, *sq ft*	2037.8	1973.4
Vertical tail area, *sq ft*	957.7	748.7
LE sweep, inboard	71.8¡	69.8¡
LE sweep, outboard	40.8¡	35.9¡
TE sweep, outboard	0.0¡	-23.9¡
Performance Data		
Range, *n. mi.*	5501	5500
Balanced field length, *ft*	10995	11022
Max thrust/engine, *lbs*	53792	51354
Landing angle-of-attack	10.6¡	10.9¡
$(L/D)_{max}$	9.4	9.2

As shown in Figure C-1, the optimal design using a 30 degree trailing-edge deflection during takeoff has a forward swept trailing edge similar to MacMillin s designs[8]. In contrast, the optimal design using a trailing-edge deflection of 20 degrees has no sweep on the trailing-edge and is much heavier by 25,470 *lbs* with a larger horizontal and vertical tail. Before explaining why the configurations are different, the takeoff performance of each optimal design was investigated by changing the trailing-edge flap deflection and recalculating the balanced field length and time-to-rotate. These results are listed in Tables C-2 and C-3.

Table C-2. Takeoff performance vs. TE flap deflection (Case A).

Takeoff Performance	TE Flap = 20°	TE Flap = 30°
Balanced Field Length (*ft*)	10971	10546
Time-to-Rotate (*sec*)	4.9	5.4

Table C-3. Takeoff performance vs. TE flap deflection (Case A2).

Takeoff Performance	TE Flap = 20°	TE Flap = 30°
Balanced Field Length (*ft*)	11559	11022
Time-to-Rotate (*sec*)	4.9	5.0

As presented in Tables C-2 and C-3, the balanced field length decreased for both designs when the trailing-edge flaps were deflected at 30 degrees. This is expected since flaps are used to increase the lift of an aircraft in order to decrease the takeoff distance. Also shown in Tables C-2 and C-3, the time-to-rotate increased with a higher trailing-edge deflection. The increase in the time-to-rotate means that the aircraft started its rotation at a lower takeoff speed and therefore took longer to reach the takeoff attitude.

As shown in Figure C-2, C-4, and C-5, the optimizer increased the amount of fuel to increase the range and initially decreased the thrust to increase the takeoff distance since the initial balanced field length is less than 11,000 *ft*. While the fuel weight continued to increase to bring up the range, the balanced field length increased past 11,000 *ft*. At this point, the horizontal tail size increased and the engine size increased to bring the balanced field length back to 11,000 *ft*. The final result is an increase in the wing area, fuel, and L/D to obtain the required mission range of 5,500 nautical miles. The engine size and horizontal tail size increased to satisfy the balanced field length requirement. In addition, the vertical tail size increased to satisfy the engine out stability requirement. The driving constraints for the design were the range and balanced field length.

For Case A2, the optimizer behaved the same as in Case A. However, the thrust decreased more than in Case A to increase the takeoff length, since takeoff is shorter with a greater flap deflection. The optimizer continued to increase the fuel to obtain the required range. As a result, the airplane started to get heavy and the horizontal tail increased to achieve the desired balanced field length while continuing to decrease the engine size to save weight. This continued with little improvement in the range until the 20th optimization cycle. At this point, the optimizer decided to decrease the TOGW to increase the range by designing a wing with less weight. This is achieved by sweeping the trailing-edge forward (TE break moves inboard and LE wing tip moves forward). With a decrease in wing weight, the engine size increased with a decrease in the horizontal tail size to achieve the desired balanced field length. The final result is an aircraft design which is lighter than Case A by 25,470 *lbs*, which is the difference in the wing, fuel, and engine weight. The vertical tail size is smaller due to the smaller engines and TOGW. The thrust to weight ratio for both designs are approximately the same, 0.258 for Case A and 0.254 for Case A2. The constraints driving this design were the range constraint, balanced field length constraint, time-to-rotate constraint, engine out stability constraint, and the two thrust constraints.

Vita

The author was born in Baltimore, Maryland to Lunette and Joseph Crisafulli on January 1, 1971. After residing in Northern Virginia for 11 years, he began his higher education at Virginia Polytechnic Institute & State University in 1989. He completed his Bachelor of Science degrees in Aerospace and Ocean Engineering in 1994. He continued his education at Virginia Polytechnic Institute & State University and completed the Master of Science degree in Aerospace Engineering in 1996.